THESIS

Study of Real-Time Optical Information Processing Using Spatial Light Modulators

Xin LIN

Graduate School of Electronic Science and Technology

Shizuoka University, Japan

February 1996

To

Mother, Father, and Lin

ABSTRACT

The present thesis describes the real-time optical information processing and computing by using liquid crystal spatial light modulators (LC-SLMs), such as real-time optical speckle metrology, real-time optical image processing and optical neural network system for pattern recognition.

Firstly, the key performance characteristics of twisted nematic liquid crystal television (LCTV) SLM (fabricated by Seiko Epson) and ferro-electric liquid crystal (FLC) two-dimensional photoaddressed SLM (fabricated by Hamamatsu Photonics, K.K.) are theoretically and experimentally investigated. Then, a method for the generation of a joint pattern to calculate a joint transform correlation function by using these LC-SLMs and a real-time optical joint transform correlator for displacement or velocity measurement in speckle applications are proposed. The generation of a joint pattern is verified by the experiment. It is possible to perform a real-time all optical joint transform correlation based on the proposed method. The velocity measurement up to 100 mm/s is realized at moderate operations of the FLC devices.

Next, real-time optical image subtraction and edge enhancement based on a speckle modulation technique are carried out by using FLC polarization switches and a FLC-SLM. A FLC-SLM is employed as a real-time and multiple-exposure optical device and the successful results are obtained from three-exposure images modulated by speckles. Thus, the image subtraction and edge enhancement are realized in real time. The whole operation is performed within several ms with a modest condition of the operation. As the used FLC-SLM has a high resolution more than 100 *l*p/mm and can store fine speckle patterns, the image qualities for the obtained results are quite satisfactory.

Finally, an optical neural network with a dynamics system of terminal attractors for pattern recognition is described and compared with the conventional Hopfield model neural network. The convergence of a unique solution and usefulness of the terminal attractor model are demonstrated by computer simulation and also optical experiment by using LCTV-SLMs. The results indicate that a terminal attractor neural network model can reduce spurious states in the Hopfield model.

CONTENTS

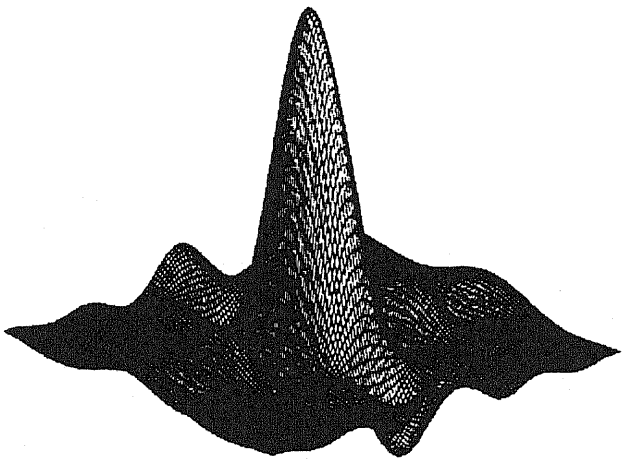

STUDY OF REAL-TIME

OPTICAL INFORMATION PROCESSING USING SPATIAL LIGHT MODULATORS

Optics is an old and venerable subject ...

Optics is a novel and captivating subject ...

CHAPTER 1

INTRODUCTION

1.1 A BRIEF HISTORY OF OPTICAL INFORMATION PROCESSING

Optical information processing is an advancing field which has received much attention since the nineteen sixties. It can handle a two-dimensional array of information using light in real time. The attractive feature of optical processing is the capability of parallel processing, which offers great potentials in processing capacity and speed. Optical processing is especially useful if the information to be processed is given by an optical form. Even for opto-electronic hybrid pattern processing, optics can also be useful for such information processing.

The study of optical information processing involves not only the realization of optical systems, but also optical devices as shown in Fig. 1.1.

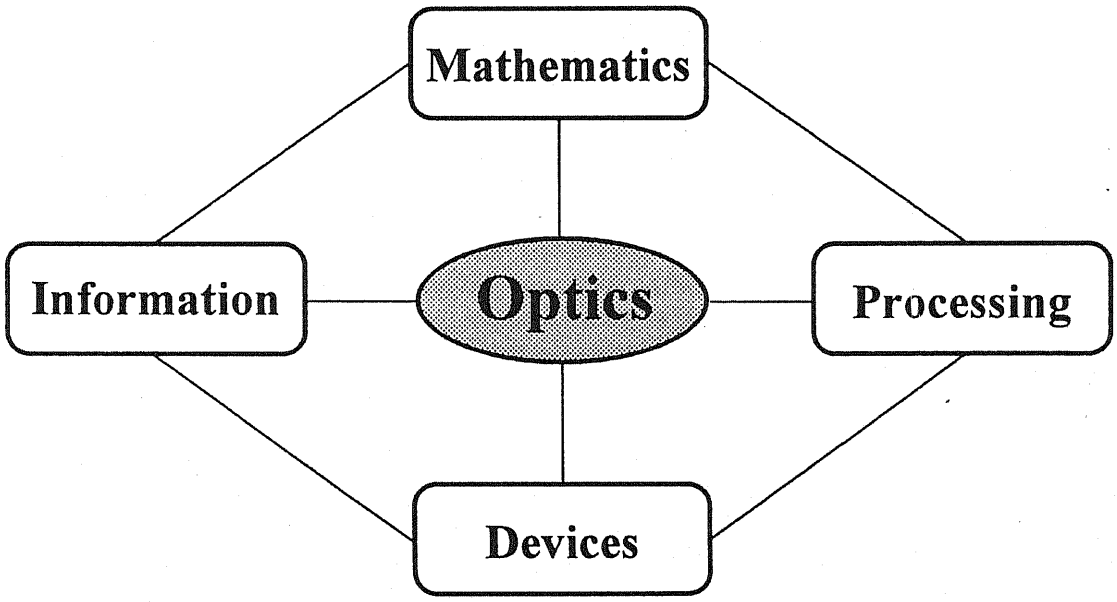

Fig. 1.1 Interrelation of disciplines required in the study optical information processing.

Historically, the idea of optical processing is dated from 1859, when Foucault first described the knife-edge test in which the direct light from an image was removed and the scattered or diffracted light was kept.[1.1] In 1873, Abbe advanced the theory in which

diffraction plays an important role in coherent image formation.[1.2] In 1906, Porter demonstrated the Abbe's theory experimentally.[1.3] Zernike developed the Nobel prize-winning concepts of the phase contrast microscopy in 1935.[1.4] In 1946, Duffieux published his important study on the use of the Fourier integral in optical problems.[1.5] In the fifties, Elias provided the initial exchange between the disciplines of the optics and communication theories.[1.6-7] Later O'Neill contributed a great deal to reconciling the two viewpoints by presenting a unified theory.[1.8] Maréchal motivated the future expansion of the interests in optical processing by successfully applying coherent spatial-filtering techniques to improve the quality of photographs.[1.9]

In the 1960's, optical processing activities reached a new height with its successful application to synthetic-aperture radar.[1.10-11] The inventions of the holographic spatial filter by Vander Lugt[1.12] and of the computer generated spatial filter by Lohmann and Brown[1.13] also form the important cornerstones for the application of optical processing to the lucrative field of pattern recognition. Many researches have also been carried out to develop real-time interface devices which connect electronic or incoherent optic systems with coherent optic ones.

In the seventies, the importance of combining electronic digital computers with optical analog processors to form hybrid processors was established. Much attention has also been given to extend the flexibility of optical processors beyond linear and space invariant regimes.

Progress in the development of spatial light modulators (SLMs), in particular for optical processing, has dramatically accelerated in the 1980's. Horner has studied the theoretical background for the use of SLMs in optical pattern recognition.[1.14-15] Javidi has analyzed the optical correlation and deconvolution problems based on the operation of SLMs.[1.16-18] The applications of SLMs for optical information processing have been experimentally conducted by Yu *et. al.*[1.19-20]

Recently, liquid crystal devices (LCDs) have been used as SLMs in the field of optical information processing because of the low cost of the devices and the ease of the

commercial availability.[1.21-25] In 1991, Ohtsubo *et. al.* proposed optical information processing systems using liquid crystal SLMs involving the optical speckle metrology,[1.26] optical images processing,[1.27] and optical neural network systems.[1.28] The liquid crystal SLMs have become key components in many real-time optical and optoelectronic systems, such as optical processing, optical interconnections, optical phase conjugation, real-time holography, optoelectronic implementation of neural networks, image processing and displays.

1.2 RESEARCH OBJECTIVES

As already mentioned, since the advent of laser, optical information processing have attracted strong attention of many investigators and have been studied by them. However, the study of real-time optical information processing using spatial light modulator is still in the incunabula. The questions many researches are involved in are "Are SLMs useful for real-time optical information processing?" and "How to use them?" This thesis tries to give a preliminary answer to these questions.

One of the successful fields of the applications is laser speckle information processing. Optical information processing and optical measurements with speckle modulation were proposed about 25 years ago and have been studies by many researchers since then. Photographic film is generally used for recording speckle patterns due to high sensitivity, high space bandwidth product, low cost and availability. But, film requires development which makes the real-time operation of information processing difficult. More recently, photodetectors have been used in electronic speckle pattern interferometry and digital particle image velocimetry system. The limitations of these systems are the low space bandwidth product and the low throughput by the photosensors. The latter makes it difficult to record fast multiple events and, in the cases of speckle photography or digital particle image velocimetry, requires substantial digital post-processing, precluding the real-time operation.

Recently the situations have drastically changed. In optical processing techniques for

speckle information processing and metrology, electrically addressed SLMs[1.29] and photorefractive materials[1.30] have been used. In the former, speckle patterns may be captured on a CCD camera and transferred to the electrically addressed SLM for the subsequent processing. These systems also suffer from the drawback of limited TV frame rate (30Hz) and low space bandwidth product (~256×256). The problem with the latter approach is that photorefractive materials generally have slow response times for reasonable laser powers (order 1 s at 1 mW/cm^2).[1.31]

Because of the nature of materials and the characteristics of devices, those systems may not be sufficient to realize a "real-time" optical processing in many applications which require fast processing of signals. As an alternative device, we use a new SLM for the "real-time" method of optical speckle information processing. An optically addressed FLC-SLM has the capabilities of a time response as fast as 100 μs or more, the larger data throughput, and the potential for real-time optical processing.

Recently, optical neural networks have received considerable attention for their applications to information storage and processing. The answer for "Why does one use optics in computers?" is that photons do not interact with each other. Consequently, light beams can pass through one another without distorting the information carried on. This suggests that optical memory may be able to avoid the difficulties of memory contention, at least during reads. Furthermore, optical technology offers parallel processing and two- and three-dimensional interconnections. Thus, the speeds of the write and read operations do not become a "bottleneck" in optical computers. Namely, the limitations of the conventional electronic computers are overcome by the inherent capabilities of the optics.[1.32-33]

Optical associative memory in neural networks has the significant advantages of the inherent parallelism and interconnectivity in optics. But the conventional Hopfield model system which is widely used in this field has major problems as an optical associative memory as follows:

1. The memory capacity is very low. The maximum number of patterns that can be exactly

stored in a network with n neurons is only about $n/(4\log n)$. [1.34]

2. The basins of attraction of stored patterns are small, so that the recollection ability is not very great.

3. There are many spurious memories, namely equilibrium states different from the stored patterns.

4. Stored patterns must be nearly orthogonal to each other. Otherwise, the performance of the model is greatly deteriorated.

Although many modified models have been proposed,[1.35-36] but they are not optical implementations. This thesis also reports a terminal attractor optical associative memory for pattern recognition. It is verified in optical experiment that this associative memory works well.

1.3 OUTLINE OF THIS THESIS

The present thesis describes the real-time optical information processing using liquid crystal SLMs, such as real-time optical speckle metrology, real-time optical image processing and optical neural network system. The layout of the thesis proceeds as follows.

Chapter 2 concerns the theoretical backgrounds and performance characteristics of a twisted nematic liquid crystal television (TN-LCTV) SLM and a ferro-electric liquid crystal (FLC) two-dimensional photoaddressed SLM. The intensity and phase modulation characteristics of LCTV and FLC as a SLM are theoretically and experimentally investigated. Furthermore, the resolution, the visibility, and the optical and electronical multiple-exposure capability for the FLC-SLM are discussed. The obtained results indicate that these SLMs can be used in real-time optical information processing.

Chapter 3 discusses the real-time optical speckle metrology using LC-SLMs. In Section 3.2, a method for the generation of a joint pattern to calculate a joint transform correlation function for real-time optical speckle measurements is described. The polarization of the speckle pattern is switched by a 90° twisted nematic liquid crystal and the spatial shift is

introduced to the pattern by passing through the birefringent calcite plate depending on its p- or s-polarized state. The generation of the joint pattern is verified by the experiment. Based on the proposed method, displacements of a light scattering object are measured. But the switching speed of the TN-LC cell is rather slow and is about 100 ms. On the other hand, FLC device which has a switching speed of the order of micro-second to several tens of micro-second. This value of the switching speed is satisfactory for most mechanical applications in optical speckle metrology. Therefore, a real-time high-speed joint transform correlator (JTC) for optical speckle interferometry is proposed by using FLC-SLM and FLC polarization switch in Section 3.3. The successive patterns from a light scattering object before and after the displacement pass through a FLC polarization switch and a birefringent plate. The joint pattern is take by a FLC-SLM as a doubly exposed pattern. The JTC is optically calculated from the joint pattern. To demonstrate the usefulness of the system, the vector velocity measurement of a light scattering object is presented.

Chapter 4 is devoted to the real-time optical images processing using FLC polarization switches and a FLC-SLM based on speckle modulation. Section 4.1 gives an optical subtraction system and, in Section 4.2, an optical edge enhancement system based on speckle defocusing modulation is carried out. FLC devices have attractive features of high-speed switching, memory effect, multiple exposure capability of images, and polarization and intensity switching capabilities. Therefore, they can become promising devices for real-time optical information processing. In above two images processing systems, a FLC-SLM is employed as a real-time and multiple exposure optical device and the successful results are obtained from three exposure images modulated by speckles. Thus the images processing are realized in real time. The whole operation are performed within several ms with a modest condition of the operations. As the used FLC-SLM has a high resolution more than 100 *l*p/mm and can store fine speckle patterns, the image qualities for the obtained results are quite satisfactory.

Optical associative memory in neural network has the significant advantages of the

inherent parallelism and interconnectivity in optics. Optical neural network for pattern recognition using the Hopfield model has the advantage of the simplicity for its structure of the network. But further investigation reveals that the storage capacity of the Hopfield model is quite limited because of the number of spurious states and the oscillations. For the purpose for the alleviation of the spurious state in the Hopfield neural network, the concept of terminal attractors has been introduced.[1.37] Based on the idea of the terminal attractors, we propose an optical neural network with a dynamics system of terminal attractors a for pattern recognition in Chapter 5. The convergence of a unique solution and usefulness of the terminal attractors are demonstrated by the computer simulation and the optical experiment using LCTV-SLMs. The results indicate that a terminal attractor neural network model can reduce spurious states in the Hopfield model.

REFERENCES

1.1 L. Foucault, *Ann. Obs. Imp.* (Paris) **5**, 197 (1859).

1.2 E. Abbe, *Arch. Mikros. Anat.* **9**, 431 (1873).

1.3 A. B. Porter, *Phil. Mag.* **11**, 154 (1906).

1.4 F. Zernike, *Z. Tech. Mag.* **16**, 454 (1935).

1.5 P. M. Duffieux, *Faculté des Sciences*, Université de Besançon (1946).

1.6 P. Elias, D. S. Grey, and D. Z. Robinson, *J. Opt. Soc. Am.* **42**, 127 (1952).

1.7 P. Elias, *J. Opt. Soc. Am.* **43**, 229 (1953).

1.8 E. L. O'Neill, *IRE Tarns.* IT-**2**, 56 (1956).

1.9 A. Maréchal, P.Croce, *Compt. Rend.* **237**, 706 (1953).

1.10 L. J. Cutrona, E. N. Leith, L. J. Porcello, and W. E. Vivian, *Proc. IEEE* **54**, 1026 (1966).

1.11 E. N. Leith, *Proc. IEEE* **59**, 1305 (1971).

1.12 A.B.Vander Lugt, *IEEE Trans.* IT-**10**, 130 (1971).

1.13 B. R. Brown, and A. W. Lohmann, *Appl. Opt.* **5**, 967 (1966).

1.14 J. L. Horner, *Appl. Opt.* **21**, 4511 (1982).

1.15 J. L. Horner, and J. R. Leger, *Appl. Opt.* **24**, 609 (1985).

1.16 B. Javidi, and C. J. Kuo, *Appl. Opt.* **27**, 663 (1988).

1.17 B. Javidi, *Appl. Opt.* **28**, 4518 (1989).

1.18 B. Javidi, *Opt. Commun.* **78**, 325 (1990).

1.19 F. T. S. Yu, and X. J. Lu, *Opt. Commun.* **52**, 10 (1984).

1.20 F. T. S. Yu, and J. E. Ludman, *Opt. Lett.* **11**, 395 (1986).

1.21 C. C. Mao, K. M. Johnson, R. Turner, D. Jared, and D. Doroski, *Appl. Opt.* **28**, 219 (1989).

1.22 T. H. Chao, *Appl. Opt.* **28**, 4727 (1989).

1.23 C. C. Mao, K. M. Johnson, and G. Moddel, *Ferroelectrics* **114**, 45 (1991).

1.24 C. M. Gomes, H. Sekine, T. Yamazaki, and S. Kobayashi, *Neural Net.* **5**, 169 (1992).

1.25 D. Cunningham, J. Sharpe, and K. M. Johnson, *Opt. Commun.* **101**, 311 (1993).

1.26 A. Ogiwara, H. Sakai, and J. Ohtsubo, *Opt. Commun.* **86**, 513 (1991).

1.27 H. Sakai, and J, Ohtsubo, *Appl. Opt.* **31**, 6852 (1992).

1.28 J. Ohtsubo, and M. Watanabe, *OSA Annual Meeting* **94** (1994).

1.29 B. Bates, and P. C. Miller, *Opt. and Lasers in Eng.* **14**, 341 (1991).

1.30 S. H. Collicott and L. Hesselink, *Opt. Lett.* **13**, 348 (1988).

1.31 P. Yeh, and C. Gu, *Int J. of Nonlinear Opt. Phys.* **1**, 167 (1992).

1.32 T. Bell, *IEEE Spectrum* **23**, 34 (1986).

1.33 B. K. Jenkins, and C. L. Giles, *Optical Computing* **22,** 625 (1986).

1.34 R. J. McEliece, E. C. Posner, E. R. Rodemich, and S. S. Venkatesh, *IEEE Trans. Inf. Theory,* IT-**33**, 461 (1987).

1.35 K. Aihara, T. Takabe, and M. Toyoda, *Phys. Lett. A*, **144**, 333 (1990).

1.36 M. Morita, *Neural Net.* **2**, 115 (1993).

1.37 M. Zak, *Neural Net.* **2**, 259 (1989).

Key performance characteristics of twisted nematic liquid crystal television and ferro-electric liquid crystal two-dimensional photoaddressed spatial light modulator are theoretically and experimentally investigated. Several characteristics that are important for optical information processing, including the intensity and phase modulation characteristics are discussed. Furthermore, resolution, visibility, and multiple exposure effect of ferro-electric liquid crystal spatial light modulator are investigated. The obtained results show that those SLMs can be used in real-time optical information processing.

CHAPTER 2

LIQUID-CRYSTAL SPATIAL LIGHT MODULATOR

2.1 LCTV-SLM

In many researches for optical information processing, twisted nematic liquid crystal televisions (LCTVs) with the active matrix drive have been used as a spatial light modulator (SLM) in a variety of ways.[2.1-2] LCTVs may be used for optical information processing because it has several salient SLM features. For example, its operation speed of ~10 ms is compatible with that of the image signals provided by a conventional TV system.

The intensity modulation property is an important characteristic of a SLM in most applications. The LCTV not only has the intensity modulation property, but also has the attractive features of polarization and phase modulations of light. The purpose of this section is to describe LCTV device structure, principle of the operation, and its intensity and phase modulation characteristics for the later use of optical information processing and computing.

2.1.1 Theory of Light Transmission in a TNLC Device

A twisted nematic liquid crystal cell is a thin layer of nematic liquid crystal placed between two parallel glass plates and rubbed so that the molecular orientation rotates helically about an axis normal to the plates (the axis of twist). If the angle of twist is 90°, for example, the molecules point in the x direction at one plate and in the y direction at the other, as shown in Fig. 2.1 (a). Transverse layers of the material act as uniaxial crystals, with the optic axes rotating helically about the axis of twist.

When an electric field is applied to the direction of the axis of twist (the z direction) the molecules tilt toward the field, as shown in Fig. 2.1 (b). When the tilt is 90°, the molecules lose their twisted character, so that the polarization rotatory power is deactivated. If the electric field is removed, the orientations of the layers near the glass surfaces dominate, thereby causing the molecules to return to their original twisted state, and the polarization rotatory power to be regained.

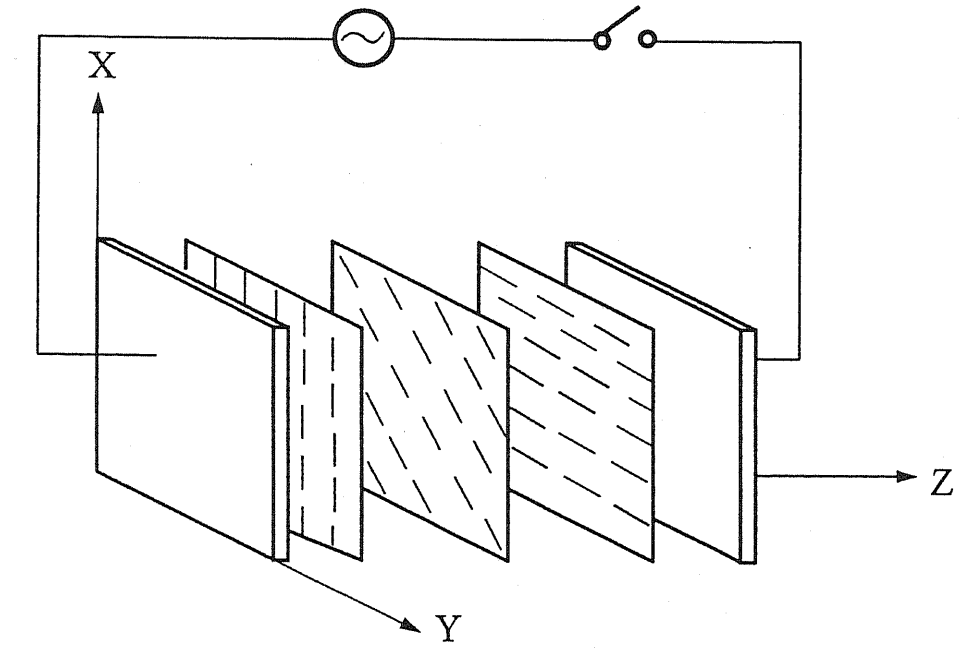

(a)

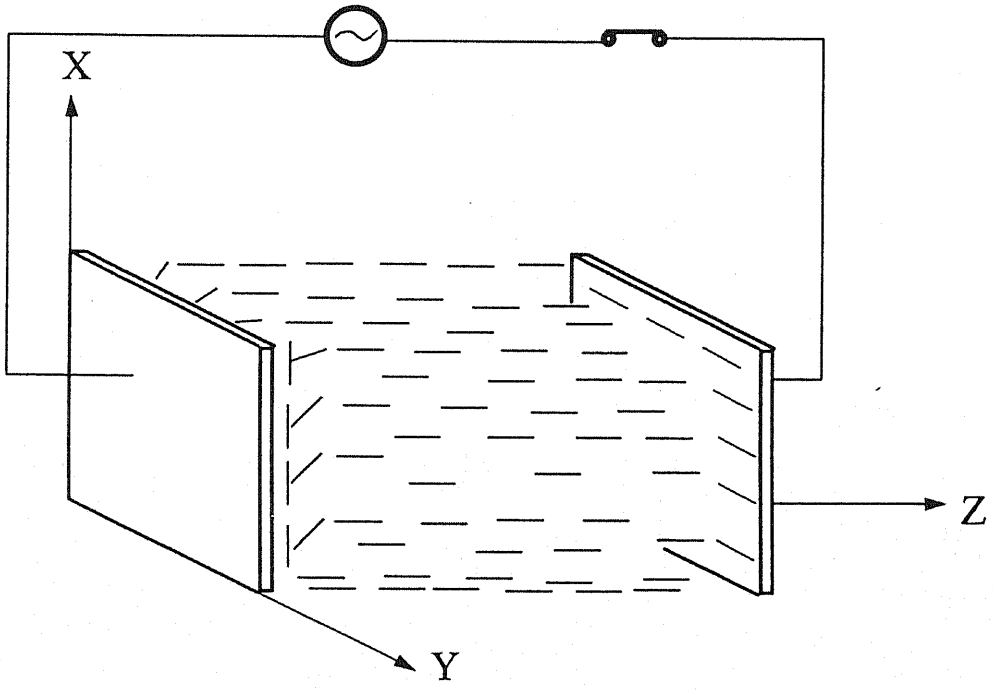

(b)

Fig. 2.1 In the presence of a sufficiently large electric field, the molecules of a twisted nematic liquid crystal tilt their twisted character. (a) Twisted state and (b) Tilted (untwisted) state.

The theoretical treatment of light transmission through a 90° TN-LCTV is almost the same as for a usual twisted nematic liquid crystal device (TN-LCD). In a TN-LCD, the propagation of polarized light along the twist axis is described by use of the Jones calculus. The TN-LCD is composed of a stack of identical birefringent plates, each oriented at a helically rotated angle, as shown in Fig. 2.1 (a). When the molecules align with the x axis at $z = 0$, we obtain the Jones matrix

$$J^{\pm} = \exp(-i\Phi)\begin{bmatrix} \frac{\pi}{2\gamma}\sin\gamma & \mp\cos\gamma \mp i\frac{\beta}{\gamma}\sin\gamma \\ \pm\cos\gamma \mp i\frac{\beta}{\gamma}\sin\gamma & \frac{\pi}{2\gamma}\sin\gamma \end{bmatrix}, \tag{2.1}$$

where J^{+} and J^{-} represent the Jones matrices for the clockwise and counterclockwise twists of the molecules and the liquid crystal material is assumed to be twisted by 90°. When an electric field is applied in the direction of the z axis, the parameters of the Jones matrices are obtained by

$$\beta = \frac{\pi d}{\lambda}[n(\theta) - n_o], \tag{2.2}$$

$$\Phi = \frac{\pi d}{\lambda}[n(\theta) + n_o], \tag{2.3}$$

$$\gamma = \sqrt{\left(\frac{\pi}{2}\right)^2 + \beta^2}, \tag{2.4}$$

where d and n_o are the thickness and ordinary refractive index of the liquid crystal material and λ is the wavelength of light. The equilibrium tilt angle θ for most molecules is a monotonically increasing function of the applied voltage, which can be described by[2.3]

$$\theta = \begin{cases} 0 & V \le V_c \\ \frac{\pi}{2} - 2\tan^{-1}[\exp(-\frac{V - V_c}{V_0})] & V > V_c \end{cases}, \tag{2.5}$$

where V is the applied rms voltage, V_c is a critical voltage at which the tilting process begins, and V_0 is a constant. When $V - V_c = V_0$, $\theta \approx 50°$.

When the electric field is removed, the orientations of the molecules near the glass surfaces are recovered and all of the molecules tilt back to their original orientation (in planes parallel to the plates). In a sense, liquid crystal material may be regarded as a liquid with memory.

For a tilt angle θ, an optical wave traveling in the z direction is polarized in the x and y directions and has refractive indices $n(\theta)$, where

$$\frac{1}{n^2(\theta)} = \frac{\cos^2\theta}{n_e^{\,2}} + \frac{\sin^2\theta}{n_o^{\,2}}. \tag{2.6}$$

Here, n_o and n_e are the ordinary and extraordinary refractive indices of the liquid crystal.

From above equations, we can recognize that the Jones matrix is a function of only one variable β, except for an unimportant multiplicative phase factor $\exp(-i\Phi)$, which is related to the applied voltage through the tilt angle θ. When the molecules are not tilted ($\theta = 0$), the retardation β achieves its maximum value,

$$\beta_{max} = \frac{\pi d}{\lambda}[n_e - n_o], \tag{2.7}$$

and decreases monotonically toward zero when the tilt angle reaches 90°. It was shown that β monotonically decreases with an increase of the applied voltage and that the relation between β and the applied voltage is approximately independent of the index difference of the birefringence, as shown in Fig. 2.2.

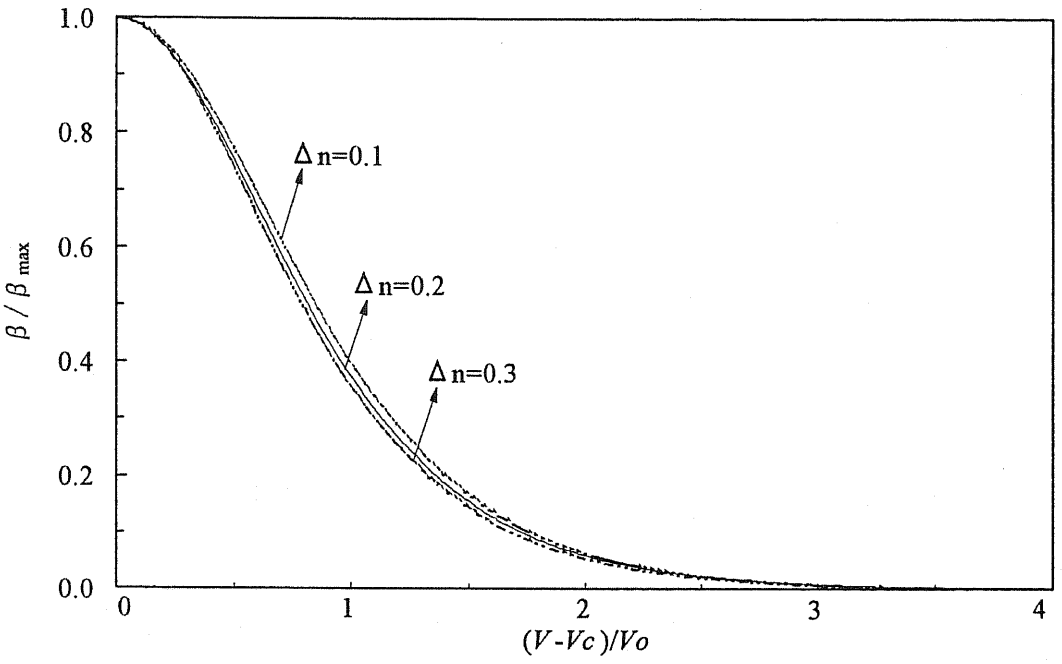

Fig. 2.2 Dependence of the normalized retardation $\beta / \beta_{max} = [n(\theta) - n_o] / (n_e - n_o)$ on the normalized rms applied voltage when $n_o = 1.5$, for the values of $\Delta n = n_e - n_o$ indicated.

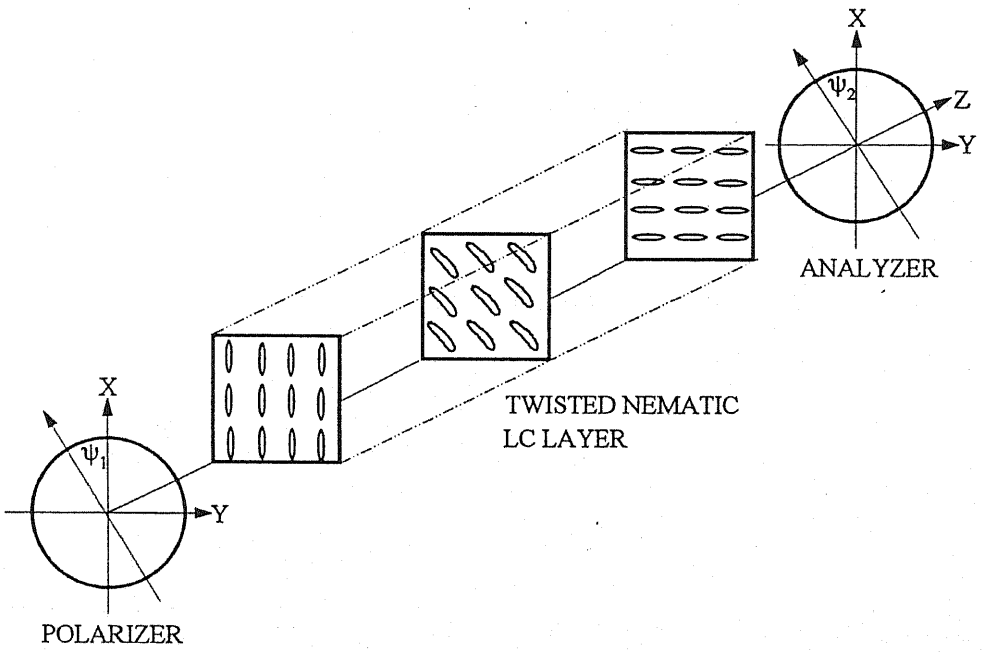

Fig. 2.3 Configuration of a 90°-TN LCTV with polarization filters: ψ_1, ψ_2, polarizer and analyzer angles.

Next, we proceed to determine the amplitude transmittance and phase shift introduced by the device as a function of β. Figure 2.3 shows a TN-LCTV model which is used in the experiment. When a TN-LCD is sandwiched between a polarizer and a analyzer, which, in general, form angles ψ_1 and ψ_2 with the x axis, the intensity transmittances of the clockwise and counterclockwise TN-LCDs are easily calculated from the Jones matrix. For an incident light linearly polarized along the direction of the polarizer, the intensity transmittances and phase shift are obtained by[2.4]

$$T^{\pm} = \left[\frac{\pi}{2\gamma}\sin\gamma\cos(\psi_1-\psi_2) \mp \cos\gamma\sin(\psi_1-\psi_2)\right]^2 + \left[\frac{\beta}{\gamma}\sin\gamma\sin(\psi_1+\psi_2)\right]^2, \tag{2.8}$$

$$\delta = \beta - \tan^{-1}\frac{(\frac{\beta}{\gamma})\sin\gamma\sin(\psi_1+\psi_2)}{(\frac{\pi}{2\gamma})\sin\gamma\cos(\psi_1-\psi_2)+\cos\gamma\sin(\psi_1-\psi_2)}. \tag{2.9}$$

The plus or minus sign of the transmittance T again denotes the clockwise or counterclockwise rotations of the twist. It is noted that the intensity transmittances for the configurations $(\psi_1,\psi_2) = (0^\circ,0^\circ)$ and $(\psi_1,\psi_2) = (90^\circ,90^\circ)$ are the same. Moreover, for given ψ_1 and ψ_2, both T and δ are a function of one variable, β. These expressions are simplified in two special cases which are important in the actual experiments: (i) the polarizer is orthogonal to the analyzer and parallel to the x-axis, i.e., $(\psi_1,\psi_2) = (0^\circ,90^\circ)$; (ii) the polarizer is orthogonal to the analyzer and also orthogonal to the x-axis $(\psi_1,\psi_2) = (90^\circ,0^\circ)$. The intensity transmittance T is a monotonic increasing function of β (i.e., a monotonic decreasing function of V) for the both cases. However, the phase shift is an approximately linear function in case (i), whereas there is no phase shift in case (ii). Thus, not only the intensity modulation but also the phase modulation of the LC device are obtained for the case (i), whereas the device is used only as an intensity modulator for the case (ii).

2.1.2 Intensity and Phase Modulation Properties

The LCTV used in the experiment is a projection TV panel of VPJ-700 (Seiko Epson) which is a 90° twisted nematic active matrix device with a thin film transistor (TFT). The panel consists of 220×320 pixels each having a size of 80×90 μm. As is shown in Fig. 2.3 for the theoretical model, the liquid crystal molecule director of the LCTV is vertically aligned at the front of the panel, while it is twisted by the right angle at the exit face.

After removing the original plastic polarizers from the LCTV panel, we evaluate the intensity transmittance and phase shift of the LCTV as almost the same manner that in Ref. 2.4. The extreme cases of the results are shown in Fig. 2.4.[2.5] The intensity transmittance and phase shift are plotted against the input composite video signal level having a 8-bit gray scale. In Fig. 2.4 (a), the orientation of the polarizer in Fig. 2.3 is aligned to be parallel to the liquid crystal molecule director at the front panel and that of the analyzer is rotated by 90°, i.e. corresponding to the configuration of $(\psi_1, \psi_2) = (0°, 90°)$ in Fig. 2.3. The phase shift from 0 to 1.2π radians and the normalized intensity transmittance of 0.3~1 are obtained in this configuration. Figure 2.4 (b) is the result for the case of $(\psi_1, \psi_2) = (90°, 0°)$. The phase modulation is not observed in this configuration, while the intensity transmittance is changed by the variation of the video signal.[2.4-6] Though we can observe no distinct phase change, the intensity modulation has the same tendency as that for the case in Fig. 2.4 (a). These results are coincident with the theoretical predictions in Subsection 2.1.1.

The diffraction efficiency of light by using the LCTV-SLM has been investigated by Ogiwara *et. al.*[2.5]. The results indicate that the phase modulation property of the LCTV rather than the intensity modulation property plays an important role to attain a high diffraction efficiency. Especially, the configuration of $(\psi_1, \psi_2) = (0°, 90°)$ is suited for the applications of the LCTV-SLM, for example, the application to an optical correlator or optical neural networks.

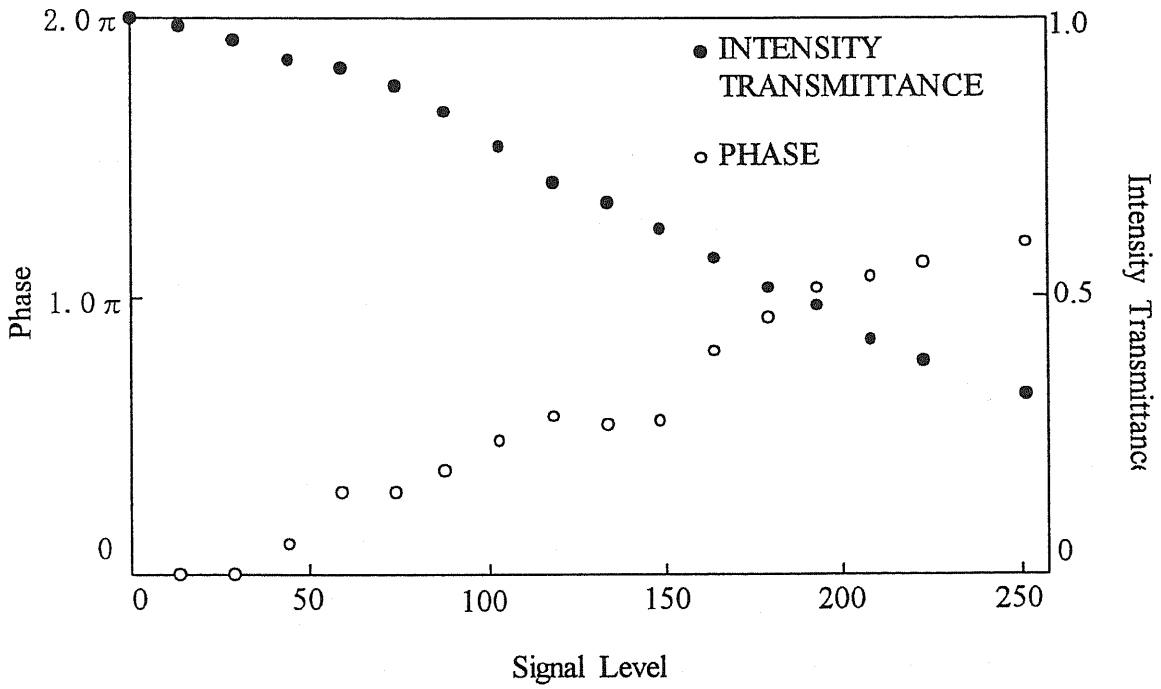

(a)

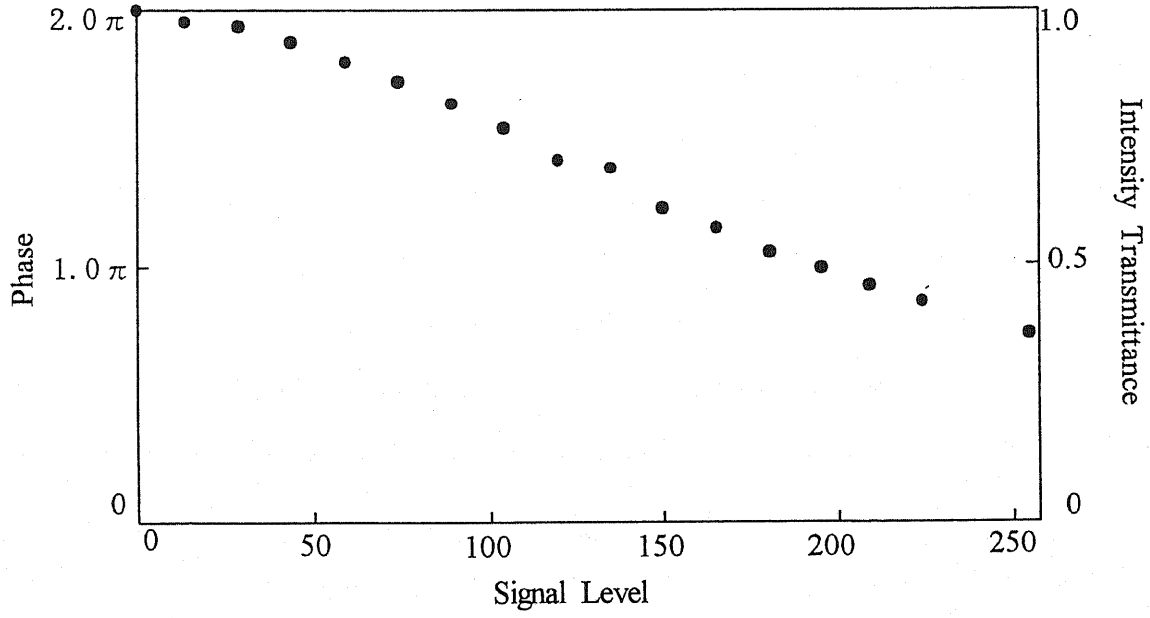

(b)

Fig. 2.4 Phase and intensity modulation properties of the LCTV at (a) $(\psi_1, \psi_2) = (0^\circ, 90^\circ)$ and (b) $(\psi_1, \psi_2) = (90^\circ, 0^\circ)$.

2.2 FLC-SLM

As already discussed, a LCTV-SLM is very suited for the applications in optical information processing and computing. Because it is inexpensive, it can be used for making rapid prototypes of optical architecture for a preliminary real-time testing. However, the LCTVs are pixelate devices and still operate at frame rates of only ~30 frames per second. In spite of this frame rate and a minimum pixel size of the order of 10 μm, the information processing capacity of these TV systems is still inadequate in some applications for a high-speed real-time information analysis of successive and repeating events such as that for fluid flows or vibrating objects.

In this section, we describe an optically addressed ferro-electric liquid crystal spatial light modulator (FLC-SLM). FLC device has the ability of a time response as faster as 100 μs or more. Therefore, the device will be a promising one for a real-time optical processing.

2.2.1 Structure and Operation Principle

In smectic-C* phase liquid crystals, the molecular orientation is tilted by an angle θ with respect to the normal to the layers (the x axis), as illustrated in Fig. 2.5. The material has ferroelectric properties. When it is placed between two close glass plates, the surface interactions permit only two stable states of molecular orientation at the angles $\pm\theta$, as shown in Fig. 2.5. When an electric field $+E$ is applied in the z direction, a torque is produced that switches the molecular orientation into the stable state $+\theta$ [Fig. 2.5 (a)]. The molecules can be switched into the state $-\theta$ by use of an electric field of opposite polarity $-E$ [Fig. 2.5 (b)]. Thus the cell acts as a uniaxial crystal whose optic axis may be switched between two orientations.

In the geometry of Fig. 2.5, the incident light is linearly polarized at an angle θ with respect to the x axis in the x-y plane. In the $+\theta$ state, the polarization is parallel to the optic

axis and the wave travels with the extraordinary refractive index n_e without retardation. In the -θ state, the polarization is switched to make an angle 2θ from the input polarization. The optical and switching characteristics of the FLC device have been discussed in detail in Refs. 2.7-8.

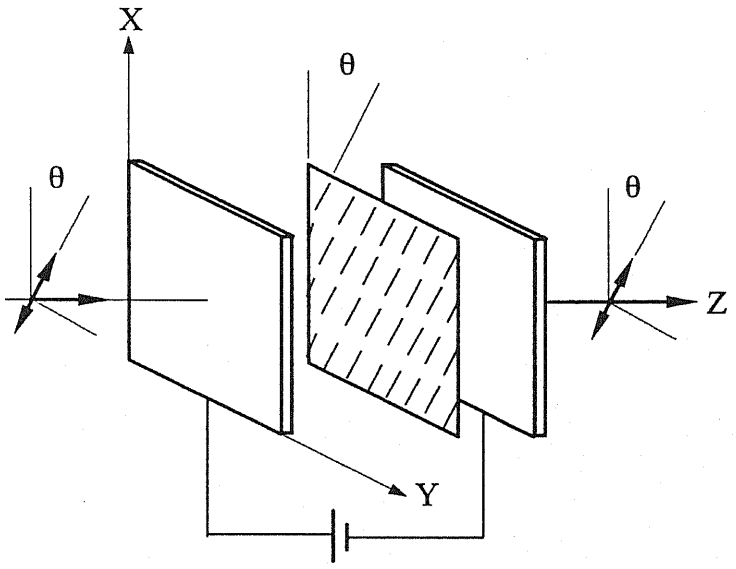

(a)

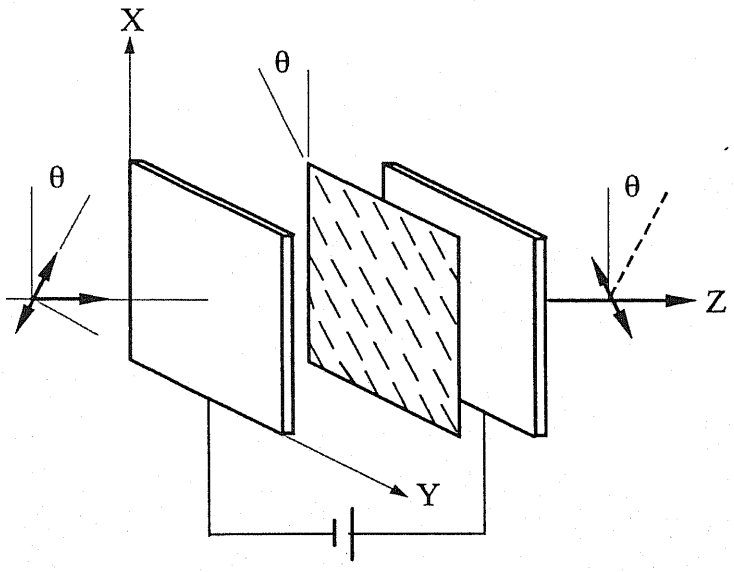

(b)

Fig. 2.5 Two states of a FLC cell.

Figure 2.6 shows a FLC-SLM (fabricated by Hamamatsu Photonics, K.K.)[2.9] that is used in our experiments. The modulation of the readout light beam occurs in ~1 μm thick layer of surface-stabilized chiral smectic-C* FLC material sandwiched between a dielectric mirror and a transparent front electrode. Optical addressing is achieved by varying the impedance of a 3 μm thick photoconductive layer of hydrogenated amorphous silicon (α-Si:H) on the rear side of the dielectric mirror in accordance with the intensity of the write beam. The operation of the FLC-SLM requires the application of a 15 V peak-to-peak amplitude square wave voltage, as shown in Fig. 2.6 (b).

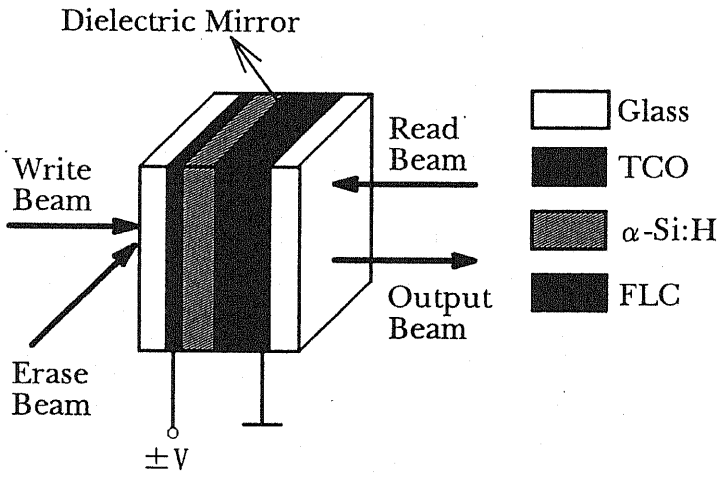

(a)

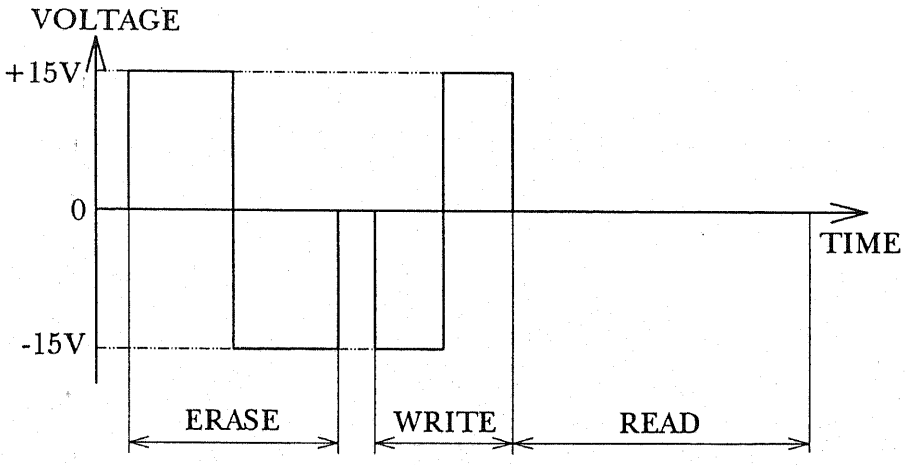

(b)

The dielectric mirror is a critical component of the device, its function is to provide effective reflection of the read beam and to block the read- and write-beam penetrations to the opposite sides. The high reflectivity is important in giving a high optical gain.

Because of the surface stabilization of the liquid crystal layer, the FLC-SLM is a bistable device.[2.10-11] In order to write an image onto the device, it is, at first, necessary to erase any previous information that might be stored in the liquid crystal layer. In principle, this can be achieved by the application of an erase voltage pulse of sufficiently high amplitude between the electrodes of the device such that the electric field across the liquid crystal layer is large enough to cause all parts of the layer to switch to the same alignment condition. In practice, the erasure can be achieved much more rapidly by a uniform illumination for the α-Si:H photoconductor and the simultaneous application of the erase voltage pulse to the electrodes. We adopted this method in our experiments by using a red LED to provide the erase illumination.

After the previous content has been erased, the erase light is switched off and the photoconductive layer is illuminated by the write-in intensity distribution, during which a write voltage pulse of opposite polarity is applied. The write-in intensity distribution is transmitted into the liquid crystal layer during the write voltage pulse (write phase) and the device becomes immune to further changes in the write-in intensity distribution when the voltage drops back down to zero (storage phase). The photoconductive layer is essentially ohmic and, therefore, the erase voltage may be of either polarity, providing that the write voltage pulse is of opposite polarity. Reversing the polarities of the pulses changes the stored image from positive to negative. This is shown in Fig. 2.7. The each letter size was abuot 5×5 mm^2 on the FLC-SLM. For writing in the positive image mode, the responses of this FLC-SLM was 42 μs, whereas it was 43 μs for the negative images.[2.11]

The reflectivity of the FLC-SLM was estimated as 99% in He-Ne laser light of 633 nm wavelength. The reflectivity was measured by writing a totally bright image to the FLC-SLM and, then, determining the ratio of the intensities of the read beam directly after the

incidence with directly before the reflection from the FLC-SLM.

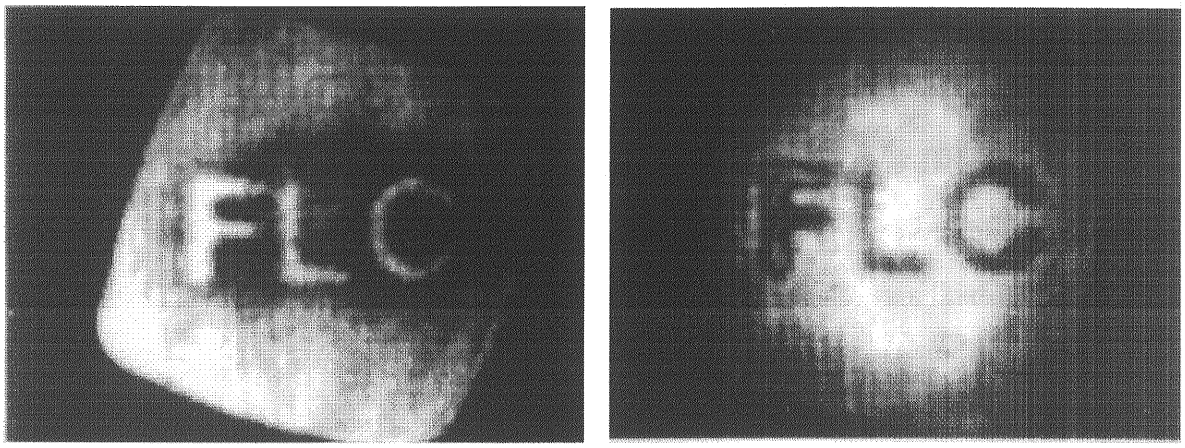

(a) (b)

Fig. 2.7 Images obtained by the FLC-SLM. (a) positive and (b) negative images.

2.2.2 Evaluations of FLC-SLM

(1) Visibility measurement

The visibility of an imaging device is one of measures for the quality of an image produced by system. According to Michelson,[2.10] the visibility is defined as

$$v = \frac{I_{\max} - I_{\min}}{I_{\max} + I_{\min}}, \tag{2.10}$$

where $I_{\max}$ and $I_{\min}$ are the maximum and minimum intensities of the resulting image respectively. The optical system shown in Fig. 2.8 was constituted to measure the visibility o the FLC-SLM used for the later optical processing and computing. A totally dark and brigh binary image was written onto the FLC-SLM and was detected by a photodetector located a

imaging plane P. The output voltages across the photodetector corresponding to the binary image were then measured. From the variation of the intensity measured in plane P the maximum visibility for a sufficiently resolved pattern was estimated to be 0.86. The visibility ν also termed modulation factor.

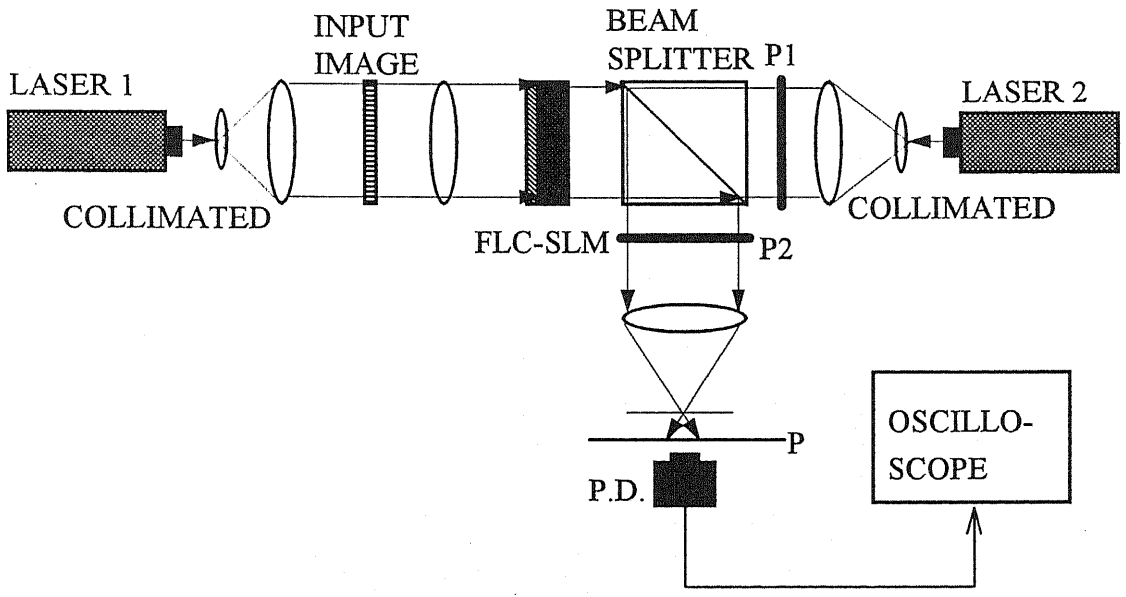

Fig. 2.8 Optical system used to measure the visibility of the FLC-SLM. P1 and P2: polarizers.

The visibility of the optically addressed FLC-SLM will be improved by the use of optical flats, instead of glass plates, for the sandwich structure. The glass plates create an interference pattern in the image plane. These rings increase the average of the background, thus increasing the value of I_{min} observed with the photodetector.

(2) Resolution measurement

We estimated the spatial resolution of the modulator by writing the sinusoidal intensity distribution of different spatial frequencies in a Mach-Zehnder interferometer and measuring the diffraction efficiencies of the grating produced in the liquid-crystal layer with the setup

shown in Fig. 2.9. The diffraction efficiency is defined as[2.11]

$$\eta = \frac{I_{+1}}{I_0}, \tag{2.11}$$

where I_{+1} is the total intensity of the first-order diffraction spot, and I_0 is the intensity of the direct beam with no grating written on the SLM. Figure 2.10 shows the variations of the first-order diffraction efficiency with the spatial frequency. The resolution of the FLC-SLM was determined to be 72 *l*p/mm, and it is the value in which the first-order diffraction efficiency has fallen to half of the maximum value.

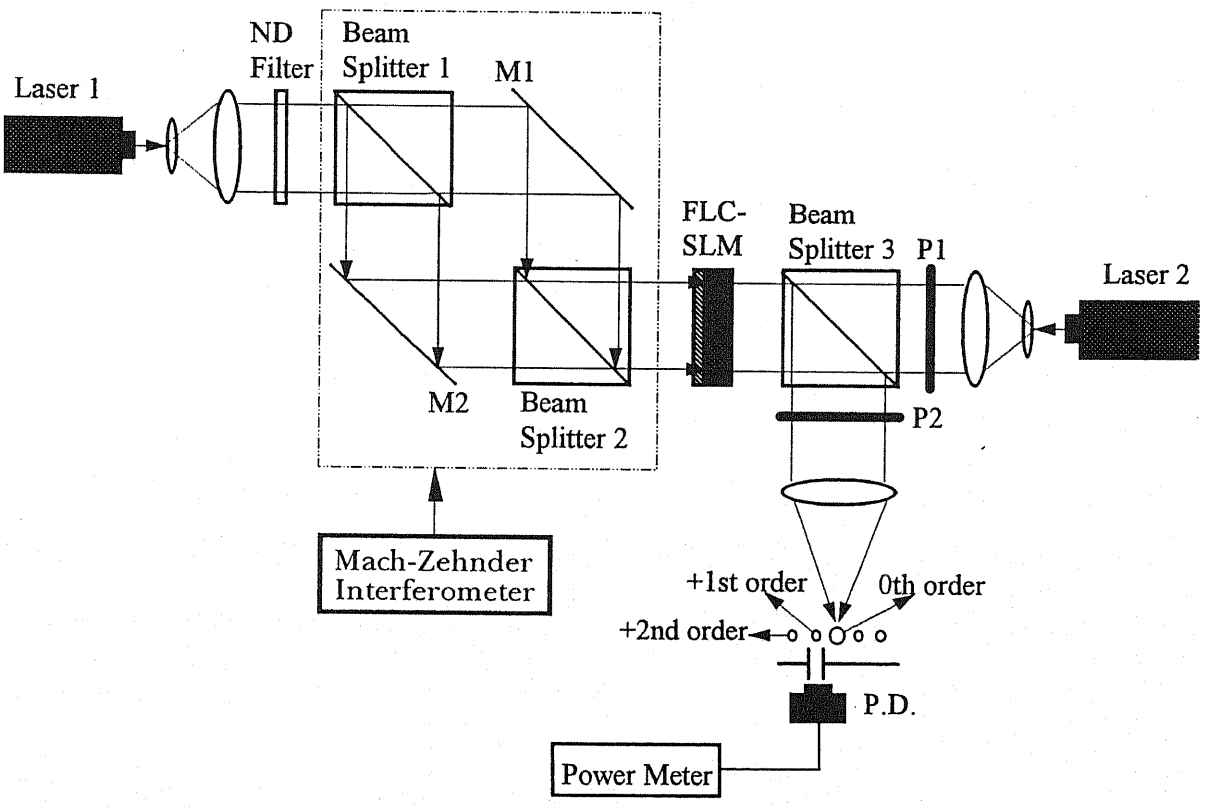

Fig. 2.9 Setup used to measure diffraction efficiencies of gratings written on the FLC-SLM. P1 and P2: polarizers, and ND: neutral-density filter.

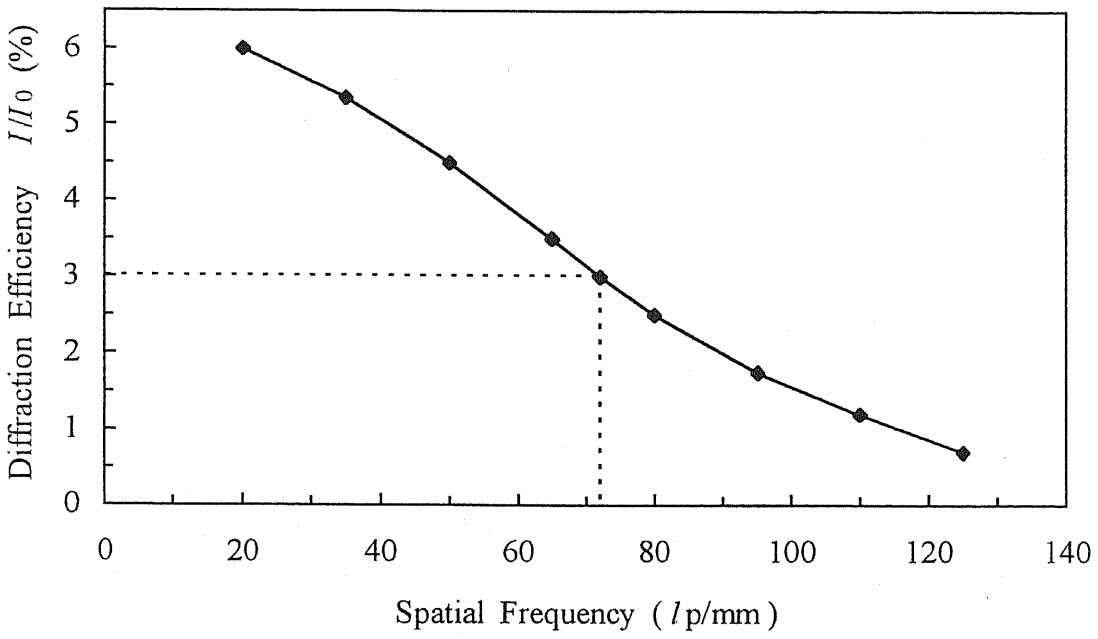

Fig. 2.10 Diffraction efficiency as a function of spatial frequency.

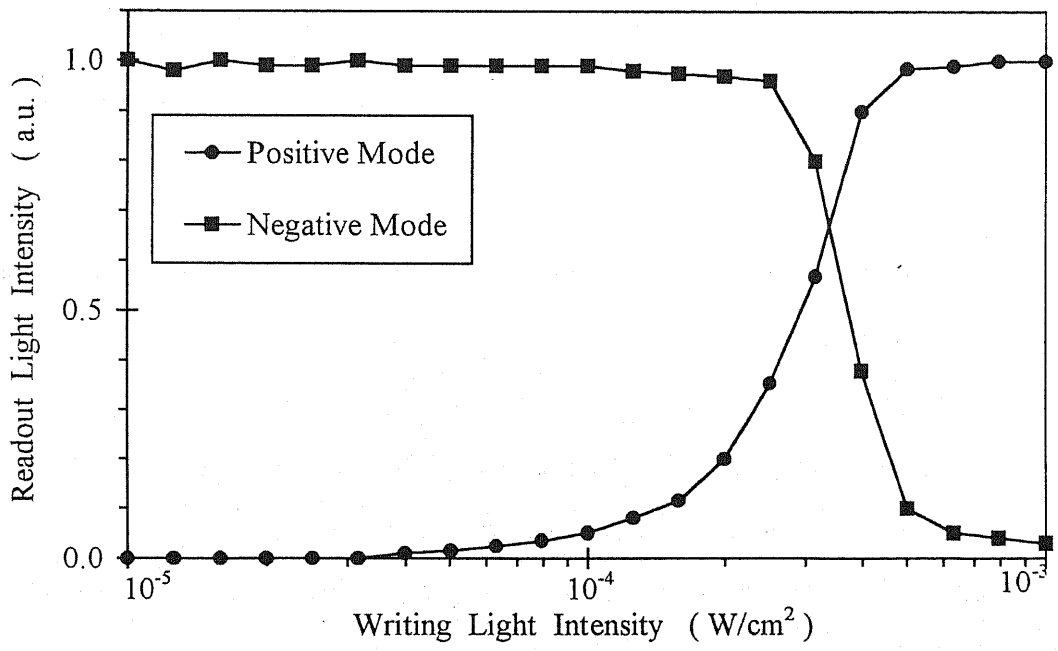

Fig. 2.11 Transmission characteristics of the FLC-SLM.

(3) Transmission characteristics

The transmission characteristics was measured by the same optical system of the visibility measurement. Figure 2.11 shows the transmission characteristics of the FLC-SLM in positive and negative contrast modes for images written by a He-Ne laser light at 633 nm wavelength.

(4) Multiple exposure properties

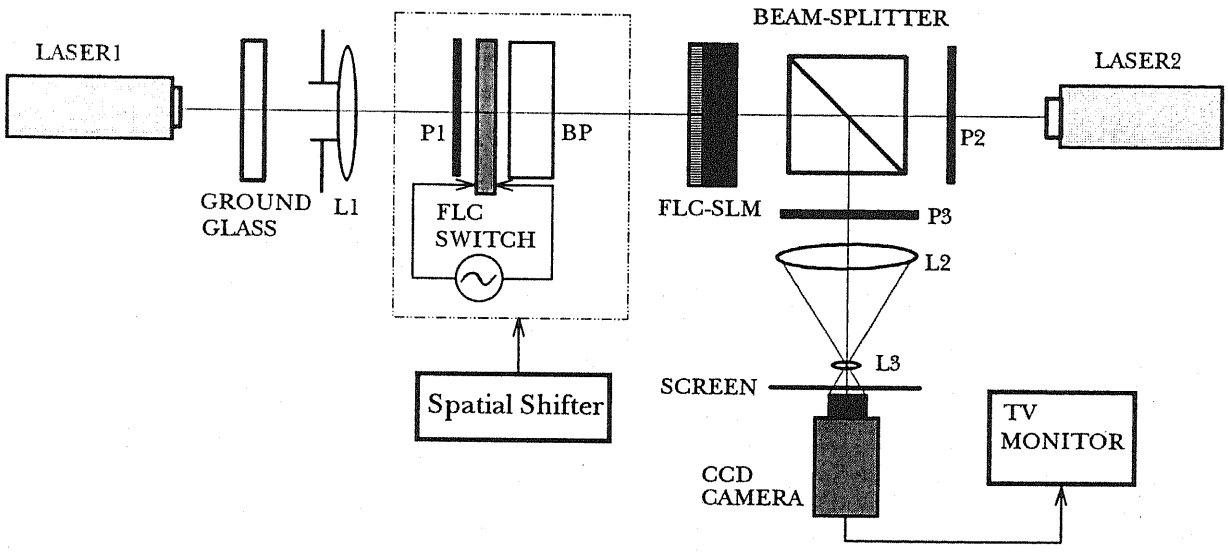

Fig. 2.12 Optical system for double-exposure property of speckle patterns. BP: birefringent plate and P1~P3: polarizers.

The important feature of the FLC-SLM is the capability of multiple exposures for input patterns. A system for double exposures by using speckle patterns is shown in Fig. 2.12. A speckle pattern is generated by a ground glass plate and, then, it is imaged onto the FLC-SLM through a spatial shifter consisting of a FLC polarization switch and a birefringent plate. By using this spatial shifter, a spatial offset between the successive exposures of the same speckle pattern is given. This spatial shifter unit will be discussed in detail in Section 3.3. The output

om FLC-SLM is a new speckle pattern which is a random distribution but has pairs of two ɔeckles. In each pair, one of the grains belongs to the first exposure and the other grain elongs to the second exposure of the identical but displaced speckle. The pair of speckles acts ; two small, identical, coherent sources and the Young's fringes are formed by the Fourier ansform in the back focal plane of the L2. The same interference fringe is produced by each air of grains. In the experiment, the fringe patterns of the speckles were taken by the CCD ımera and was shown on a TV monitor. An example of fringe patterns due to displaced ɔeckles recorded on the FLC-SLM is shown in Fig. 2.13.

There are two possible drives of the FLC-SLM to write a doubly exposed pattern on ıe SLM; one is optical and the other is electrical. In the optical writing mode, the electrical rite-in signal for the FLC-SLM is turned on during a certain time duration. Within this uration, the optical signal pulses are sequentially switched on and the double exposure pattern formed by these pulses as shown in Fig. 2.14 (a). These optical pulses may be generated by n opto-electronic shutter such as a FLC switch used in this experiment. On the other hand, in ıe electrical mode, the FLC-SLM is constantly exposed by the optical signal during the ıccessive exposures. Two writing electrical pulses are successively generated at a certain ppropriate time interval as shown in Fig. 2.14 (b). Then the doubly exposed pattern can be btained after the second pulse.

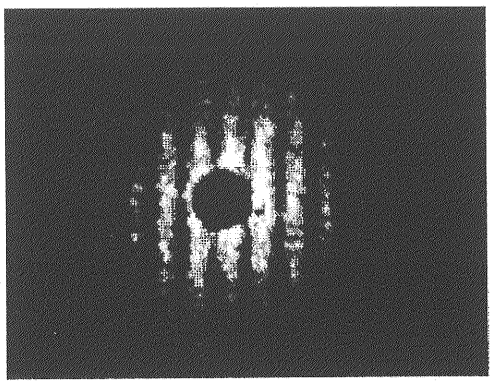

Fig. 2.13 Example of fringe patterns by the double exposures.

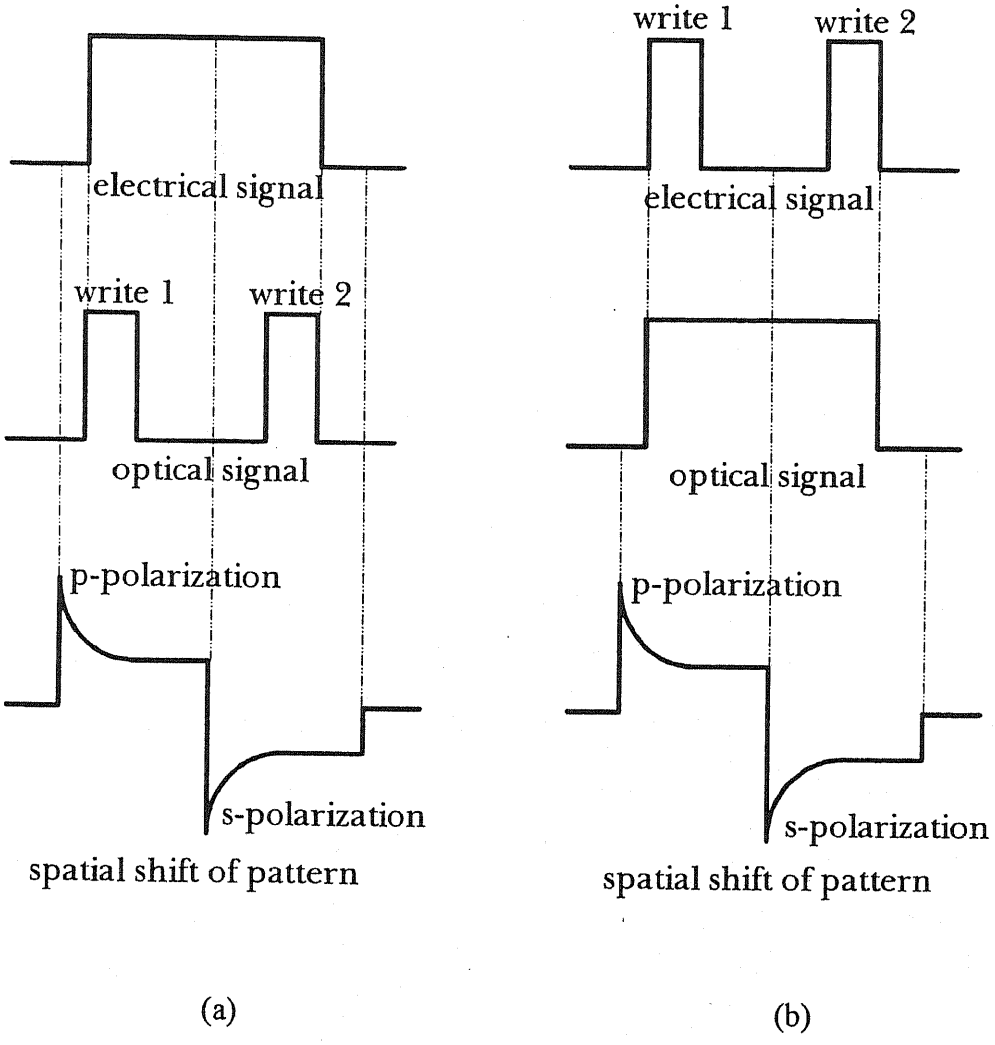

Fig. 2.14 Operation modes of the double exposures. (a) optical mode and (b) electrical mode.

Figure 2.15 shows the double-exposure properties of the two mode. In Fig. 2.15 (a), the exposure spatial offset is changed but the exposure time is fixed as 150 μs. The exposure time is variable but the exposure offset is fixed 1000 μs in Fig. 2.15 (b). These results indicate that the FLC-SLM has a optimum exposure range both in space and in time offset, and good visibility is obtained for the optical writing mode because of a little blurred effect of the pattern taken by the FLC-SLM.

The performance characteristics of the FLC-SLM which is used in the experiment are summarized in Appendix A.

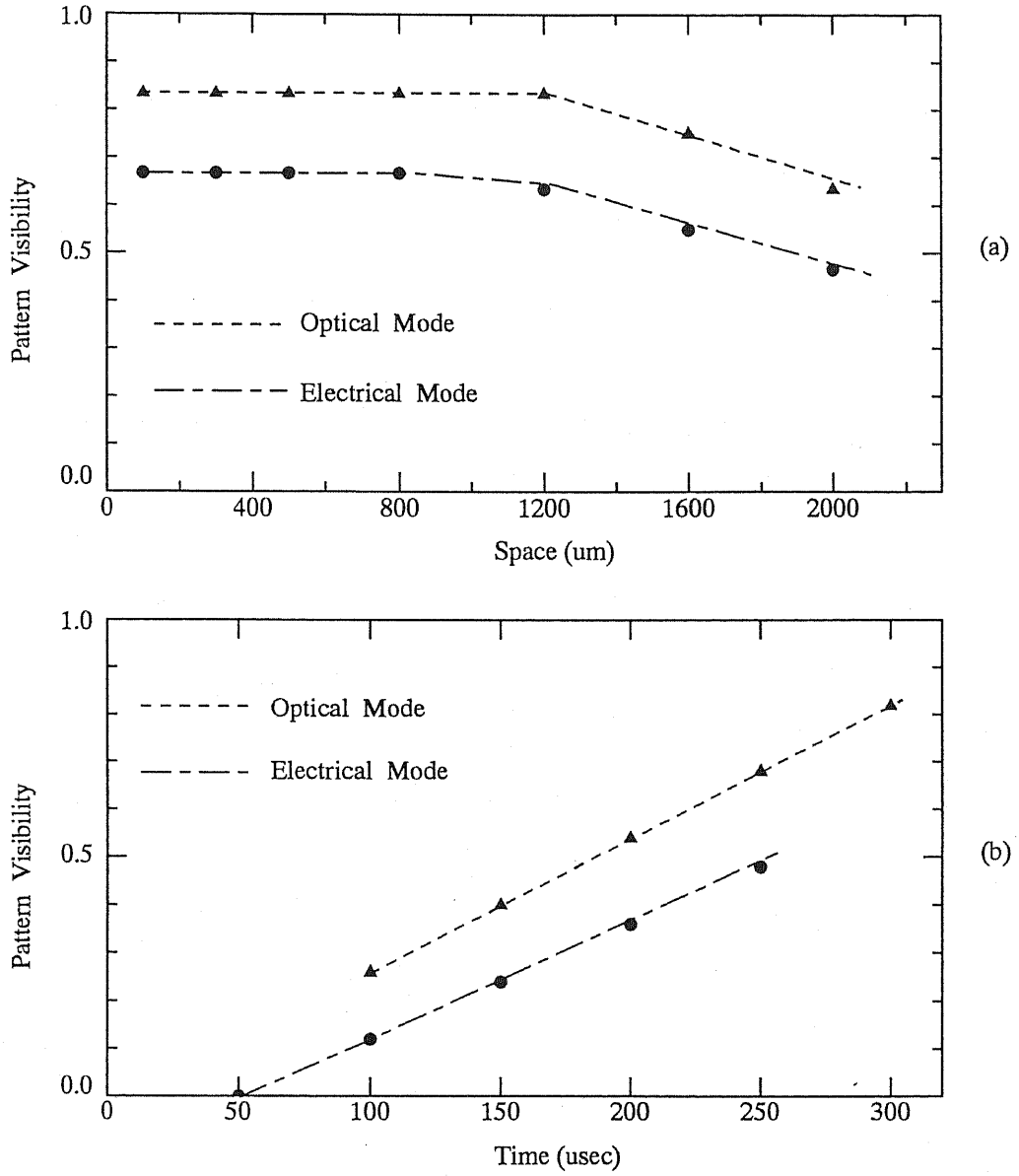

Fig. 2.15 Double-exposure properties for the two modes for (a) the spatial offset and for (b) the time offset.

2.3 SUMMARY

We have described the operation capabilities of LCTV- and FLC-SLMs. The advantages of these liquid crystal SLM's are their fast response time, high sensitivity, low-power operation, high spatial resolution, and so on. Moreover, the LCTV has been recently used in the field of optical information processing because of the low cost of the device and the ease of the commercial availability. On the other hand, FLC-SLM has the excellent features of multiple exposure capability of images, much larger data throughput, and the great potential for further, real-time, optical processing.

REFERENCES

2.1 D. A. Gregory, *Appl. Opt.* **25**, 467 (1985).

2.2 K. D. Hughes, S. K. Rogers, J. P. Mills, and M. Kabrisky, *Appl. Opt.* **26**, 1042 (1987).

2.3 P.G.de Gennes, *The Physics of Liquid Crystals*, Chap. **3**, Clarendon Press, Oxford (1975).

2.4 K. Lu, and B. E. A. Saleh, *Opt. Eng.* **29**, 240 (1990).

2.5 A. Ogiwara, H. Sakai, and J. Ohtsubo, *Opt. Commun.* **86**, 513 (1991).

2.6 T. H. Barnes, T.Eiju, K. Matsuda, and N. Ooyama, *Appl. Opt.* **28**, 4845 (1989).

2.7 G. Moddel, C. T. Kuo, K. M. Johnson, and W. Li, *Mat. Res. Soc. Symp. proc.* **118**, 405 (1988).

2.8 G. Moddel, K. M. Johnson, W. Li, R. A. Rice, L. A. Pagano-Stauffer, and M. A. Handschy, *Appl. Phys. Lett.* **55**, 537 (1989).

2.9 S. Fukushima, T. Kurokawa, and M. Ohno, *Appl. Opt.* **31**, 899 (1992).

2.10 M. Born, and E. Wolf, *Princiles of Optics*, **6th** ed. p.267 (Pergamon, New York, 1980).

2.11 Y. Kobayashi, T. Takemori, N. Mukohzaka, N. Yoshida, and S. Fukushima, *Appl. Opt.* **33**, 2785 (1994).

A method for the generation of a joint pattern to calculate a real-time joint transform correlation for speckle applications is proposed. A real-time optical joint transform correlator for displacement or velocity measurement in speckle applications by using proposed method is described. The successive patterns from a light scattering object before and after the displacement pass through a liquid crystal polarization switch and a birefringent plate. The generation of the joint pattern is verified by the experiment. It is possible to perform a real-time all optical joint transform correlation based on the proposed method. The velocity measurement up to 100 mm/s is realized at moderate operations of ferroelectric devices.

CHAPTER 3

REAL-TIME OPTICAL SPECKLE METROLOGY

Speckle photography and speckle interferometry have been developed since early 1970s as a means for non-contact assessment of displacements, tilts, contours and other surface characteristics of solid objects.[3.1] This work also led to the development of particle image velocimetry (PIV)[3.2] which measures fluid velocities in two-dimensional flow fields.

The recent techniques used for optical pattern recognition and optical speckle metrology may be broadly classified into the VanderLugt-type filter-based correlation[3.3] and the joint transform correlation (JTC).[3.4] The VanderLugt-type correlator requires a priori fabrication of the filter used in the correlation process, thereby prohibiting real-time operation. In addition, the filter must be accurately aligned along the optical axis in the Fourier plane and the technique requires close positioning between the filter and the Fourier transform of the input. On the other hand, the joint transform correlator can be operated at video frame rates[3.5] and it has several features that make them an attractive optical information processing architecture as follows:

1. they are relatively insensitive to optical alignment errors compared with other Fourier based correlators;
2. a complex-valued SLM is not required in the Fourier plane;
3. a priori knowledge of the reference image is not necessary;
4. JTC can be compactly designed.

Optical joint transform correlators have been demonstrated with a variety of opto-electronic devices.[3.6-3.11] Obviously, the JTC is a powerful tool for such as an object identification or a displacement measurement.

3.1 THEORY OF THE JTC

The JTC was introduced by Weaver and Goodman for the first time as an architecture for performing optical correlations.[3.4] This technique differs from classical matched filtering in that it dose not require the synthesis of a frequency plane filter. Consider two image functions

$f(x+x_0,y)$ and $g(x-x_0,y)$ in the geometry shown in Fig. 3.1 (a). The intensity of the Fourier transform of the two images is given by

$$\begin{aligned} I(u,v) &= \left|\mathcal{F}[f(x+x_0,y)+g(x-x_0,y)]\right|^2 \\ &= \left|F(u,v)\exp(-i2\pi ux_0)+G(u,v)\exp(i2\pi ux_0)\right|^2 \\ &= F(u,v)F^*(u,v)+G(u,v)G^*(u,v) \\ &\quad +F(u,v)G^*(u,v)\exp[-i2\pi u(2x_0)] \\ &\quad +G(u,v)F^*(u,v)\exp[i2\pi u(2x_0)], \end{aligned} \tag{3.1}$$

where $\mathcal{F}$ is the Fourier transform operator and the capital letters denote the Fourier transform of the lower letter functions. The output of the JTC $c(x,y)$ is given by performing an inverse Fourier transform of the intensity distribution of Eq. (3.1),

$$\begin{aligned} c(x,y) &= \mathcal{F}^{-1}[F(u,v)F^*(u,v)]+\mathcal{F}^{-1}[G(u,v)G^*(u,v)] \\ &\quad +\mathcal{F}^{-1}\{F(u,v)G^*(u,v)\exp[-i2\pi u(2x_0)]\} \\ &\quad +\mathcal{F}^{-1}\{G(u,v)F^*(u,v)\exp[i2\pi u(2x_0)]\}. \end{aligned} \tag{3.2}$$

Then, the output of the correlator is calculated by

$$\begin{aligned} c(x,y) &= f(x,y)\otimes f(x,y)+g(x,y)\otimes g(x,y) \\ &\quad +f(x+2x_0,y)\otimes g(x,y) \\ &\quad +f(x-2x_0,y)\otimes g(x,y), \end{aligned} \tag{3.3}$$

where $\otimes$ denotes a correlation operation.

The output plane geometry of the JTC is readily recognized by Eq. (3.3). The output plane is divided into three regions as shown in Fig. 3.1 (b). The central region corresponds to the first two terms in Eq. (3.3) and contains the overlapping auto-correlations of $f(x,y)$ and $g(x,y)$. The side regions correspond to the last two terms in Eq. (3.3) and contains the cross-correlation between $f(x,y)$ and $g(x,y)$.

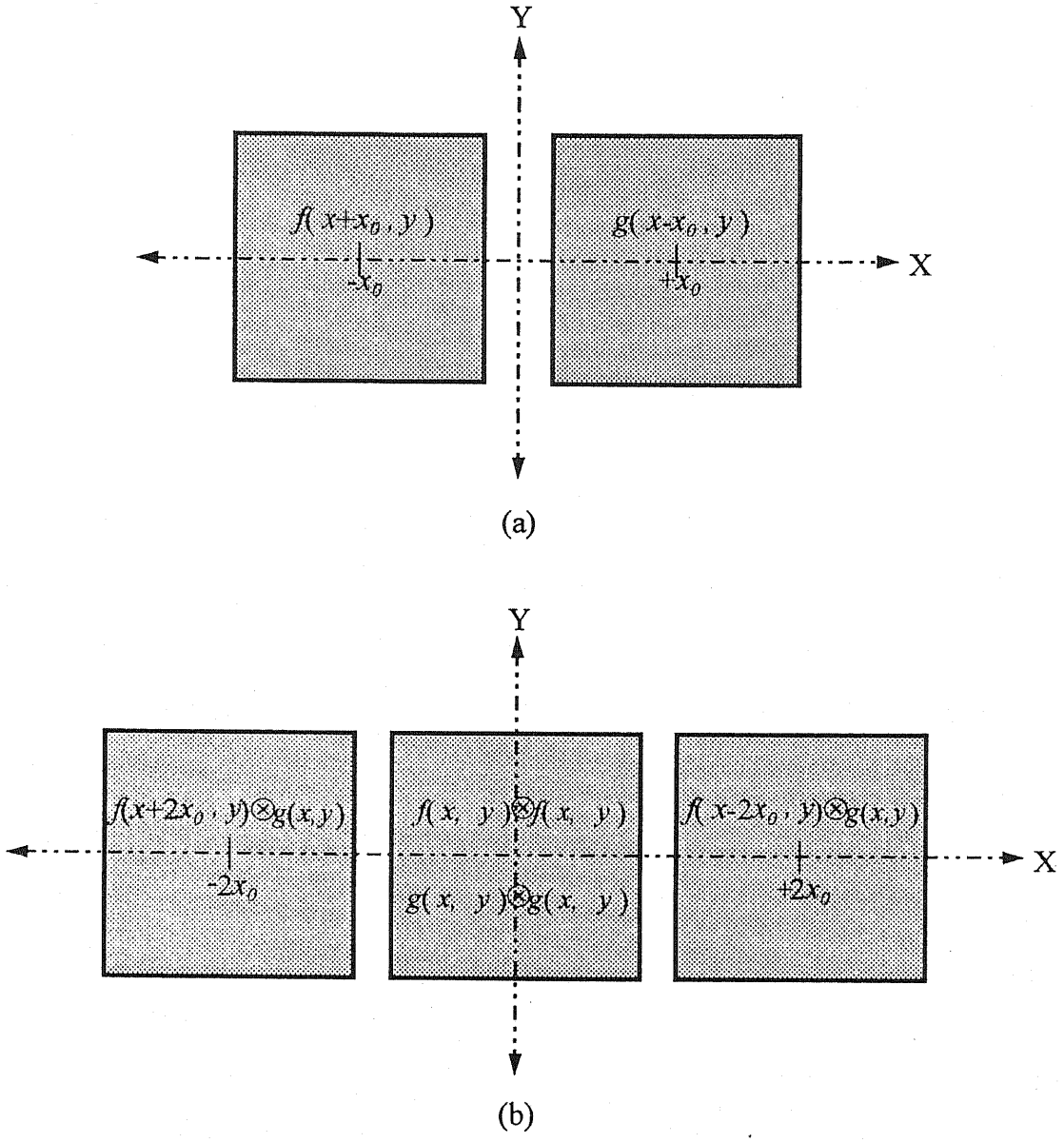

Fig. 3.1 Input plane (a) and output plane (b) of the JTC.

3.2 OPTICAL SPECKLE JTC USING A TN-LC CELL AND A BIREFRINGENT PLATE

Optical JTC techniques in speckle phenomena are well known and have been used for

determining surface displacement, deformation, rotation, and tilt. Though many papers have been published for the optical joint transform correlator, the optical implementation to calculate only the correlation function and/or the evaluation of only the output performance of the JTC are the main concerns in those papers.[3.11-12] Most of the papers have not mentioned how to generate a joint pattern for the real-time optical processing. In the usual case, a joint pattern was synthesized by computer software and the generated pattern was displayed on a TV monitor or taken as a master photographic film for the correlation input. It is difficult to implement real-time optical processing by those methods. In practice, how to generate or acquire a joint pattern is the key point to realize the fast "real-time" JTC.

Recently, a real-time optical joint transform correlator for speckle displacement or velocity measurement has been proposed by using an Optic RAM detector and a LCTV.[3.13-16] In the previous papers, the doubly exposed joint pattern was obtained electronically by the Optic RAM device. After the detection of the joint pattern, the cross-correlation function was optically calculated by using a LCTV-SLM. A joint pattern can be formed rather faster than the conventional method by use of the Optic RAM detector. But, because of the sequential read-out of the memory contents of the Optics RAM, it is not still in sufficient to realize a "real-time" optical correlator in many applications which require a fast processing of the signal.

As an alternative or more efficient method to produce a joint pattern, we propose a new method to form a joint pattern for speckle applications in this section. The joint pattern before and after the displacement of a light scattering object is formed through a spatial shifter consisting of a TN-LC cell and a birefringent plate with a polarization plate. The generation of the joint pattern is verified by the experiment. In this section, to confirm the usefulness of the method, the joint pattern of the speckle patterns is generated in real time and taken by a CCD camera. Then, the JTC function is calculated by a computer. It is possible to implement a real-time correlator based on the proposed method together with such as the previously proposed LCTV-based optical correlation technique.[3.15]

3.2.1 Principles of the Method

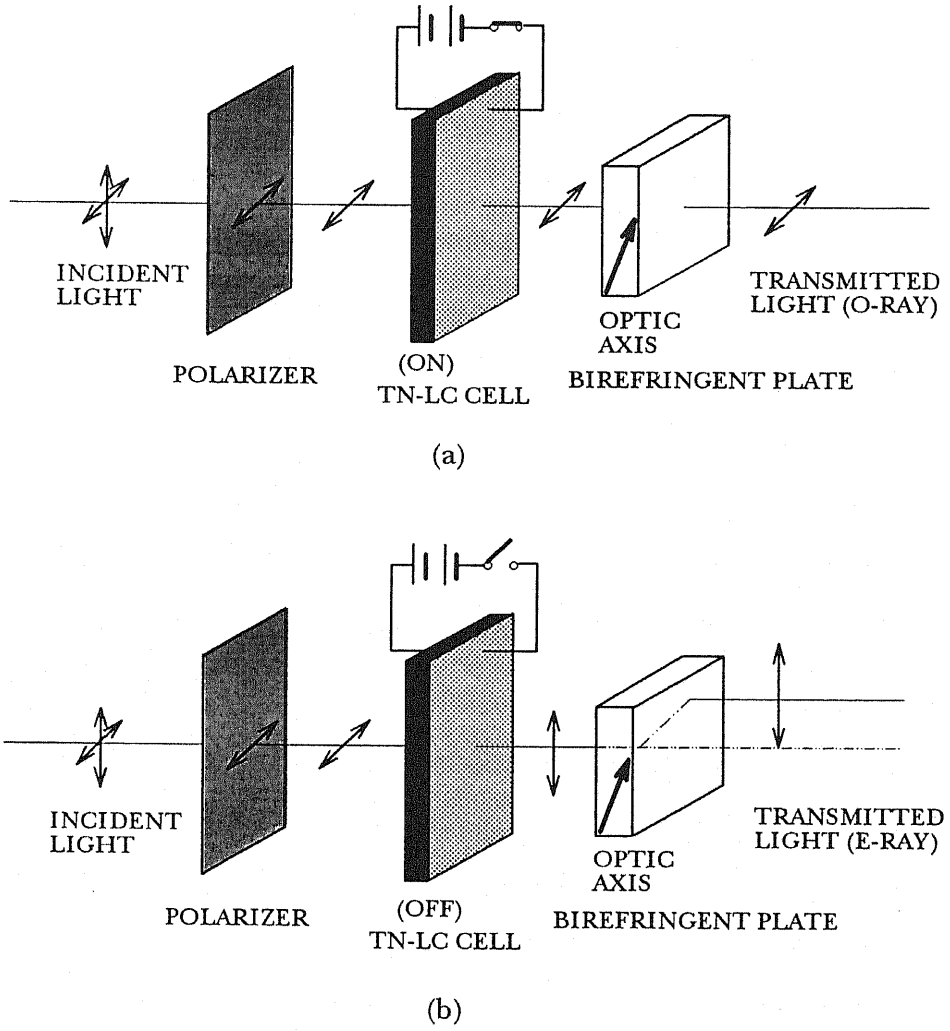

Fig. 3.2 Principle operation of the spatial shift.

The main elements of the module to produce a spatially shifted joint pattern are a 90° TN-LC cell and a birefringent calcite ($CaCO_3$) plate. By using this module, a spatial offset between the successive two speckle patterns can be easily and quickly given. For example, we consider the situation where an s-polarized pattern as shown in Fig. 3.2 passes through a TN-LC cell.

The director of the LC molecules at the front surface in Fig. 3.2 is chosen to be aligned to the same direction as the s-polarization of the incident light. The polarization of the pattern remains unchanged when the voltage is applied to the TN-LC cell, because the twist of the molecules is dissolved and the director of the LC molecules is aligned to the direction of the light propagation.

On the other hand, it is rotated 90° when no voltage is applied, since the polarization rotates along the rotation of the molecule directors. Then the polarization of the pattern is switched from s- to p-state. To give a spatial shift to the second pattern, a birefringent plate is inserted behind the TN-LC cell. If the optic axis of the birefringent crystal is lying at the same plane as the p-polarization as shown in Fig. 3.2 (a), the transmitted beam through the plate becomes an o-ray and no spatial shift of the pattern occurs. At the same optic axis, however, the s-state of the polarization becomes an e-ray after passing through the birefringent plate as shown in Fig. 3.2 (b) and, thus, a certain amount of the spatial shift is given to the pattern. The amount of the transverse shift depends on the length of the crystal along the transmission. In the experiment, a spatial shifter consisting of a TN-LC cell and a birefringent plate is inserted in front of a CCD camera to detect speckle patterns and the pattern before and after the displacement of a light scattering object are taken by the CCD camera. The whole operation of the experimental system is described in the following subsection.

3.2.2 Experiments and Results

To demonstrate the effectiveness of the method, we have only shown the principle of the spatial shift of patterns. The real-time JTC based on this method will be presented in the next section.

The schematic diagram of speckle detection and the calculation of the correlation function is shown in Fig. 3.3. A collimated light beam from a He-Ne laser illuminates a moving ground glass plate. The speckle patterns are detected by a CCD camera through a two-lens

imaging system with a pinhole at the filter plane. The spatial shifter unit which is composed of a polarizer, a TN-LC device, and a birefringent plate, is inserted in front of the CCD camera. The two-lens imaging system was employed because of the small decorrelation of the speckle for the translation of the pattern at the detection plane[3.17]. The pinhole controls the speckle size on the detector. The focal length of the lenses L1 and L2 are 100 and 130 mm, respectively, and the size of the pinhole used in the experiment is 0.75 mm, so that the average size of the speckles at the detector plane is calculated to be 0.134 mm. Then the speckle size corresponds to about 6 pixels of the CCD element.

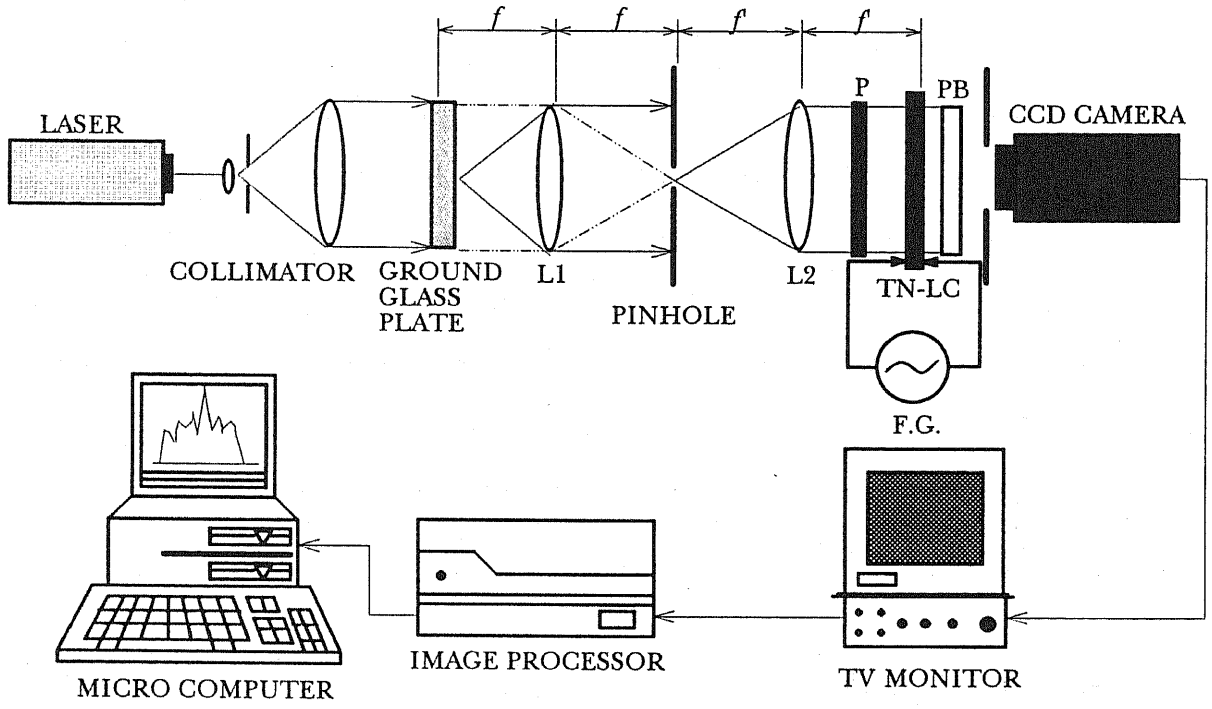

Fig. 3.3 Schematic diagram of speckle detection and processing. L1 and L2: lenses, P: polarization filter, TN-LC: TN-LC cell, BP: birefringent plate, and F.G.: function generator.

The 90° TN-LC cell has an aperture of 2.0×2.0 cm^2 and is driven by a sinusoidal signal from a function generator. The switching speed of the TN-LC is rather slow and is about

100 ms at the applied voltage of 5.0 V. The birefringent calcite plate has also a clear aperture of 2.0×2.0 cm^2 and a thickness of 9.19 mm which corresponds to the shift of e-ray of 1 mm at the wave length of λ=0.633 μm. The module is placed in front of the CCD camera with a polarization filter which enables the polarization of the pattern to be s-polarized state as shown in Fig. 3.2.

By applying the voltage to the TN-LC cell, the first speckle pattern is taken by the CCD camera. Then, after a certain time offset, the voltage is turned off and the second speckle pattern is detected. The second pattern is spatially shifted from the first pattern due to the applied voltage to the TN-LC cell even if there is no displacement of the object. During the successive exposures, the pattern moves for a certain direction in actual speckle measurements. Therefore, the displacement of the speckle is added to the spatial offset. The speckle pattern is digitized 512×512 pixels with an 8-bit gray scale through an image grabber controlled by a computer. In the actual calculation of the correlation function, this image was reduced to the size of 128×128 pixels and the calculation was performed with 128×128 pixels by the computer. The detected speckle pattern before and after the displacement of the object are sent to the memory of the computer. The speckle patterns are clipped to have a binary level at the mean intensity because we can obtain a sharp correlation function which enables the accurate detection of the correlation peak. Then the joint pattern is produced in the computer. The joint pattern is something like a specklegram but it should be distinguished from an ordinary specklegram because a certain spatial offset is given between the successive speckle pattern. Then, the correlation function is calculated by employing a two-dimensional fast Fourier transform (FFT) method by the computer.

Figure 3.4 shows the speckle pattern with and without the applied voltage to the TN-LC cell taken by 512×512 pixels with an 8-bit gray scale (before the clipping of the pattern) when the ground glass plate is stationary. As is seen from this figure, the speckles in Fig. 3.4 (a) shift horizontally to the right direction in Fig. 3.4 (b). Therefore, the distance of the corresponding speckle pairs between Figs. 3.4 (a) and (b) becomes the spatial offset in speckle

lisplacement or velocity measurement. To show the shift more clearly, the same frame of each peckle pattern in Figs. 3.4 (a) and (b) is scanned and each intensity distribution is displayed in ig. 3.5. Figure 3.6 shows the cross-correlation intensities distribution between Figs. 3.5 (a) nd (b).

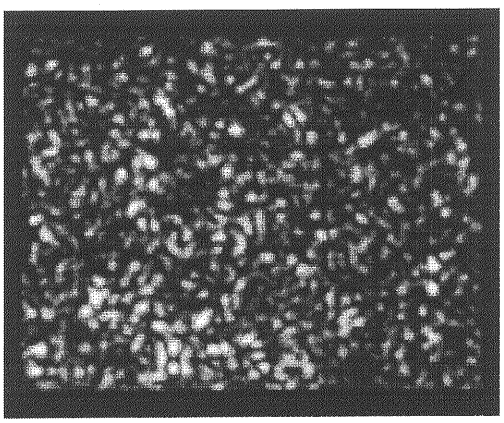

(a)

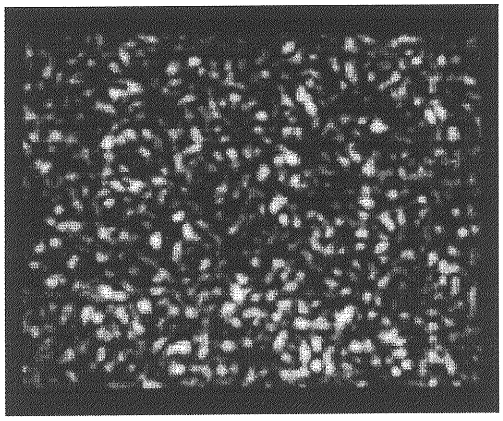

(b)

ig. 3.4 Speckle patterns (a) with and (b) without an applied voltage to the TN-LC cell. The bject is stationary.

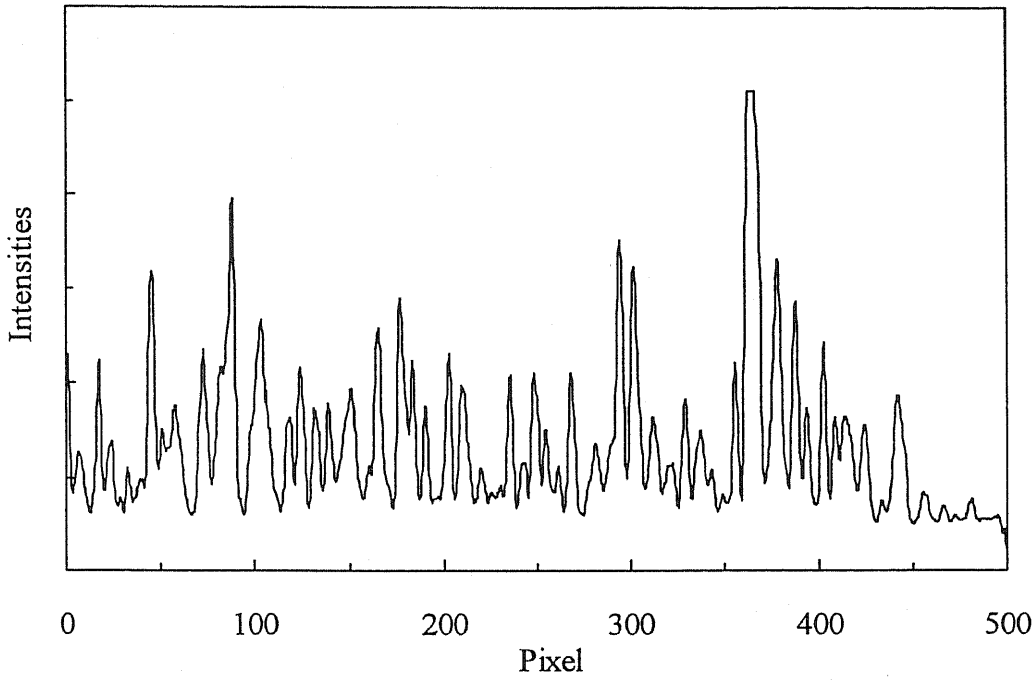

(a)

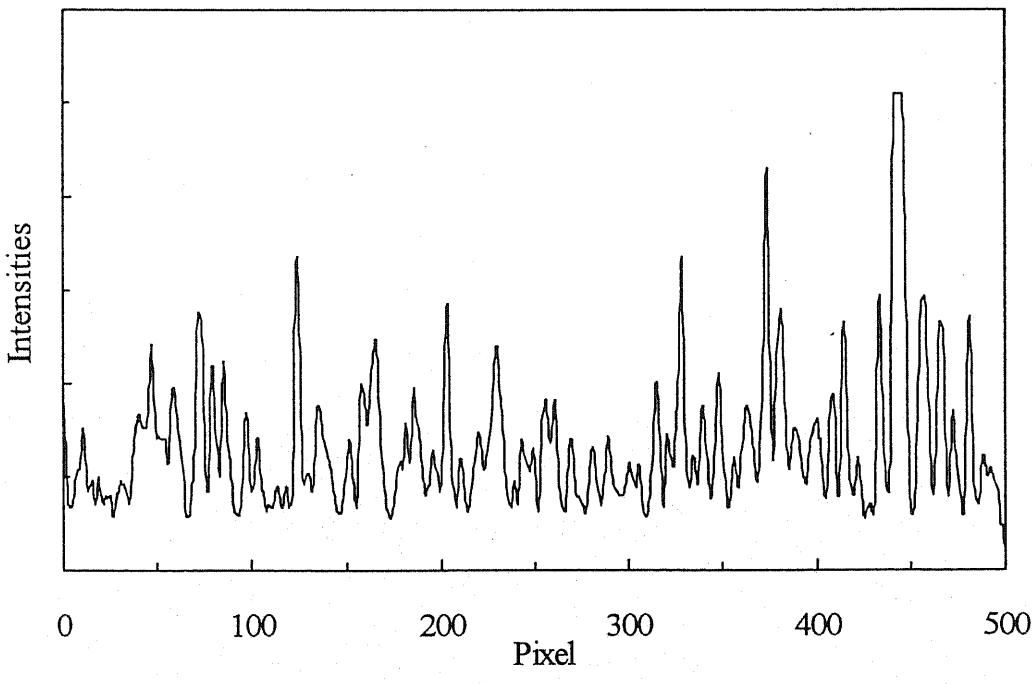

(b)

Fig. 3.5 One-dimensional scan for the intensity of each speckle pattern shown in Figs. 3.4 (a) and (b).

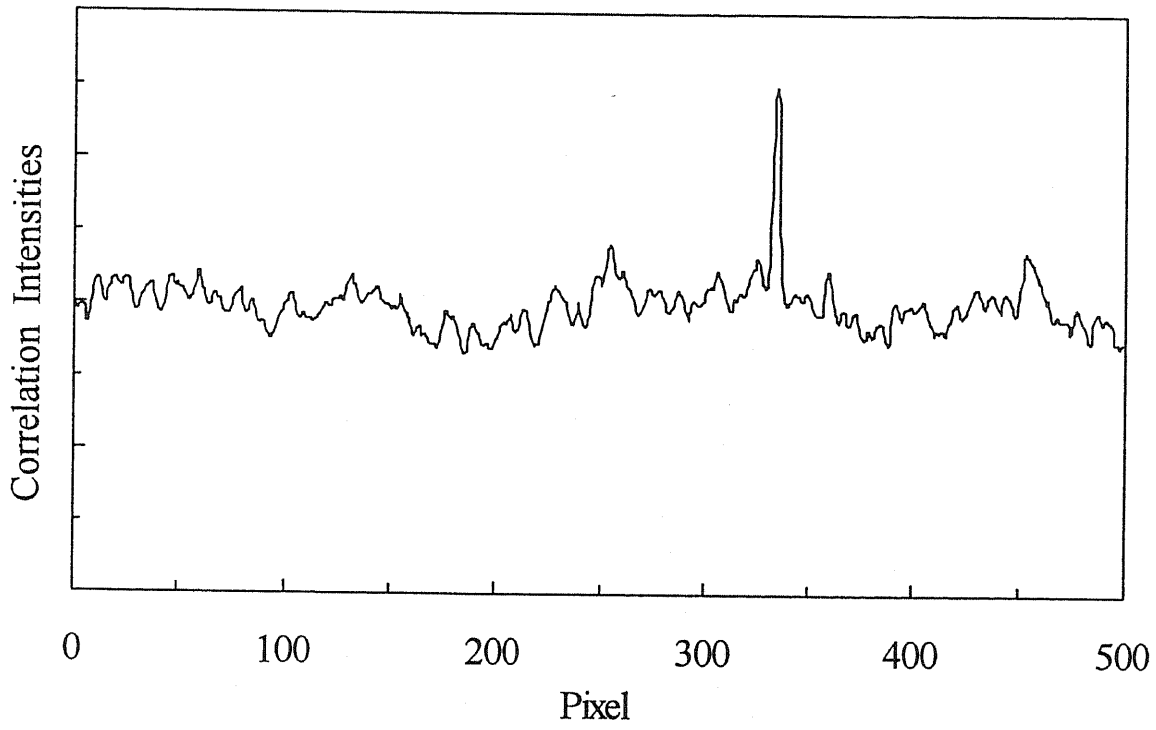

Fig. 3.6 The cross-correlation between the intensity distributions in Figs. 3.5 (a) and (b).

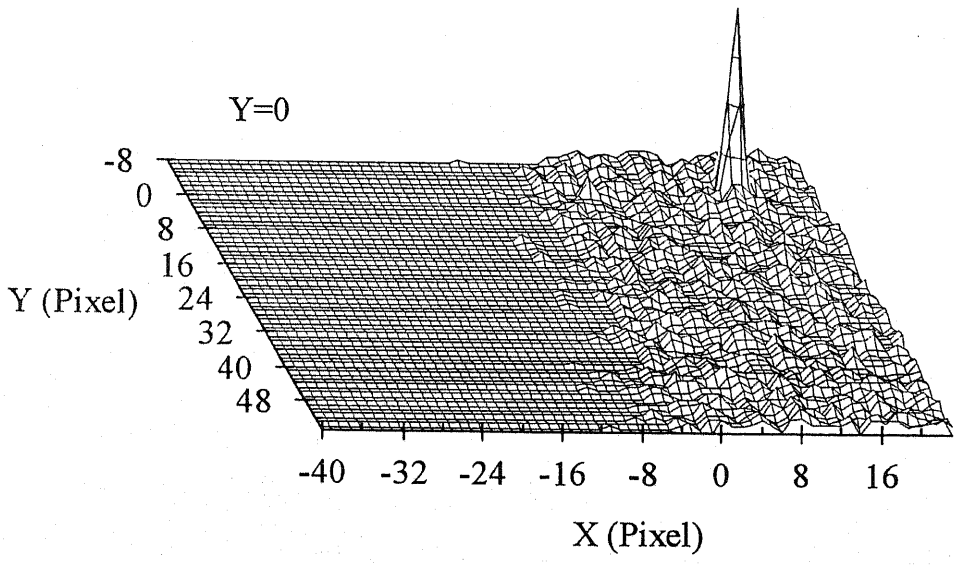

Fig. 3.7 Joint transform correlation with no displacement of the object.

Figure 3.7 shows the calculated joint transform correlation function of the clipped specklegram by the computer when the object is stationary. The quarter of the area (i.e. 64×64 pixels) for the calculated correlation function is plotted in this figure. The origin of the X-Y coordinate corresponds to the correlation peak of the stationary speckle pattern without the spatial shifter. The correlation peak shift 14 pixels from the center of the coordinate to the X direction, which the shift to the Y direction is zero. Then, the position of the shifted correlation peak in Fig. 3.7 becomes a new origin for the speckle displacement measurement in the proposed method of the joint transform correlation.

The joint transform correlation function are shown in Fig. 3.8 when the object is displaced along the Y direction (the X component is set to be zero). The values of the displacement are 0.2, 0.5, and 1.0 mm from Figs. 3.8 (a) to (c), respectively. The correlation peaks also move to the Y direction. As is well known, the speckles move over the several mean speckle sizes with remaining the peak value unchanged due to the employment of the two-lens imaging system, namely, the decorrelation of speckle pattern is small over a wide range of the speckle translation. Furthermore, due to the clipping effect of the speckle intensities, the correlation function is sharpened compared with the ordinary full-bit correlation function. This effect makes it easy to detect the peak position with high accuracy.[3.18-20]

From the obtained correlation function such as shown in Fig. 3.8, the distances of their peak positions from the correlation peak in Fig. 3.7, i.e. the new origin, are plotted against the actual displacement of the object. The result is shown in Fig. 3.9. As is seen from this figure, there is a good linear relation between the peak positions and the object displacements. One of the main features of this method is that the direction of the displacement can be detected from the direction of the correlation peak. In this case, the correlation peak, i.e. the speckles, moves to the positive direction in the Y coordinate (while the X component of the displacement is zero), so that it is concluded the object actually moves to the negative Y direction in the object plane due to the employed imaging geometry. Thus, the two-dimensional measurement for the displacement or velocity of the light scattering object can be carried out by using the proposed method.

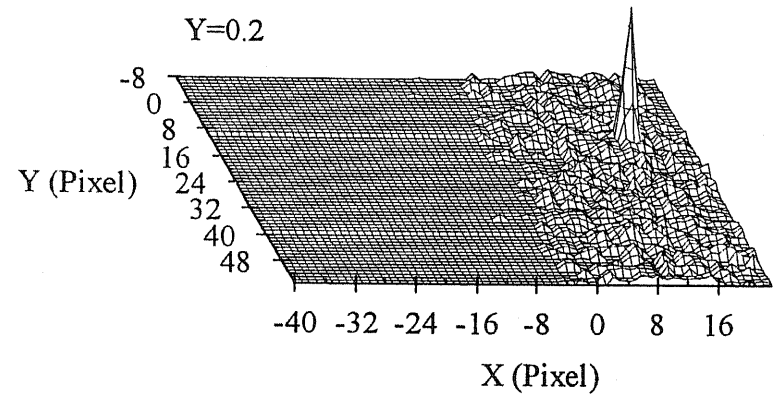

(a)

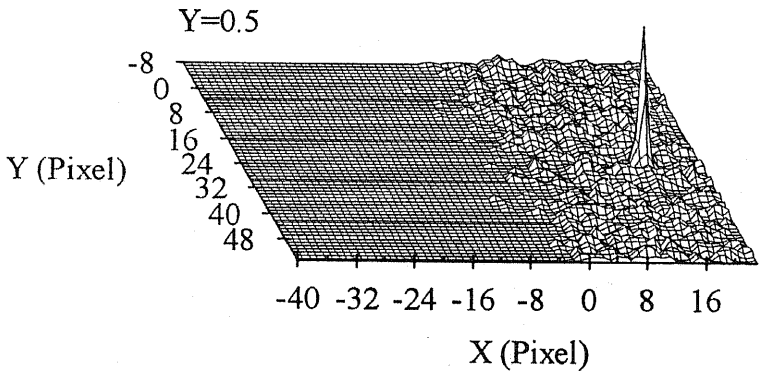

(b)

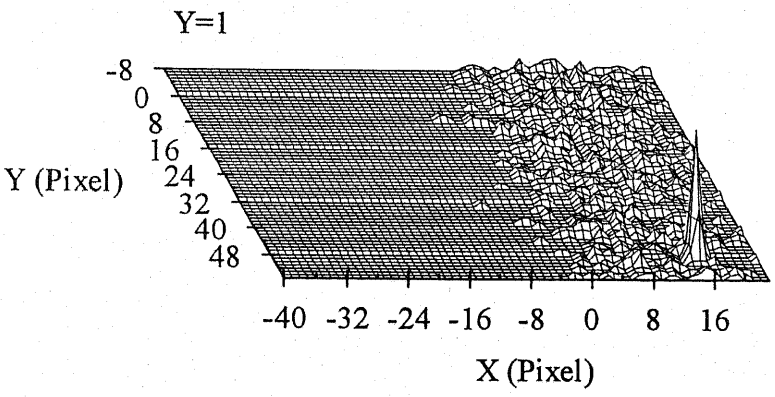

(c)

Fig. 3.8 Joint transform correlations for the displacements of the object.

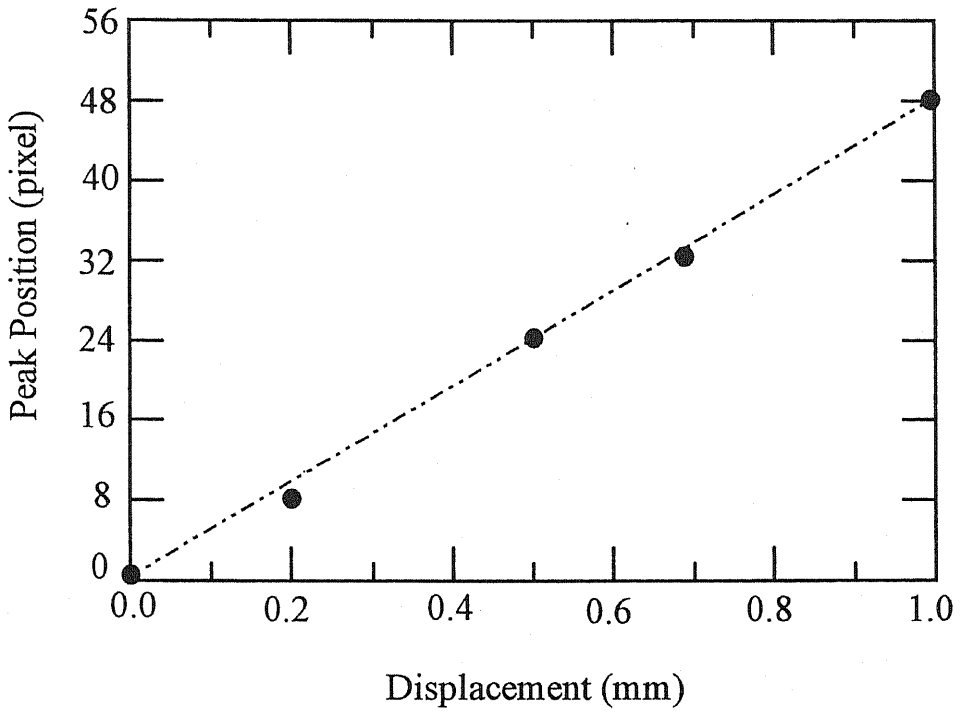

Fig. 3.9 Relation between the displacement and peak position of the correlation function.

In the experiment, we have used a ground glass plate which is a rather well-defined diffuser and has little depolarization effect. When we use an actual diffuser such as a rough metal surface or an opal glass plate, the depolarization effect by such a light scattering object plays an important role for the formation of the speckle pattern. But, in this case, we can select a certain polarized state of the speckle pattern though a polarizer. Actually, the polarization filter is inserted in front of the spatial shifter in the experiment as shown in Fig. 3.3. We have also tried to measure the displacement for a light scattering object having a depolarization effect and verified that this method can be applied to such an object. As for the deformation of speckles, the effect of the speckle decorrelation may not be assumed negligible for a large surface deformation, although speckles deform little for a pure translation state of a light scattering object. But, the deformation under usual interests in speckle applications is small, so that one can expect a similar speckle pattern even after the deformation of the object and the proposed method can be still applied.

However, the switching speed of the TN-LC cell used in the experiment is rather slow

and is about 100 ms. Therefore, this TN-LC cell is suited for the displacement measurement or the velocity measurement of a slowly moving object. For a velocity measurement in most cases, a faster polarization switching device may be required to realize a real-time JTC based on the proposed method. Currently, a FLC device which has a switching speed of the order of micro-second to several tens of micro-second is available as the polarization switch. This value of the switching speed is satisfactory for most mechanical application in speckle metrology. In this case, a SLM having a faster switching speed compatible with the speed of the FLC polarization switching device is also required to implement a real-time optical correlator. Fortunately, a FLC-SLM which has the same switching speed as the FLC polarization switching device is now available. Besides, as already mentioned in section 2.2, a FLC-SLM also has the attractive feature of double and multiple exposure capability of images, so that a joint pattern can be easily formed in real-time. We have presented an experiment using such devices and it is described in the following section.

3.3 REAL-TIME OPTICAL JTC FOR SPECKLE MEASUREMENTS USING FLC-SLM

We have described an optical implementation to obtain a joint pattern by using a spatial shifting unit which consists of a polarization switch of a 90° TN-LC cell and a birefringent plate in section 3.2.[3.21] By the introduction of the spatial shift for the input pattern, we could obtain not only an object displacement but also its direction in the speckle measurements. In that experiment, we successfully composed a joint pattern and digitally calculated a joint transform correlation from the optically composed joint pattern. But the switching speed of the TN-LC device used in that experiment is rather slow and is about 100 ms, so that it is useful only for the measurements of rather slowly moving object or static displacement and its speed was not sufficient for dynamic speckle measurements.

In this section, we employed a FLC cell as a polarization switching device instead of a

TN-LC cell because of the capabilities of the faster switching operation. The FLC polarization switching device used in the experiment can operate as fast as 100 μs and behave as a half wave plate. For the optical realization of the JTC, we also employed an optically addressed FLC-SLM which can operate as fast as the switching speed of the FLC polarization switch. Optically addressed FLC-SLM has been used in performing optical correlation, real-time holography, optical phase conjugation, real-time incoherent to coherent light conversion, neural computation, and other various optical information processings.[3.22-24] Here, the important feature of the FLC-SLM is the capability of multiple exposures for input patterns. The FLC-SLM has a memory effect so that it is possible to overwrite multiple images. A real-time optical JTC for speckle applications is proposed based on these characteristics of FLC polarization switching device and FLC-SLM. By using the combination of a FLC polarization switch and a birefringent plate, an appropriate spatial shift can be quickly given to the successive two patterns. The speckle patterns before and after the deformation or the movement of an object are taken as a doubly exposed joint pattern onto the FLC-SLM synchronizing with the operation of a FLC polarization switch. The joint pattern is optically processed and the JTC pattern is finally obtained. The cycle time of the FLC devices used in the experiment is as fast as several ms. We performed the object velocity measurement and the object speed up to 100 mm/s can be measured at modest operation of the FLC devices.

3.3.1 Principle of Spatial Shift

The main elements of the module to produce a spatial shifted joint pattern are a FLC polarization switch and a birefringent calcite ($CaCO_3$) plate. By using this module, an appropriate spatial offset between successive two speckle patterns can be quickly given. The principle of the method for the spatial shift by using a FLC device is almost the same as that by using a TN-LC device. But the operation of a FLC device is a little bit different from that of a TN-LC device. Consider the situation where a p-polarized pattern passes through a FLC

polarization switch as shown in Fig. 3.10.

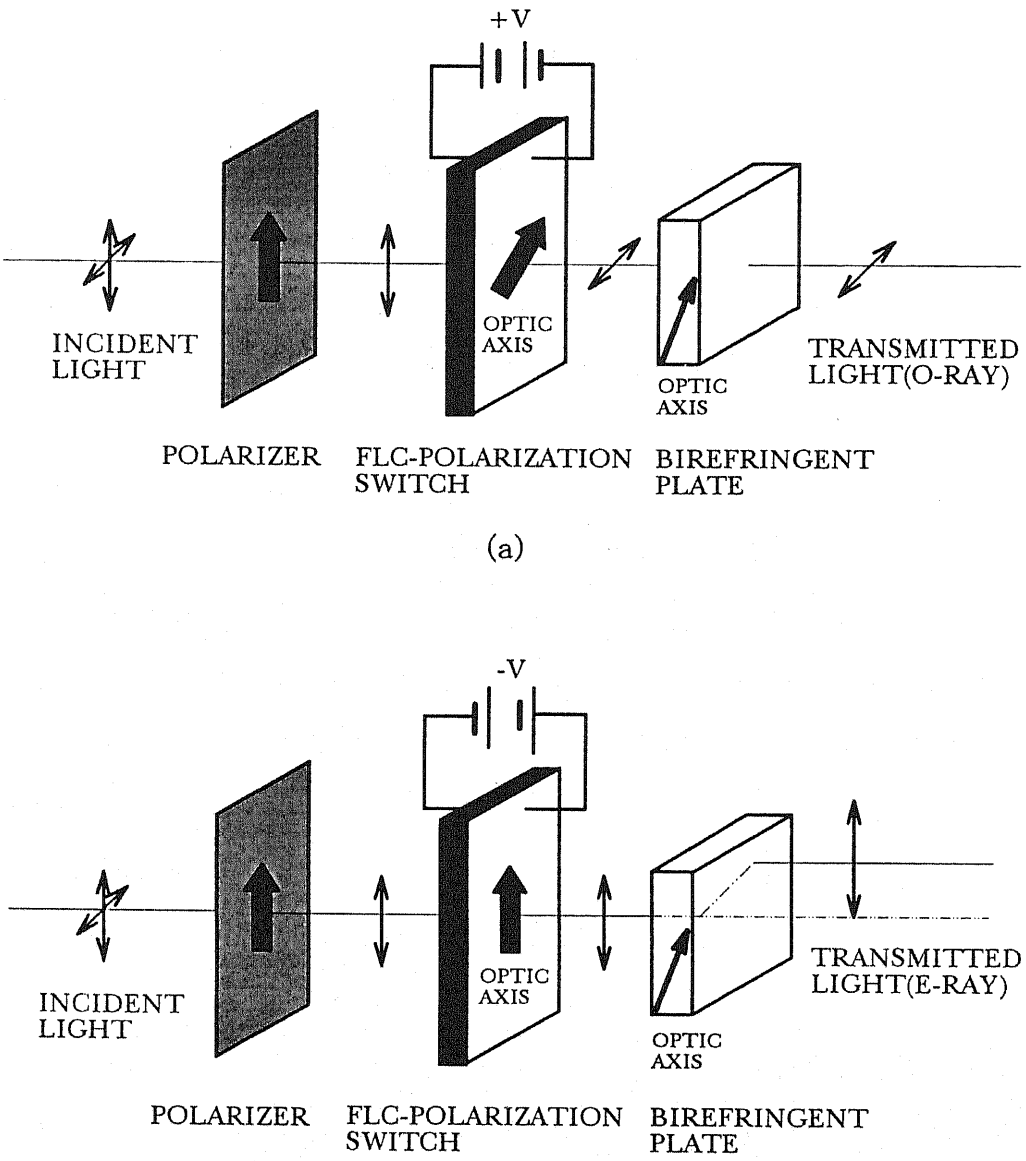

Fig. 3.10 Principle operation of the spatial shift for an input pattern.

As already mentioned in Section 2.2, when the molecules of chiral semectic-C* liquid crystal form a thin layered structure, the electric polarizations of the molecules have two

preferred orientations and the orientation can be selected by an externally applied electric field. The liquid crystal material is nominally a uniaxial birefringent medium with its optic axis parallel to the average orientation of the liquid crystal molecules. By properly setting the thickness of the FLC layer and the liquid crystal orientations, the polarization of the input light at an appropriate wavelength is changed by 90°. Namely, the FLC cell functions as a half wave plate. For example, when the applied voltage to the FLC switch is positive, the p-polarization of the pattern rotates 90° for an appropriate orientation of the liquid crystal molecules and becomes a s-polarized pattern as shown in Fig. 3.10 (a). On the other hand, it remains unchanged when the applied voltage is negative as shown in Fig. 3.10 (b). The switching speed of the polarization is in general faster than 100 μs for a FLC device, while it is ~100 ms for a TN-LC device.

To give a spatial shift to the second pattern with respect to the first one, a birefringent plate is inserted behind the FLC polarization switch. If the optic axis of the birefringent crystal is lying at the same plane as the p-polarization as shown in Fig. 3.10 (a), the transmitted light through the birefringent plate becomes an ordinary ray and no spatial shift of the pattern occurs. On the other hand, the p-polarized light becomes an extraordinary ray after passing through the birefringent plate as shown in Fig. 3.10 (b). Thus, a certain amount of the spatial shift is given to the second pattern by selecting the applied voltage with appropriate time sequence to the FLC polarization switch. The amount of the shift depends on the length of the crystal along the light transmission and the wavelength used. By inserting this spatial shift module in front of an FLC-SLM, the joint pattern can be taken by the FLC-SLM which plays an important role as a double exposure device.

3.3.2 Experiments

The whole system of the real-time optical speckle JTC is shown in Fig. 3.11. A rotating ground glass plate mounted on a two-dimensional X-Y stage by which we can select the position of

the illumination on the glass plate is illuminated by a direct beam from a 50 mW He-Ne laser LASER 1 operating at the wavelength of 633 nm. A speckle pattern is generated by the rotating ground glass plate. The speckle pattern is imaged by a single lens L1 (f=100 mm) together with an aperture (12 mm) which controls the size of the image speckle. The magnification of the lens L1 in the speckle imaging was 7.5. The average speckle diameter D_s can be estimated by the parameters of the imaging system and is given by

$$D_s = 1.22\lambda(1+M)F, \tag{3.4}$$

where λ is the wavelength, M is the image magnification, and F is the F-number of the imaging lens. Thus, the speckle size becomes about 50 μm on the FLC-SLM.

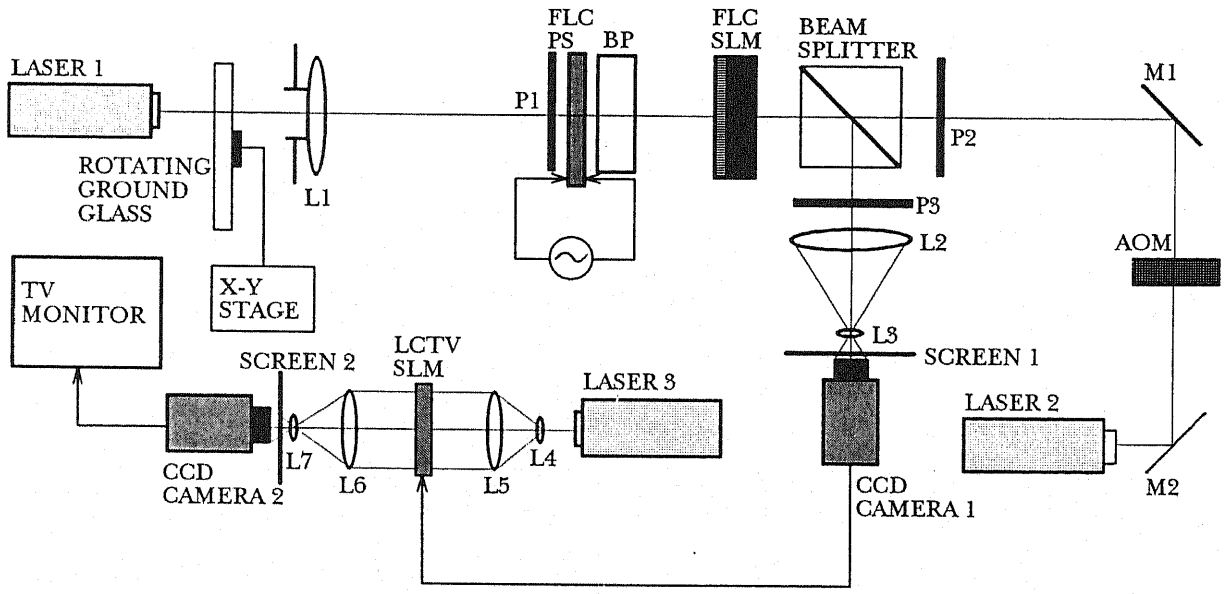

Fig. 3.11 Schematic diagram of speckle detection and the optical JTC. FLC PS: FLC polarization switch, BP: birefringent plate, AOM: acousto-optic modulator, and P1-P3: polarizers.

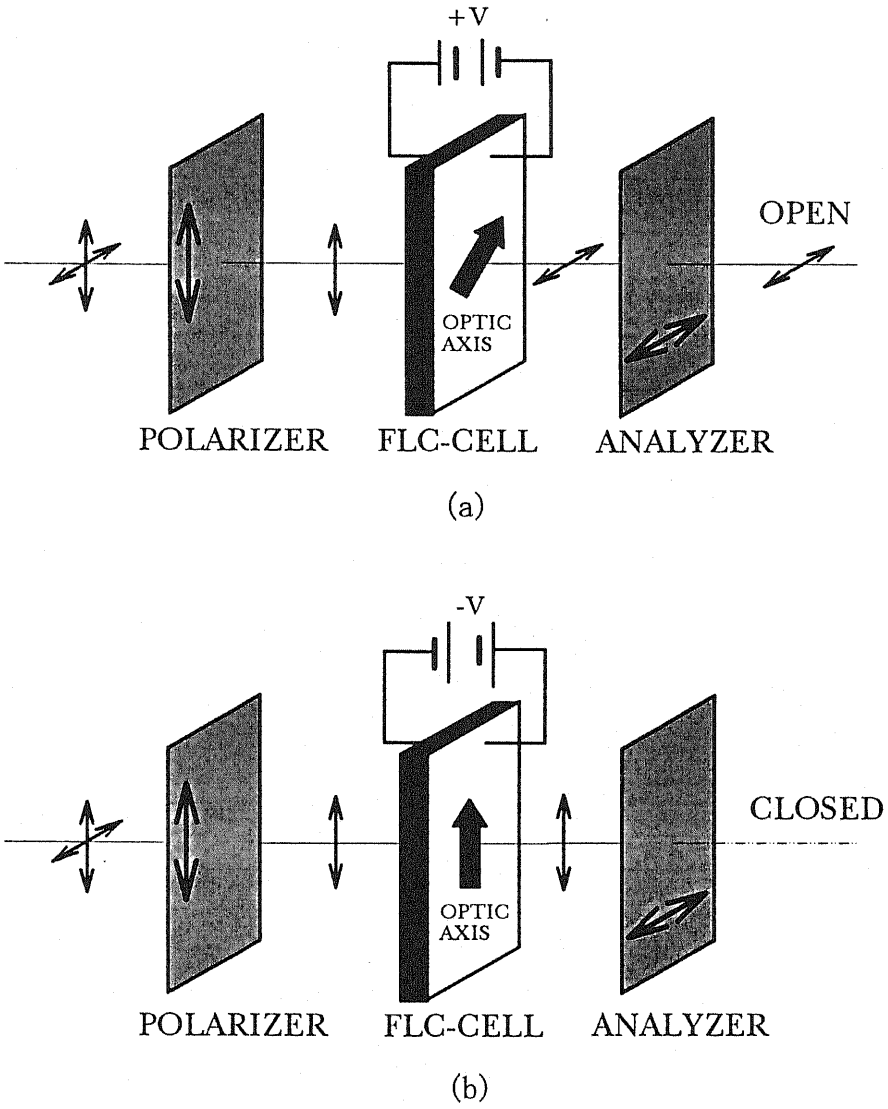

Fig. 3.12 Principle operation of the FLC light valve.

The FLC polarization switch used in the experiment is a commercially available intensity switching device (Displaytech LV050AC FLC Light Valve) driven by an electrical signal. Originally, this FLC Light Valve is intended for use as a high speed, broadband optical shutter, chopper or modulator. The device consists of a thin cell of FLC material between crossed polarizers as shown in Fig. 3.12. Incoming light passes through the first linear polarizer and then through the FLC cell. Transparent electrodes on either side of the cell allow a drive

voltage to be applied to the cell. When the voltage is +V, the polarization plane of the light is changed by 90°. The light then passes through the second polarizer. This is the open or transmitting state. When the voltage is -V, the linearly polarized light passes through the cell unchanged. The light is then blocked by the second polarizer. This is the closed or non-transmitting state. Thus, the device transmits light when the voltage is +V but does not transmit light when the voltage is -V.

The FLC cell functions as a voltage switchable half wave plate. It can be optimized for a chosen wavelength of light. Since the cell is a very thin first order wave plate, wavelengths on either side of the design wavelength are changed by very nearly 90°. Hence the device has usable performance over a broad range of wavelengths.

In our experiments, the polarizer and the analyzer were removed to use it as a polarization switch. The speckle pattern is detected by an optically addressed FLC-SLM through a spatial shifter unit which is discussed in the previous section. By using this spatial shifter, a spatial offset between the successive two speckle patterns is given. The amount of the spatial offset depends on the length of the birefringent calcite crystal along the light transmission. The FLC polarization switch has a circular aperture and the diameter of its clear aperture is 12 mm. The clear aperture of the birefringent plate is 20×20 mm^2 and the thickness of the crystal is 4.59 mm which corresponds to a spatial shift of the extraordinary ray of 0.5 mm at the wavelength of 633 nm. The molecules of the FLC polarization switch have two preferred orientations, separated from each other by 45°, so that, for a polarized light at an appropriate polarization angle of incidence, one can change the polarization 90° by switching the applied voltage. The raise time of the FLC polarization switch is 50 μs.

The clear aperture of the FLC-SLM is 20×20 mm^2 [3.25] and the average power on the FLC-SLM used in the experiments was roughly estimated to be several hundreds $\mu W/cm^2$. Then, the patterns before and after the displacement of the object motion are written onto the FLC-SLM and the joint pattern is formed as a doubly exposed speckle pattern. The FLC device has bistable characteristics and the effect can be used as a memory. The optical axis of

the FLC molecules is switched between two stable orientations. Therefore, the FLC-SLM behaves as a binary threshold device for the input light. Thus, the FLC device can be used not only as a polarization switch but also a SLM. The general operation characteristics and structures of FLC-SLMs have been described in Section 2.2. The operation of the FLC-SLM is synchronized with the polarization switch. There are two possible drives of the FLC-SLM to write a doubly exposed pattern: one is optical and the other is electrical (see Section 2.2). We employed the electrical writing mode for easiness of the experiment, though the optical writing mode has better visibilities because of little blurred effect of the patterns taken by the FLC-SLM.

Figure 3.13 shows an example of the time chart of the driving voltage signals for the FLC-SLM and the FLC polarization switch for the double exposures. Both the FLC-SLM and the FLC polarization switch were driven by zero mean AC voltages to avoid unwanted phase changes of the molecules. In Fig. 3.13 (a), an erase pulse must be applied to the FLC-SLM to eliminate the device history since it has a bistable characteristics. The duration of the erase pulse was typically 2 ms. The write patterns are recorded during the write intervals by positive write-in pulses. Finally, when the read-in beam is incident from the back side of the FLC-SLM only during the read interval, the stored image is read out. In Fig. 3.13 (b), the FLC polarization switch is not driven by a squared wave signal but a specific optimized waveform to facilitate fast switching of the FLC material and promote long lifetime of the device. Then the waveform exhibits a ±15 V switching transient which is 300~600 μs decays to a ±5 V switching voltage as illustrated in Fig. 3.13 (b).

The polarization of the pattern passing through the FLC polarization switch is changed between the successive exposures. The time interval of the successive pulses was typically about several hundreds μs to 1 ms. Between the successive pulses, the speckle pattern moves certain amount across the FLC-SLM plane, while the patterns are assumed to be stationary within the write-in pulse durations. The width of each pulse was typically one hundred micro-seconds depending on the input light intensity of the pattern. The polarization

of speckle pattern is switched by the FLC polarization switch synchronized with the operation of the FLC-SLM. It is possible to set a shorter time separation for the double exposures depending on the writing light intensity.

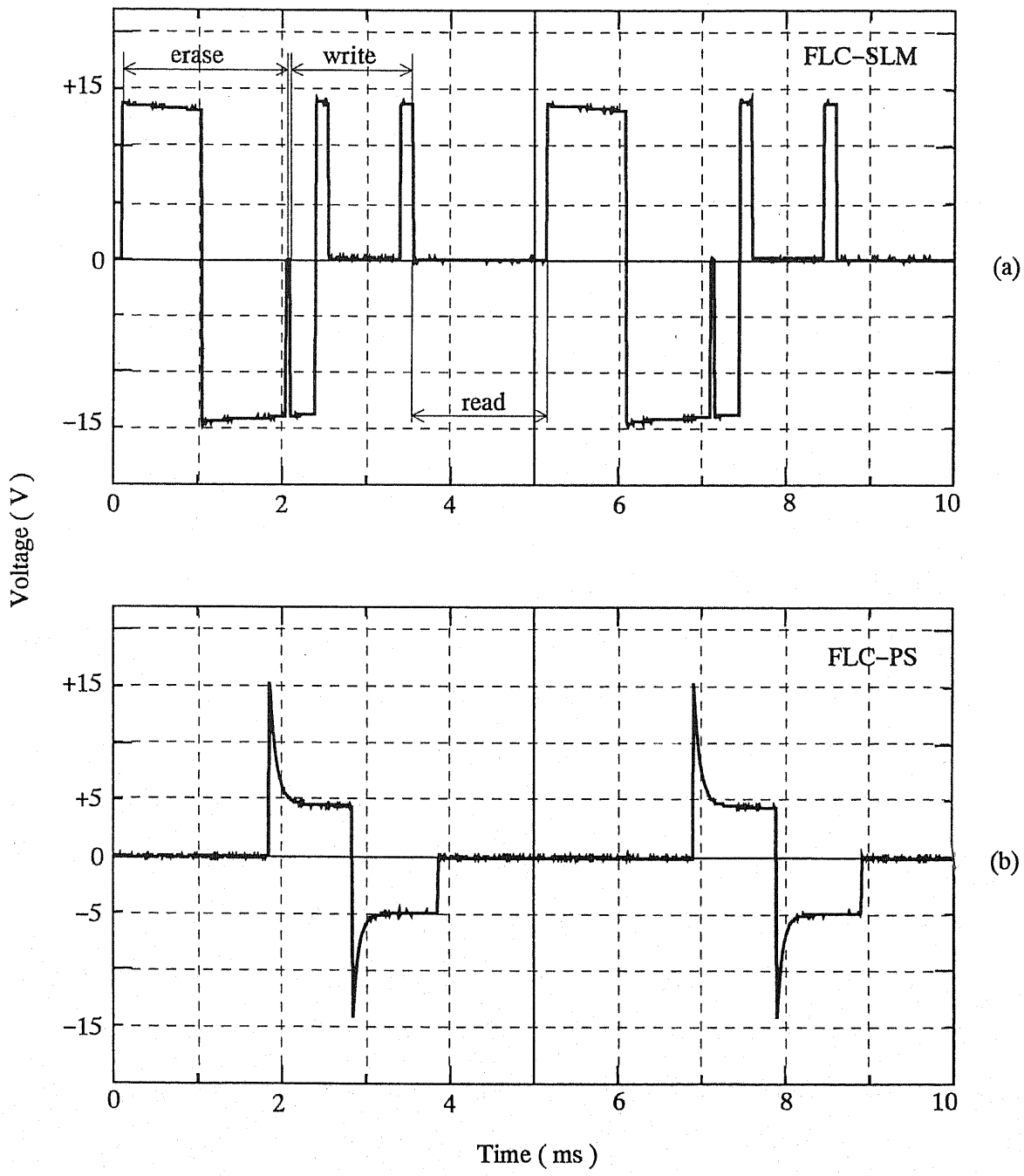

Fig. 3.13 Electrical signal for the FLC-SLM (a) and the FLC polarization switch (b).

The joint pattern taken by the FLC-SLM was read by a He-Ne laser LASER 2 in Fig. 3.11 and the read coherent pattern was optically Fourier transformed by a lens L2 (f=200 mm). The read beam from LASER 2 is turned on by an acousto-optic modulator only at the reading operation to avoid unnecessary exposures to the FLC-SLM. The Fourier transformed pattern was enlarged by an objective lens L3 (×10). The Fourier transformed pattern was imaged onto the screen SCREEN 1 and taken by a CCD camera CAMERA 1. Then, it was displayed onto an LCTV-SLM. The Fourier transformed pattern, i.e., the fringe pattern, was again optically Fourier transformed by a lens L6 (f=100 mm). Then, we obtain a joint transformed pattern on a CCD camera CAMERA 2 through a magnification lens L7 (×10). The whole system was controlled by a micro-computer and the CCD cameras were also synchronized with the operation of the FLC switch and the FLC-SLM. Thus, the object velocity can be measured at time resolution less than or around 1 ms, but the sampling rate is limited by a TV frame rate of 1/30 s in the experiment.

3.3.3 Results and Discussion

By using the system described in the previous subsection, we conducted an in-plane velocity measurement of the rotating ground glass plate. Figure 3.14 shows the Fourier transformed pattern of a joint speckle pattern and its Fourier transformed pattern, i.e., the joint correlation, taken by the CCD cameras for a stationary object. The spatial offset was given to the horizontal direction in the figure so that several vertical fringes can be seen at the Fourier plane of the joint pattern as shown in Fig. 3.14 (a). The time interval between the two write-in pulses to the FLC-SLM was set to be 850 μs and the duration of the write-in pulses was set to be 150 μs in the experiment. Fig. 3.14 (b) is the optical Fourier transformed pattern of the fringes of Fig. 3.14 (a). Both the DC components of the fringe pattern and the correlation pattern were suppressed by the masks on the screens to obtain appropriate signal levels on the CCD cameras. The distance between the correlation peaks in Fig. 3.14 (b) correspond to the spatial

ffset. The position of the either correlation peak in Fig. 3.14 (b) becomes a new origin for the peckle velocity measurement.

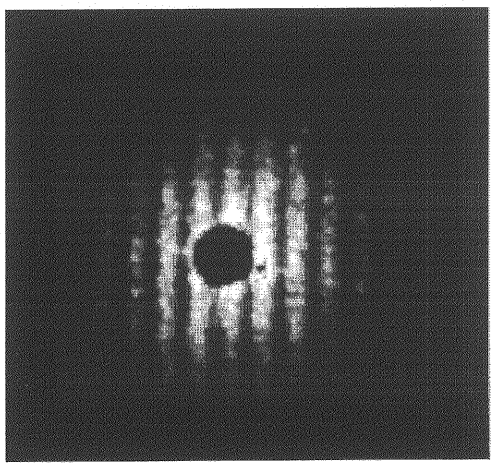

(a)

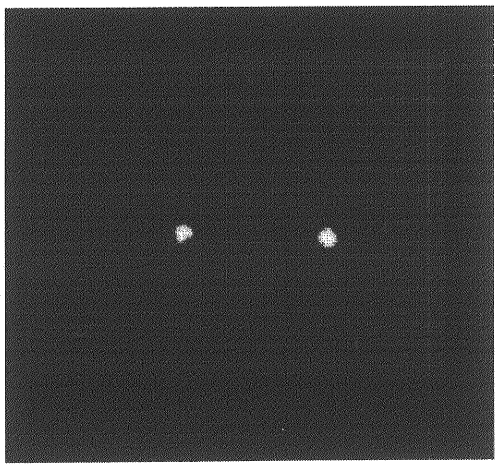

(b)

ig. 3.14 (a) Fringe pattern obtained by the Fourier transform of a joint pattern for the tationary object. (b) Optically calculated joint transform pattern.

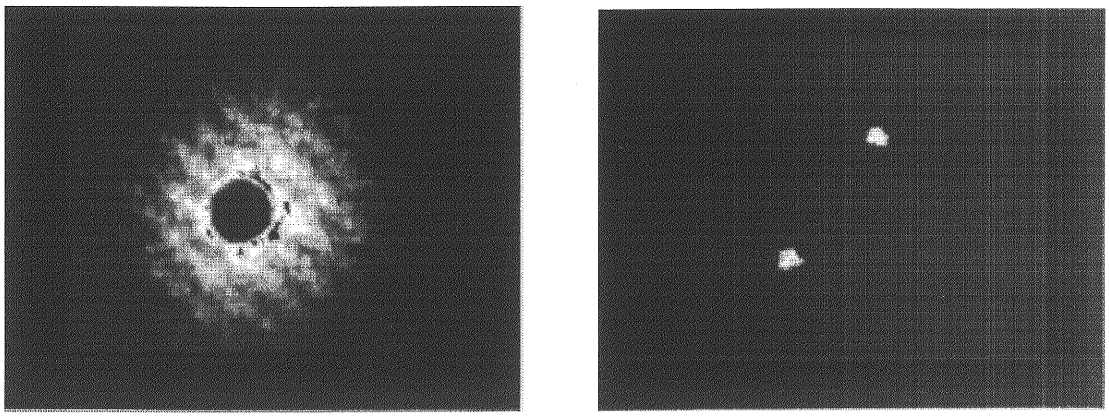

(a) (b)

ig. 3.15 (a) Fringe pattern when the ground glass plate rotates clockwise direction. (b) Joint ransform pattern.

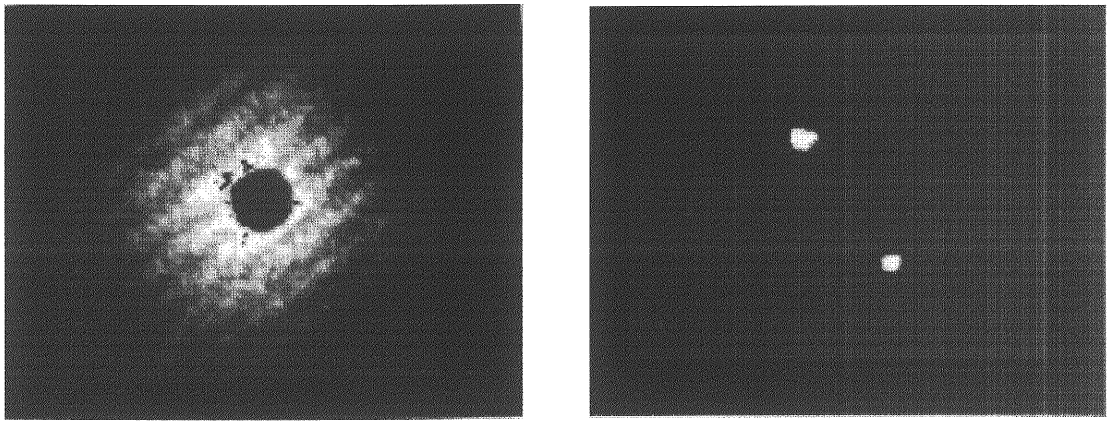

(a) (b)

ig. 3.16 (a) Fringe pattern when the ground glass plate rotates counter-clockwise direction inverse direction of Fig. 3.15). (b) Joint transform pattern.

Figure 3.15 shows examples of the fringe patterns and the JTCs for the object in motion. The fringes in Fig. 3.15 (a) do not align for the vertical direction any more due to the rotation of the ground glass plate. From the corresponding peaks of the joint transformed pattern in Fig. 3.15 (b), we can obtain the magnitude and direction of the motion of the rotating ground glass plate at the illumination spot. The distance between the correlation peaks in Figs. 3.14 (b) and 3.15 (b) represents the magnitude of the motion and its direction from the origin represents the direction of the motion. The detection principle of the magnitude and the direction has been discussed in detail in Ref. 3.14. Figure 3.16 shows another examples of the results. In this figure, the location of the illuminating spot on the ground glass plate is the same as in Fig. 3.15, while the direction of the rotation is opposite to that of Fig. 3.15. It is easily seen that the correlation spots in Figs. 3.15 and 3.16 are symmetrically situated. The magnitude and the direction of the motion are also calculated from the distance and direction between the origin and the correlation peak.

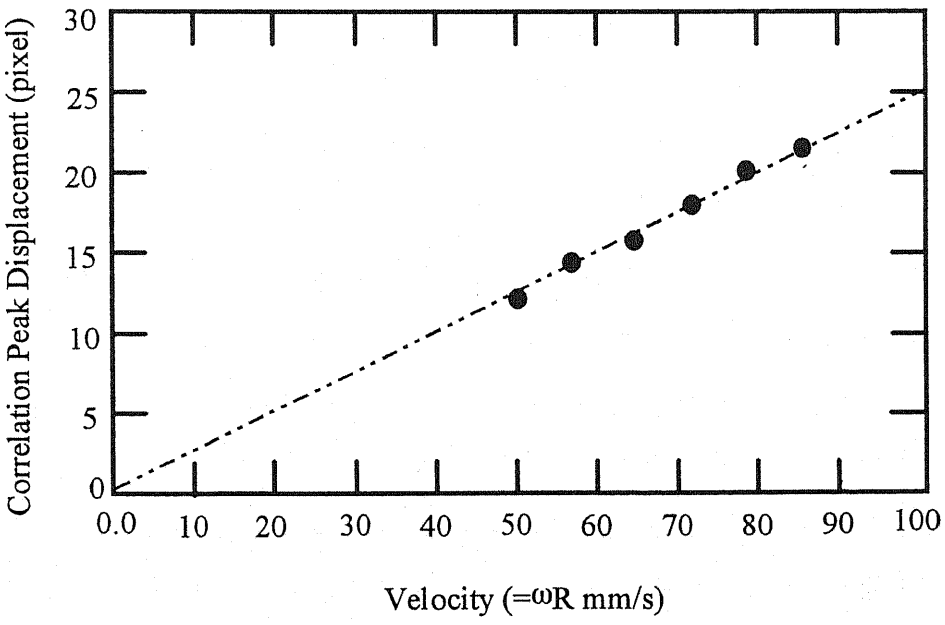

Fig. 3.17 Relation between the object velocity and the correlation peak displacement.

Figure 3.17 shows the result of the velocity measurement. Though we can measure not only the magnitude of the object motion but also its direction, we only displayed the relation between the magnitude of the velocity and the correlation peak displacement. We could obtain a good linear relation between the peak displacement and the object velocity so that the system can be used for speckle velocity measurements. By using a TN-LC device as a polarization switching device, we could only measure static displacement of an object as shown in Section 3.2. On the other hand, by using a FLC polarization switching device and a FLC-SLM, the measurement of an object motion up to 100 mm/s can be performed at a modest operation of the FLC devices as shown in Fig. 3.17. The limitation of the speed in the current experiments is originated from the separation of the speckle pairs on the FLC-SLM (i.e., 0.5 mm) and the time interval between the successive exposures (i.e., several hundreds μs). A faster object velocity measurement is possible by using a high power laser. The speckle size we used in the experiment was about 50 μm. The maximum resolution of FLC-SLM is said to be 200 /p/mm, so that finer speckle pattern can be stored in an FLC-SLM. From this point of view, it is at present possible to achieve faster object velocity measurement by employing a thinner birefringent calcite plate and smaller magnification of the speckles even for the same operation condition of the FLC devices. Thus, by using FLC devices, dynamical speckle measurement can be done in two-dimensional space. The device with such a high speed switching capability is especially very suitable for dynamical mechanical measurements.

3.4 SUMMARY

We have described a method for the generation of a joint pattern to calculate a joint transform correlation function for speckle applications in Section 3.2. To give a spatial shift to the pattern, the combination of a 90° TN-LC cell and a birefringent calcite plate has been used based on the polarization switching by the TN-LC cell and the optical path separation between the o- and e-rays through the birefringent plate. The successive two speckle patterns before

and after the displacement have been detected. A spatial shift has been given to the latter pattern, so that the joint pattern which is something like a specklegram but is different from an ordinary one has been formed from the two patterns. Then, the joint transform correlation function has been calculated. A good linear relation between the peak position of the correlation function and the object displacement has been obtained, which enables the application of this method to displacement and velocity measurements in speckle techniques.

In Section 3.3, we have successfully realized a real-time high-speed joint transform correlator for speckle applications by using FLC devices which can operate faster than a cycle of several ms. To make a spatial shift for a pattern, the combination of a FLC polarization switch and a birefringent plate has been used. The joint pattern before and after the motion has been written onto a FLC-SLM as a double-exposure image synchronized with FLC polarization switch. The joint pattern has been optically processed and the JTC pattern has been obtained. An object speed as fast as 100 mm/s can be measured by the currently proposed system at its modest operation. The switching speed of the FLC devices and the order of the speed obtained in the experiments are satisfactory for ordinary mechanical applications in speckle metrology.

At the second stage of the optical Fourier transform, we have used a CCD camera and a LCTV-SLM to obtain a final joint transform pattern. Therefore, the velocity can be measured at a time resolution as fast as 1 ms, but the sampling rate is limited by a TV frame rate of 1/30 s. If an another FLC-SLM is available for the second optical Fourier transform in the system, a faster sampling rate can be achieved by synchronizing the second FLC-SLM with the first FLC-SLM and the FLC polarization switch. Though FLC-SLM is a very attractive and promising device for real-time optical processing and computing, the sensitivity of the device to an input light, which is actually limited by the sensitivity of a transparent conduction electrodes, is not so high and a rather high power laser must be used especially for writing a pattern. So this point should be improved to realize a compact joint transform correlator by using a compact and small power laser systems.

REFERENCES

3.1 J. C. Dainty, ed., *Laser speckle and related phenomena* Ch. 6 (Springer, Berlin, 1984).

3.2 T. D. Dudderar, R. Meynart, and P. G. Simpkins, *Opt. and Lasers in Eng.* **9,** 163 (1988).

3.3 A. B. VanderLugt, *IEEE Trans. Inf. Theory* **IT-10**, 139 (1964).

3.4 C. S. Weaver and J. W. Goodman, *Appl. Opt.* **5**, 1248 (1966).

3.5 J. C. Kirsch and D. A. Gregory, *Opt. Eng.* **29**, 1122 (1990).

3.6 M. C. Hamilton, and B. L. Powers, *Opt. Lett.* **12**, 549 (1987).

3.7 B. Javidi, and C. J. Kuo, *Appl. Opt.* **27**, 663 (1988).

3.8 B. Javidi, and S. F. Odeh, *Opt. Eng.* **27**, 295 (1988).

3.9 J. M. Florence, *Opt. Lett.* **14**, 341 (1989).

3.10 F. T. S. Yu, and X. J. Lu, *Opt. Commun.* **52,** 10 (1984).

3.11 F. T. S. Yu, S. Jutamulia, T. W. Lin, and D. A. Gregory, *Appl. Opt.* **26,** 1370 (1987).

3.12 Q. Tang, and B. Javidi, *Appl. Opt.* **31,** 4016 (1992).

3.13 A. Ogiwara, H. Sakai, and J. Ohtsubo, *Opt. Commun.* **78,** 213 (1990).

3.14 A. Ogiwara, H. Sakai, and J. Ohtsubo, *Opt. Commun.* **78,** 322 (1990).

3.15 A. Ogiwara, H. Sakai, and J. Ohtsubo, *Opt. Commun.* **86,** 513 (1991).

3.16 A. Ogiwara, and J. Ohtsubo, *Opt. Commun.* **93,** 234 (1992).

3.17 J. Ohtsubo, *J. Opt.* **12,** 129 (1981).

3.18 J. Ohtsubo, *Appl. Opt.* **24,** 746 (1985).

3.19 J. Marron, and G. M. Morris, *Appl. Opt.* **25,** 789 (1986).

3.20 J. Ohtsubo, and A. Ogiwara, *Opt. Commun.* **65,** 73 (1988).

3.21 X. Lin, J. Ohtsubo, and T. Takemori, *Opt. Commun.* **98,** 41 (1993).

3.22 D. A. Jared, K. M. Johnson, and G. Moddel, *Opt. Commun.* **76,** 97 (1990).

3.23 C. C. Mao, K. M. Johnson, R. Turner, D. A. Jared, and D. Doroski, *Appl. Opt.* **31,** 3908 (1992).

3.24 M. Killinger, J. L. de Bougrenet de la Tocnaye, P. Cambon, R. C. Chittick, and

W. A. Crossland, *Appl. Opt.* **31,** 3930 (1992).

3.25 Y. Kobayashi, T. Takemori, N. Mukohzaka, N. Yoshida, and S. Fukushima, *Appl. Opt.* **33,** 2785 (1994).

Real-time optical image subtraction and edge enhancement based on a speckle modulation technique are carried out by using FLC polarization switches and a FLC-SLM. A FLC-SLM is employed as a real-time and multiple exposure optical device and the successful results are obtained from three exposure images modulated by speckles. Thus, the image subtraction and edge enhancement are realized in real-time. The whole operation is performed within several ms with a modest condition of the operation. As the used FLC-SLM has a high resolution more than 100 lp/mm and can store fine speckle patterns, the image qualities for the obtained results are quite satisfactory.

CHAPTER 4

REAL-TIME OPTICAL IMAGE PROCESSING USING FLC DEVICES BASED ON SPECKLE MODULATION

Laser speckle technique is used not only in optical measurements but also in various fields of optical information and image processing such as to extract the difference between two images, image coding and decoding, and image multiplexing. Speckle pattern can carry the information of images by its random nature of the coding. Optical image subtraction and other optical information processing based on the speckle modulation technique have been proposed since early 1970s.[4.1-3] The speckle modulation technique has also been applied to speckle metrology. In usual, an image to be processed has a rather low frequency signal component and has a small diffraction area in the Fourier plane. But, by the introduction of speckle modulation, its information is enforced to be spread out in the high frequency region. Thus, the technique makes it easier to filter the Fourier spectrum and process the input image. But the proposed methods were almost based on the photographic technique by which the real-time processing is not possible. As an alternative method, a video system is used for the processing, however, the resolution of the imaging device and the total number of the pixels are currently not sufficient to obtain good results and it is also limited by the video frame rate.

As already mentioned, optically addressed SLMs are easily available and they are expected to be rewritable real-time devices in optical information processing and optical computing. One of the promising devices is a FLC-SLM which is used in various fields of optical information processing such as real-time speckle metrology,[4.4-5] real-time optical correlation,[4.6] optical phase conjugation,[4.7] real-time holography,[4.8-9] and opto-electronic neural networks.[4.10] The FLC-SLM has attractive features of high sensitivity, high gain, fast response, multiple-exposure capability, and high resolution as a real-time optical spatial light modulator.

In this section, we propose a novel techniques of real-time image subtraction and edge enhancement by using a FLC-SLM and FLC polarization switches based on the speckle modulation. In the proposed system, we employed a FLC-SLM as a real-time multiple-exposure device instead of a photographic plate. We also used FLC polarization switches together with birefringent plates to generate appropriate spatial offsets to realize the image

subtraction for the successive exposures. By using the same optical system as that for the image subtraction, the edge enhancement of an image is performed by using the successive exposures with focused and defocused imaging systems. The exposed pattern on the FLC-SLM is optically Fourier transformed and filtered by a slit filter at the Fourier plane. Finally, the edge enhancement image is obtained by the optical Fourier transform of the filtered patterns. The FLC-SLM can be switched as fast as μs, so that it is possible to perform image subtraction and edge enhancement within several to ten μs at its fastest operation rate. Therefore, the potential operation speed is expected to be much faster than that of the conventional system. The actual switching speed of the FLC-SLM is dependent on the incoming light level. The other merit of the use of FLC-SLM with speckle modulation technique is that FLC-SLM can store high frequency information due to its high resolution image capture capability.

4.1 THEORY OF SPECKLE MODULATION

4.1.1 General Principle

A laser speckle pattern contains high spatial frequencies and is able to carry the information of images by a random coding. It gives a wide spread-out field in the spectrum plane of the signal, and this facilitates the operations of filtering. The method of the subtraction between images by speckle modulation has already been studied by using a photographic film or video devices.[4.2] Figure 4.1 (a) shows the recording geometry in the conventional method of the speckle modulation. Let A be a signal to be processed. Generally, it is a transparency with $a(x,y)$ as its light distribution. A high resolution photographic plate H, placed immediately behind A records the product $a(x,y)\cdot g(x,y)$, where $g(x,y)$ is the speckle pattern produced by the ground glass G. The distance between A and H is so small that they can be considered to lie in the same plane. The photographic plate is exposed twice to the speckle pattern and between

the exposures it is translated through y_0. The total light recorded is

$$a(x,y)\cdot g(x,y)+a(x,y-y_0)\cdot g(x,y-y_0).$$

This expression can be rewritten as

$$[a(x,y)\cdot g(x,y)]*[\delta(x,y)+\delta(x,y-y_0)],$$

where the symbol $*$ denotes a convolution operator and the function $\delta(\cdot)$ is the delta-function.

The photographic plate is processed under the usual conditions of linearity and it is illuminated by a parallel beam of light, as shown in Fig. 4.1 (b). The amplitude transmitted is given by

$$t(x,y)=\alpha-\beta\{[a(x,y)\cdot g(x,y)]*[\delta(x,y)+\delta(x,y-y_0)]\}, \tag{4.1}$$

where α and β are constants representing the transmittance of the unexposed film and the slope of the amplitude transmittance versus energy of exposure, respectively. The amplitude distribution in the focal plane of lens L1 is the Fourier transform of $t(x,y)$, that is

$$T(u,v)=\alpha\cdot\delta(u,v)-\beta\left\{[A(u,v)*G(u,v)]\cdot\left[1+\exp\left(-j\frac{2\pi v}{\lambda}y_0\right)\right]\right\}, \tag{4.2}$$

where (u,v) is a Fourier angular coordinate of a point in the focal plane of lens L1. The upper letter functions are the Fourier transforms of the corresponding lower letter functions, and λ is the wavelength of light. The first term on the right-hand side of Eq. (4.2) represents the direct image of the source which is located in F at the focus of L1. It can be neglected due to its small size. In the second term, apart a constant, the spectrum of the product

$a(x,y)\cdot g(x,y)$ is modulated by the factor $1+\exp(-j2\pi\nu y_0/\lambda)$ which represents a system of Young's fringes the light of which is proportional to $\cos^2(\pi\nu y_0/\lambda)$.

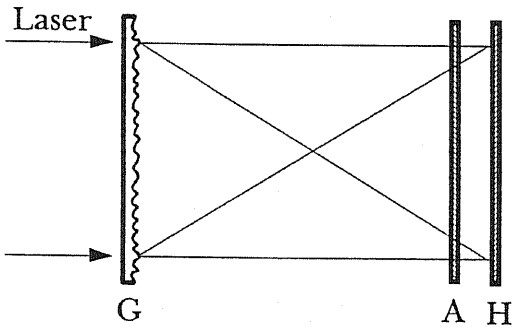

(a)

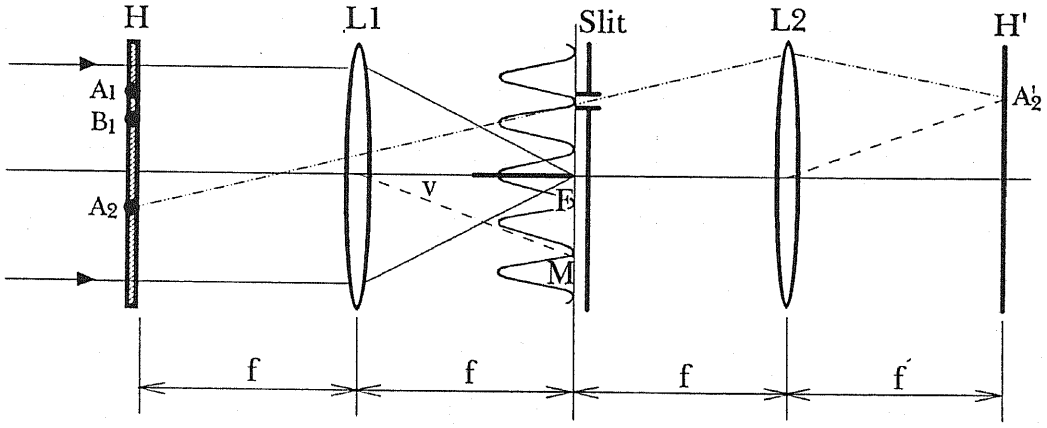

(b)

Fig. 4.1 Optical images processing by speckle modulation. (a) Recording of the transparency A modulated by the speckle pattern and (b) optical filtering system. G: ground glass, A: transparency, and H: photographic plate.

Consider a slit placed in the focal plane of L1 and so positioned that the slit coincides with a maximum fringe; such a slit allows the signal to give its image in the plane H' conjugate

to H. If the slit is translated in its plane through half a period so that it falls on a minimum fringe, no information from the signal will be transmitted. The slit acts as a filter for the extraction of the required information. The reconstructed image $a(x,y)\cdot g(x,y)$ in the plane H' is modulated by a speckle pattern $g(x,y)$, but due to fine structure of the speckle such modulation is not visible.

4.1.2 Detection of the Difference Between Two Images

Let A and B be the two signal to be compared, and A and B are copied on the same high resolution photographic plate H, as shown in Fig. 4.1 (a). During the first exposure, A is placed against H and is illuminated by means of a speckle pattern from the ground glass G. A is then replaced by B, but before the second exposure, H is given a small translation in any direction. Figure 4.2 represents an area of H after the development. In areas where A and B are identical, for each speckle grain recorded with A, there corresponds an identical speckle grain recorded with B. The distance between two identical grains is equal to the translation given to the plate H between the two exposures. On the other hand, in areas where A and B are different, the intensities of the corresponding points are different. If in a certain area A is completely transparent and B is opaque, only the speckle grains recorded with A will be present. Let H be illuminated with a collimated beam as shown in Fig. 4.1 (b), then , the lenses L1 and L2 form an image of H at H'. In areas where A and B are identical, there are groups of two identical grains. These grains diffract light, and two identical grains such as A_1 and B_1 yield Young's fringes in the focal plane of lens L1. This is true of all the areas of A and B that are identical. If an opaque screen with a slit is placed in the focal plane in such a way that the slit coincides with a dark fringe, the light from A_1 and B_1 will not reach the image H'. This is true for every group of two identical grains, and therefore the light from all the identical areas of A and B will disappear from the image H'. Consider areas where A and B are different. The two corresponding grains are different and do not diffract the same luminous intensities. They

yield Young's fringes with non-zero minima. Some of the light goes through and reaches H'. Only areas of A and B which are different are seen in H' and, thus, the difference A-B is observed.

Although the photographic plate has superior resolution and sensitivity it can not be real-time operation. In this chapter, we employed a FLC-SLM as a real-time film instead of a photographic plate to detect difference between two images quickly.

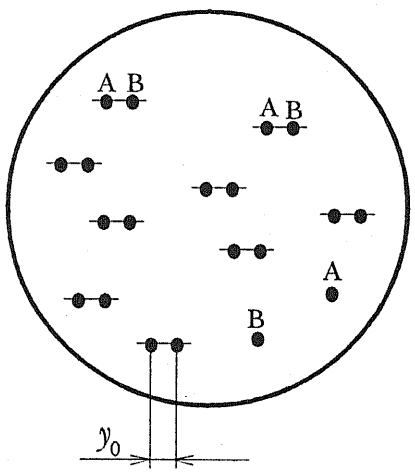

Fig. 4.2 Structure of the resulting speckle on H.

4.1.3 The Light Distribution in the Image Plane

The technique just described may be explained by means of a very simple mathematical development. When the two images modulated by speckle pattern at a x-y coordinate are exposed twice on the real-time imaging device such as a FLC-SLM used in this experiment and the speckle translation y_0 to the y-direction between the successive exposures are introduced, the total intensity $t(x,y)$ to be recorded is written by

$$t(x,y) = [a(x,y)\cdot g(x,y)]*\delta(x,y+\frac{y_0}{2}) + [b(x,y)\cdot g(x,y)]*\delta(x,y-\frac{y_0}{2})$$
$$= [a(x,y)\cdot g(x,y)]*[\delta(x,y+\frac{y_0}{2}) + \delta(x,y-\frac{y_0}{2})] \qquad (4.3)$$
$$-[d(x,y)\cdot g(x,y)]*\delta(x,y-\frac{y_0}{2}),$$

where $d(x,y) = a(x,y) - b(x,y)$ is the difference between the two images, $a(x,y)$ and $b(x,y)$ are the functions corresponding to the images A and B, respectively, and $g(x,y)$ represents the speckle pattern. The optical Fourier transform of the intensity $t(x,y)$ is given by

$$T(u,v) = 2[A(u,v)*G(u,v)]\cdot\cos(\frac{\pi v}{\lambda}y_0) - [D(u,v)*G(u,v)]\cdot\exp(-j\frac{\pi v}{\lambda}y_0). \qquad (4.4)$$

The first term of Eq. (4.4) is a fringe term produced by the speckle translation. If the Fourier transformed pattern is filtered and the information around the dark fringes, i.e. $\cos(\pi v y_0/\lambda) \sim 0$, is passed through the filter, only the second term is extracted and the subtraction of the images is obtained by the optical Fourier transform of the filtered pattern. If the speckles are fine enough in the image space, the Fourier function $G(u,v)$ becomes a broad function and the information of the image subtraction $D(u,v)$ is fully extracted by the filtering.

With two exposures, the first term of Eq. (4.4) is modulated by Young's fringes as shown in curve 1 in Fig. 4.3. Then, the slope of the curve at M is non-zero. In order to let go through the least amount of light from the identical regions of A and B, a narrow slit must be used and this is not favorable to the quality of the filtered image. To improve the quality of the filtered image by modifying the shape of the fringes, three- or multiple-exposure technique is employed to obtain a sufficient intensity level.[4.2] In the proposed real-time image processing, a three-exposure technique of the patterns is demonstrated by using the multiple-exposure capability of a FLC-SLM. In the three-exposure procedure, at first, a spatial translation $-y_0$ of the speckle pattern associated to the image A is given for an exposure time $t_0/2$ and, then, the

image B modulated by the speckle pattern without translation is exposed for a duration t_0. Finally, the image A modulated by the translated speckle pattern with y_0 is exposed for $t_0/2$, i.e. the exposure times proportional to the binomial coefficients. These recordings are tabulated in Table 4.1.

Table 4.1 Three-exposure recordings

Exposure	Images	Translation	Exposure time
1st	A	$-y_0$	$t_0/2$
2nd	B	0	t_0
3rd	A	y_0	$t_0/2$

The recorded light intensity on the FLC-SLM is given by

$$\begin{aligned} t(x,y) &= [a(x,y)\cdot g(x,y)]*[\frac{1}{2}\delta(x,y+y_0)+\frac{1}{2}\delta(x,y-y_0)] \\ &\quad +[b(x,y)\cdot g(x,y)]*\delta(x,y) \\ &= [a(x,y)\cdot g(x,y)]*[\delta(x,y)+\frac{1}{2}\delta(x,y+y_0)+\frac{1}{2}\delta(x,y-y_0)] \\ &\quad -[d(x,y)\cdot g(x,y)]*\delta(x,y), \end{aligned} \tag{4.5}$$

and the corresponding Fourier spectrum is calculated as

$$T(u,v) = 2[A(u,v)*G(u,v)]\cdot\cos^2(\frac{\pi v}{\lambda}y_0)-[D(u,v)*G(u,v)]. \tag{4.6}$$

The fringe modulation is proportional to the square of the cosine term which is represented by curve 2 in Fig. 4.3. The resulting flat minimum at M, i. e., the dark fringe parts are enlarged compared with those of the two-exposure. The necessary information here is again only the

difference of the two images and it can be extracted for the negligible small value of the first term in Eq. (4.6). Thus, comparing with two exposure case, we can use a wider slit to filter the Fourier pattern and obtain a good filtered image.

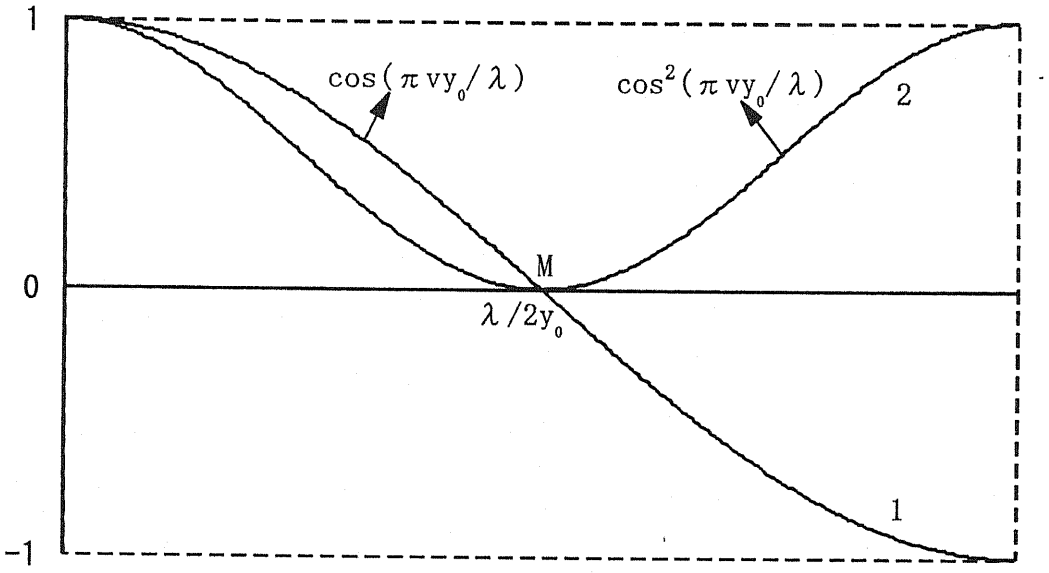

Fig. 4.3 Structure of the fringes in the spectrum for two exposures (curve 1) and for three exposures (curve 2).

4.2 OPTICAL IMAGE SUBTRACTION

Real-time image subtraction is extremely important in image processing. Recently, a real-time image subtraction by using a polarization modulation of LCTV-SLM has been proposed.[4.11] But twisted nematic liquid crystals used for LCTV-SLMs has a slow response time and they can operate at most by a video frame rate. However, the operation speed of the proposed

system in this section is faster than 10 ms at the modest operations of the FLC devices and the potential speed of ferro-electric crystal devices is two times or more faster than that of twisted nematic crystal devices.

4.2.1 Optical Experiment

Figure 4.4 shows the whole optical setup for real-time detection of the difference between two images based on speckle modulation. The right half of the figure is the write-in system for the three-exposure image and the left half is the read-out system of the exposed image and the optical filtering system. A ground glass plate is illuminated by a laser beam from a 50 mW He-Ne laser (Laser 1) at a wavelength of 633 nm. The depolarization effect through a ground glass plate is usually small as far as its surface roughness is around or less than the optical wavelength and the transmitted light through the ground glass, i.e. the generated speckle pattern, is assumed to be linearly polarized. The speckle pattern is divided by a half mirror HM and each pattern illuminates the image A or B through a lens L1 (f=100 mm). Birefringent calcite ($CaCO_3$) plates BP1 and BP2 are employed to give appropriate spatial offsets to the speckle pattern. Three FLC polarization switches PS1, PS2, and PS3 with clear apertures of 12 mm are used to realize three exposures in real time. The polarization of an input light through the FLC switch can be rotated by 90° by a positive applied voltage to the FLC cell. The maximum switching speed of the FLC polarization switches is 50 μs.

The detail of the real-time three-exposure technique is schematically shown in Fig. 4.5. It is noted that the propagation of light here is from right to left in this figure. In Fig. 4.5 (a), the linearly polarized speckle pattern passes through the FLC polarization switch PS1 as a p-polarized pattern due to the negative applied voltage to the polarization switch. The p-polarized pattern is shifted by the birefringent plate BP1 as an extraordinary ray. The amount of the shift depends on the length of the birefringent calcite crystal along the light transmission. In our experiment, the birefringent plate has a size of 20×20 mm^2 and the thickness of the

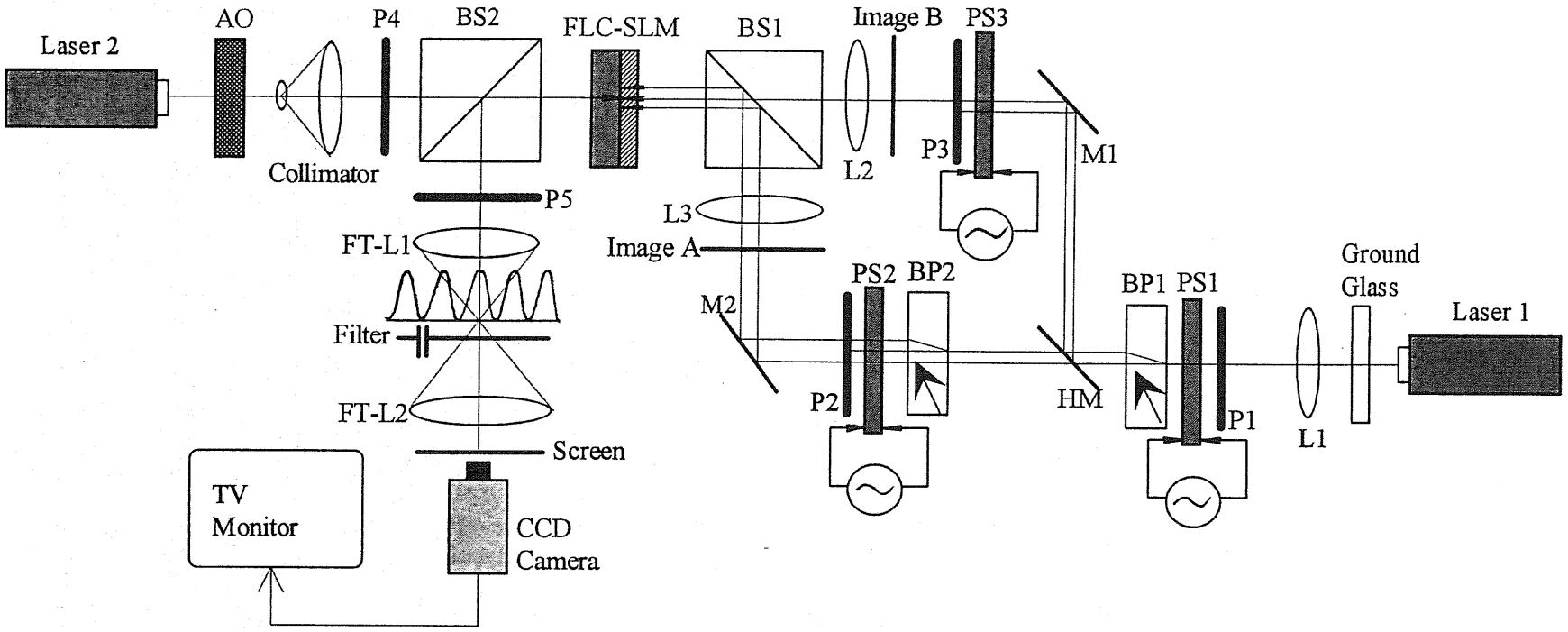

Fig. 4.4 Experimental setup for the proposed real-time detection of the difference between two images. L1-L3: lenses, P1-P5: polarizers, PS1-PS3: FLC polarization switches, BP1-BP2: birefringent plates, HM: half mirror, BS1, BS2: beam splitters, AO: acousto-optic modulator, and FT-L1, FT-L2: Fourier transform lenses.

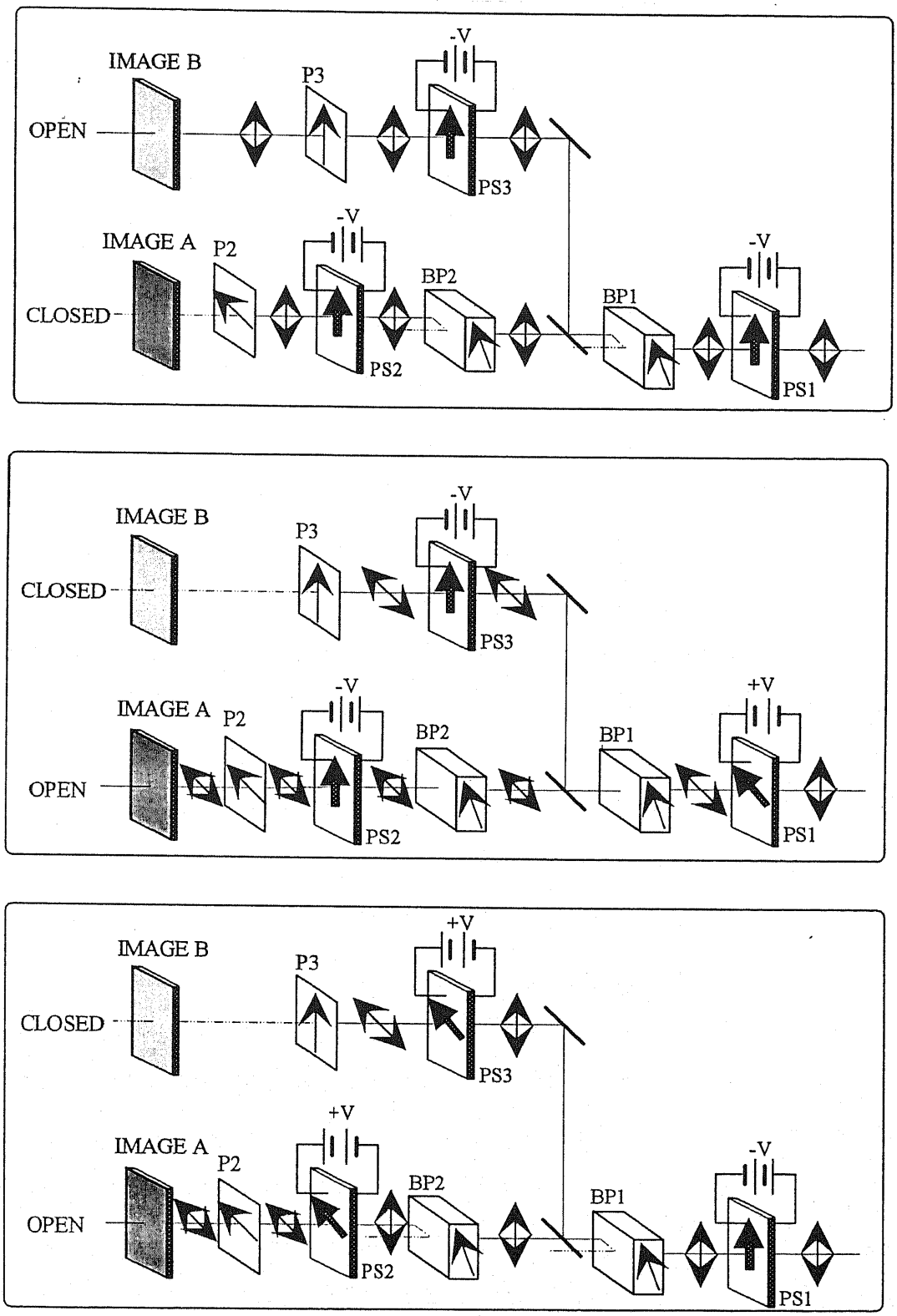

Fig. 4.5 Principle operations for the real-time spatial shifts of a speckle pattern and the three exposures.

crystal is 4.59 mm which corresponds to a spatial shift of the extraordinary ray of 0.5 mm at the wavelength of 633 nm. One of the shifted patterns which is divided by the half mirror is fed to another birefringent plate BP2 and also has a further shift of 0.5 mm through it. The FLC polarization switch PS2 is driven by a negative voltage at this time and the output speckle pattern is a p-polarized pattern. Then, the speckle pattern is blocked out by the polarizer P2 and the image A is not written onto the FLC-SLM. The other pattern passes through the polarization switch PS3 driven by a negative voltage and the pattern through PS3 is a p-polarized one. The speckle pattern passes through the polarizer P3 and the product of the speckle pattern with the image B is taken. Then, the image B with the speckle pattern is exposed onto the FLC-SLM for a time duration of t_0. In the following, this speckle pattern is assumed to be zero shift on the FLC-SLM. In Fig. 4.5 (b), the p-polarized speckle pattern is switched to a s-polarized one by the positive applied voltage to the polarization switch PS1. The switched ordinary-ray pattern is not shifted by the birefringent plate BP1 and it is multiplied with the image A as shown in the figure. Then, the image A with the shifted speckle pattern having the amount of the shift is $-y_0$ with respect to the first exposure pattern is exposed onto the FLC-SLM for a time duration of $t_0/2$. As the same manner, the image A with a shifted speckle pattern having the shift of y_0 is also exposed onto the FLC-SLM for a time duration of $t_0/2$ as shown in Fig. 4.5 (c). Thus, the three exposures of the images are taken by using the multiple-exposure capability of the FLC-SLM.

The lenses L2 and L3 used in the experiments in Fig. 4.4 have focal lengths of 100 mm and the both magnifications of the imaging systems are unity, so that the shift y_0 of the speckle pattern is 0.5 mm on the FLC-SLM. The average speckle size on the FLC-SLM is 25 μm which is enough larger than the spatial resolution of the FLC-SLM. The images with unshifted and shifted speckles are exposed by the FLC-SLM. The FLC-SLM used here is developed by NTT and fabricated by Hamamatsu Photonics, K.K. The clear aperture of the FLC-SLM is 20×20 mm^2 and the average light power on the FLC-SLM used in the experiments was roughly estimated to be several hundreds $\mu W/cm^2$. The spatial resolution of

the FLC-SLM is measured to be more than 100 *l*p/mm at the experimental condition. The general operation characteristics and structures of FLC-SLMs have been described in Section 2.2. The switching speed of a FLC-SLM depends on the incoming light intensity and the typical switching speed of the FLC-SLM used is less than 100 μs. The FLC-SLM is operated by synchronizing with the FLC polarization switches under the control of a micro-computer.

A typical example of the driving voltages for the FLC-SLM and the FLC polarization switches is shown in Fig. 4.6. Figure 4.6 (a) is the trace of the voltage of two cycles for the FLC-SLM. The modulation voltages both for the FLC-SLM and the FLC polarization switches were 30 V at peak-to-peak value with zero mean. In Fig. 4.6 (a), an erase pulse to eliminate the previous pattern due to the bistable characteristic of the device had typically 4 ms duration. The write-in pulse duration for the first exposure with a positive applied voltage to the FLC-SLM was t_0=300 μs and the pulse durations for the second and third exposures were the same as t_0 / 2=150 μs. Dead times of 800 μs among each write-in pulse were introduced to adjust the operations of the FLC-SLM and the FLC polarization switches. From Fig. 4.6 (b) to (d), the driving voltages for the FLC polarization switches synchronized with the FLC-SLM operation are shown. The FLC polarization switches were not driven by squared wave signals but specifically optimized waveforms to facilitate faster switchings of the FLC material. Then, the waveforms exhibits a ±15 V switching transient which quickly decays of about 300 μs to a ±5 V switching voltage as illustrated from Figs. 4.6 (b) to (d). For each write-in pulse of the FLC-SLM, it is easily recognized that the corresponding applied voltages of the polarization switches are consistent with the operations shown in Fig. 4.5. The total cycle time of the read-write is within several ms in this case, but it can be much shortened by employing higher intensities of the write-in and read-out beams.

After the third exposure, the three-exposed pattern was read by a collimated read-out light of a 10 mW He-Ne laser from Laser 2 as shown in Fig. 4.4. The read-out beam form Laser 2 was turned on by an acousto-optic modulator AO only at the reading operation to avoid unnecessary exposures to the FLC-SLM. The three-exposure pattern was Fourier

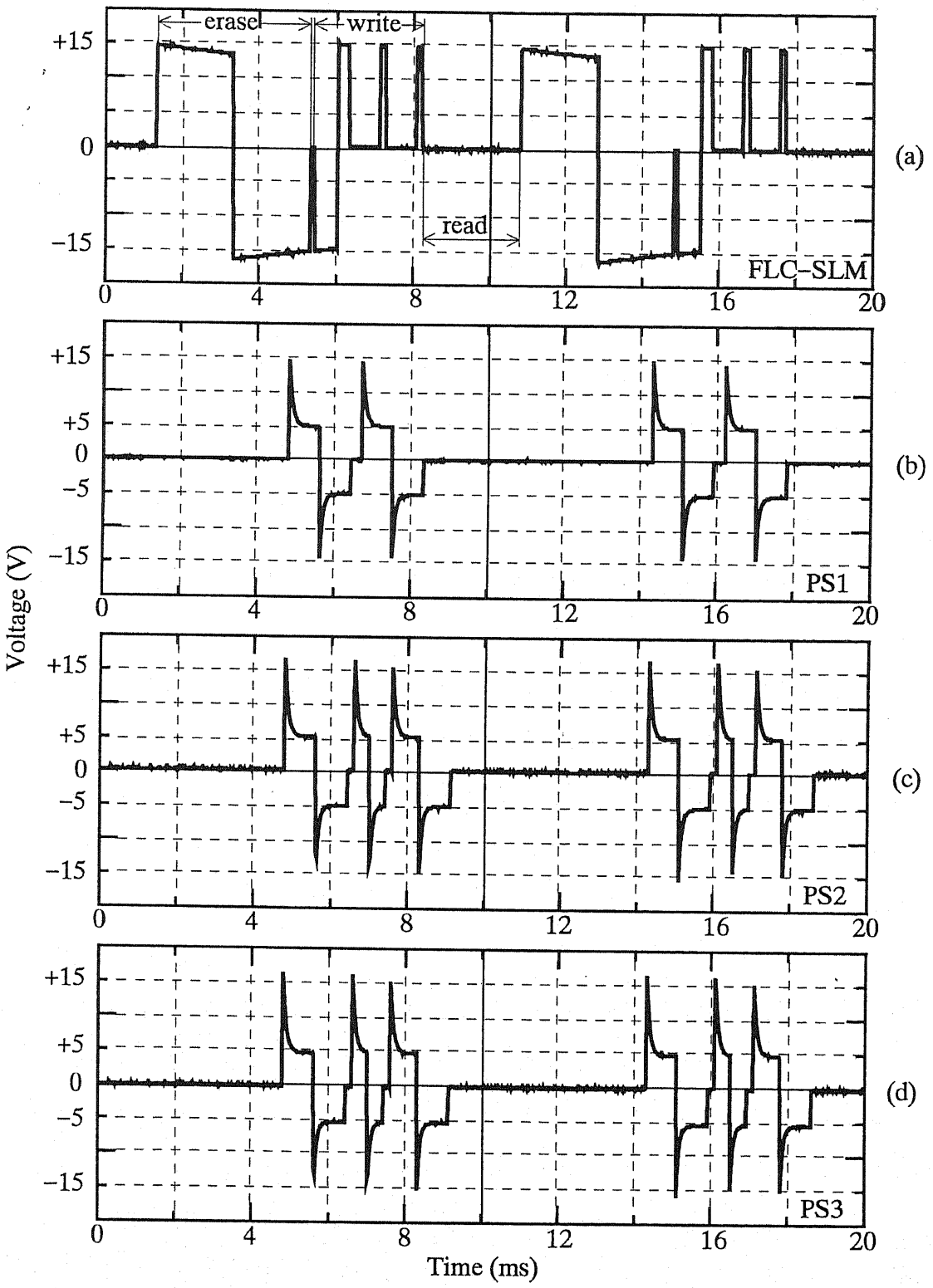

Fig. 4.6 Electrical signals to drive the FLC-SLM (a) and the FLC polarization switches PS1-PS3 (from (b) to (d)).

transformed by a lens FT-L1 (f=400 mm) and the fringe pattern produced by the three exposures was enlarged by an objective lens (×10) which is not shown in Fig. 4.4. The typical fringe separations are 2.4 mm at the Fourier plane. A slit filter of a width of 1 mm was placed at the Fourier plane to pass through a dark fringe. The filtered amplitude which has the information of the image subtraction as discussed in section 4.1 was again optically Fourier transformed by a lens FT-L2 (f=400 mm). The resulted output pattern was imaged onto a screen and taken by a CCD camera. Finally, the difference of the two image was displayed on a TV monitor. The whole operation of the system was controlled by the microcomputer.

4.2.2 Results and Discussion

Based on the proposed three-exposure technique, the real-time image subtraction was performed. At first, we compare the fringe patterns for two- and three-exposure images in the experimental system. A speckle pattern produced by a ground glass plate without input images in Fig. 4.4 was used to write two- and three-exposure patterns on the FLC-SLM. Figure 4.7 shows an example of observed Fourier fringes for two- and three-exposure patterns taken by the system shown in Fig. 4.4. Of course, the proposed system can be used as a two-exposure system by appropriate drives and timings for the FLC-SLM and FLC polarization switch voltages. In Fig. 4.7 (a), the observed dark fringes for the two exposures are so narrow that we must use a fine slit to extract the required information. This results in an obscure and noisy filtered output image. On the other hand, the dark parts of the fringes are enlarged for the three-exposure case as shown in Fig. 4.7 (b) and, thus, we can obtain a better filtered image. In this experiment, we used only a single slit filter. Nevertheless, the intensity levels and image qualities of the obtained results were satisfactory due to the employment of the three exposures. But high intensity and better quality images can be obtained by employing a multiple-slit filter at the Fourier plane.

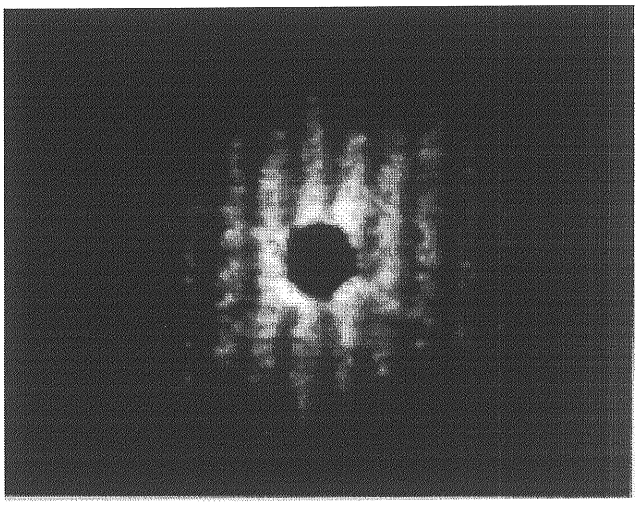

(a)

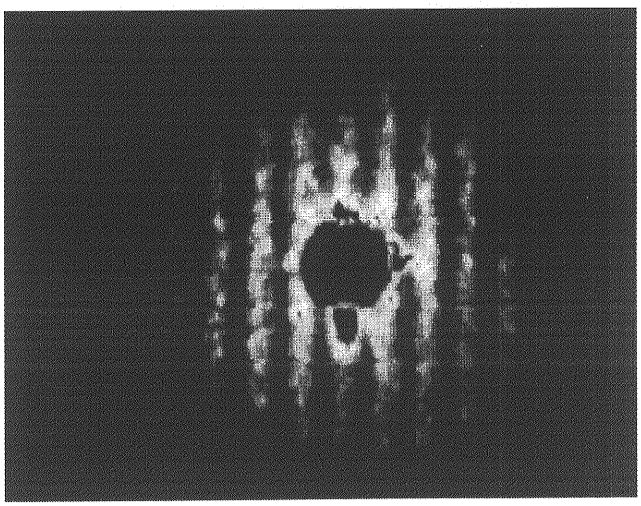

(b)

Fig. 4.7 Examples of the Fourier fringes observed in the experimental system with speckle patterns only. Fringe patterns for a two-exposure (a) and for a three-exposure (b).

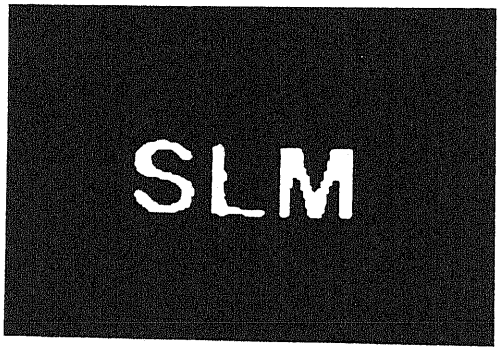

(a)

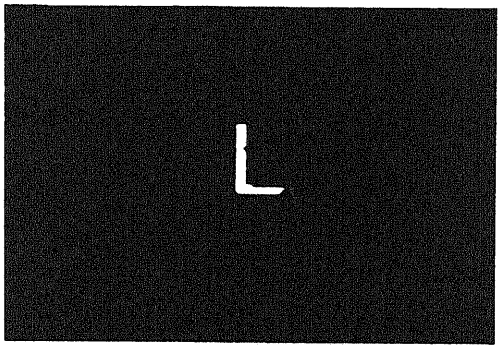

(b)

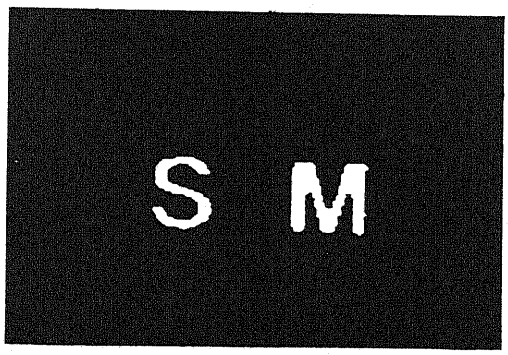

(c)

Fig. 4.8 Result of an image subtraction. (a) image A, (b) image B, and (c) result of the image subtraction A-B.

Figure 4.8 shows an example of the image subtraction by using the proposed system. The two original input patterns are letters "SLM" and "L" as shown in Figs. 4.8 (a) and (b), respectively. The letters "L"s in the both patterns were imaged at exactly the same position on the FLC-SLM. These letters were recorded on the FLC-SLM with speckle patterns by the three-exposure technique as already discussed. The each letter size was about 3×3 mm^2 on the FLC-SLM. The three-exposure pattern was optically Fourier transformed and filtered by the single slit filter. Then, the final output of the image subtraction was obtained by the Fourier transform of the filtered pattern and detected by the CCD camera as shown in Fig. 4.8 (c). The pattern taken by the CCD camera is digitized by 0 to 255 gray scale and the signal levels of the characters "S" and "M" in Fig. 4.8 (c) are from 140 to 150. The background noise levels are 20 and the levels for the residue of the subtracted image "L" are around 50. The noise and residue are not visible in this figure due to the small dynamic range of the photocopy. The obtained result is satisfactory and the modulation effect by the speckle grains is actually not visible because each speckle is so fine.

4.3 OPTICAL EDGE ENHANCEMENT

Edge enhancement is used in optical associative memory,[4.12] biological sample observation,[4.13] and image processing.[4.14] In the optical pattern recognition, the edge enhancement is one of the most important preprocessing techniques. For example, in an optical correlator, cross-correlation signals associated with input objects that are similar to the reference image can be greatly reduced by using the edge enhancement technique.

There exists several methods to perform a real-time optical edge enhancement of an image. For example, a high pass filter in a optical filtering system is used to obtain an edge enhanced image. But, in this case, the intensity level of the resulted image is low due to the cut of the DC component. Therefore, a phase filter which blocks around the zero order diffraction spot is sometimes used as a rough approximate high pass filter to obtain a high intensity

image. Another example is the method by utilizing real-time optical materials such as a specially designed edge enhancing SLM[4.15-17] and photorefractive crystals.[4.18-19] However, a high power laser source is usually necessary for the system operations and only a small portion of the input light power can be used as an output. Further, a careful adjustment is required for the arrangements of such optical systems. On the other hand, the optical arrangement is not so difficult and the high output power efficiency can be attained by the employment of the multiple-slit filter in the proposed method.

In this section, we propose a novel real-time edge enhancement by using the FLC devices based on the speckle defocusing modulation and the operation speed of the proposed system is faster than 10 ms at the modest operations of the FLC devices.

4.3.1 Principles of the Method

The real-time edge enhancement of an image is conducted based on the same principle of the proposed image subtraction in Section 4.2. Consider the case that one of two images, say the image B, is the same as the image A, but the imaging system for the image B(=A) is defocused. The speckle patterns to be modulated are almost identical between the images A and B as far as the amount of the defocus is much less than the distance between the imaging lens and the FLC-SLM plane. Then, the function $D(u,v)$ in Eq. (4.6) is written by

$$D(u,v) = A(u,v)\cdot[1 - H(u,v)], \tag{4.7}$$

where the function $H(u,v)$ is the optical transfer function (OTF) for the defocused imaging system. The effect of a focusing error on the OTF is discussed in Appendix B. For example, for a rectangular aperture, the OTF is given by

$$H(u,v) = \Lambda(\frac{u}{2f_0}) \cdot \Lambda(\frac{v}{2f_0}) \cdot \mathrm{sinc}[\frac{8w}{\lambda}(\frac{u}{2f_0})(1-\frac{|u|}{2f_0})] \times \mathrm{sinc}[\frac{8w}{\lambda}(\frac{v}{2f_0})(1-\frac{|v|}{2f_0})]. \tag{4.8}$$

Here, $\Lambda(\cdot)$ and $\mathrm{sinc}(\cdot)$ are triangle and sinc functions, respectively, f_0 denotes the coherent cutoff frequency of the imaging system, and w represents the maximum path-length error.

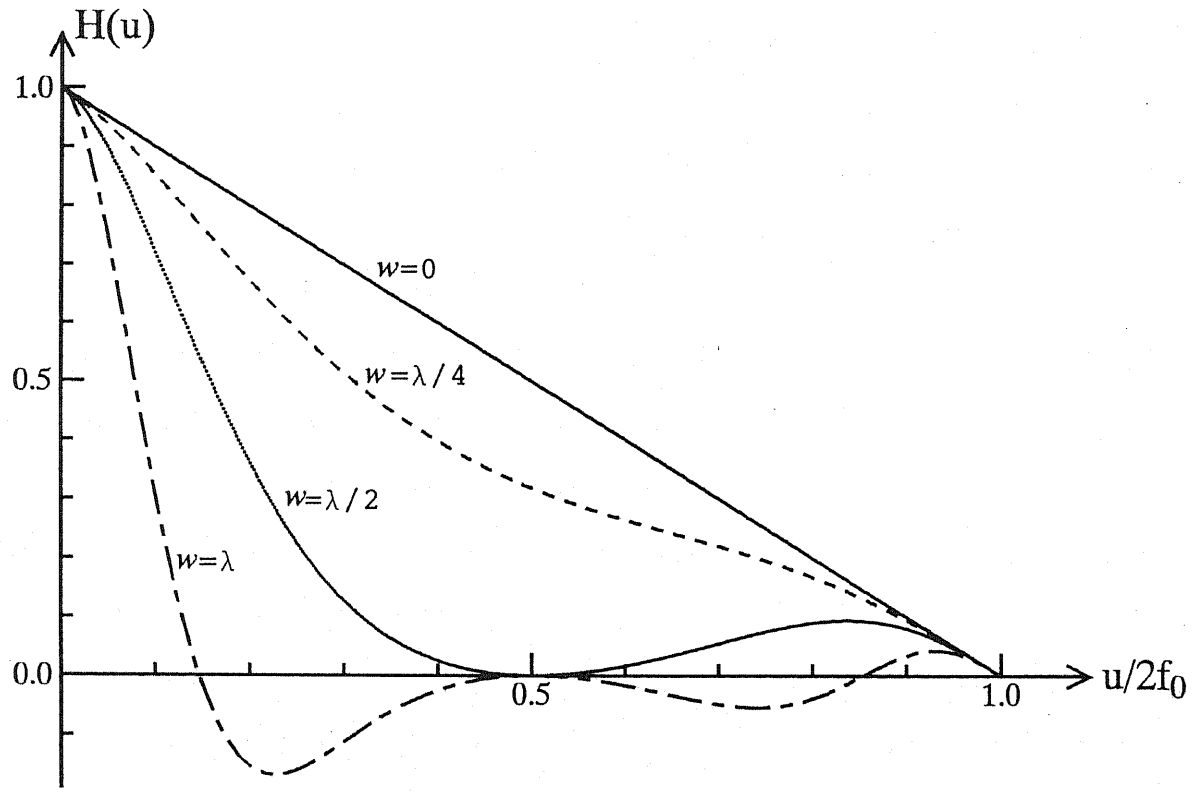

Fig. 4.9 Cross section of the OTF with defocus for a rectangular aperture. The parameter w is the maximum path-length error.

Figure 4.9 shows a one-dimensional plot of the OTF for various parameter values of w. If the second factor $1 - H(u,v)$ of Eq. (4.7) is approximated by $(jku)(jkv)$ (k being a certain constant), then, the exactly differentiated pattern of the image A, namely the edge enhanced image, would be obtained by the Fourier transform of Eq. (4.7). In actual, for a rectangular aperture, the second factor is not proportional to uv but rather to u^2v^2 for a large amount of defocus. However, as seen from Fig. 4.9, the OTF for a large amount of defocus has wide linear region and the second factor in Eq. (4.7) can be assumed as a low pass filter. Thus, the proposed system behaves as an approximate edge enhancement system for the input image.

There are several techniques of edge enhancement based on digital image processing. For example, unsharp masking[4.20] is a similar technique of edge enhancement which subtracts an image from its blurred version in a digital computer. As is already discussed, fast optical techniques for image edge enhancement are expected in many applications of image processing. The proposed system is promising one for a fast optical image edge enhancement.

4.3.2 Experiments and Results

The same optical system shown in Fig. 4.4 is used for the real-time edge enhancement. But the image B is the same as the image A, and the imaging system for B(=A) is defocused. Figure 4.10 shows two examples of the results for the edge enhancement of images. Figure 4.10 (a) shows two defocused input patterns and Fig. 4.10 (b) shows the output patterns taken by the CCD camera for the corresponding inputs. The maximum path-length error w introduced to generate the defocused image is about $w = \lambda / 2$ which is calculated from the aperture size of the imaging lens l=40 mm (in the actual experiment, the aperture is circular) and the amount of the defocus of about 60 μm. The OTF curve for the maximum path-length error $w = \lambda / 2$ has already been plotted in Fig. 4.9. In this experiment, the speckle patterns were shifted to the horizontal direction in the figure. In spite of the roughly approximate system response for the differentiation and one-dimensional shift of the speckle patterns, the obtained results are quite

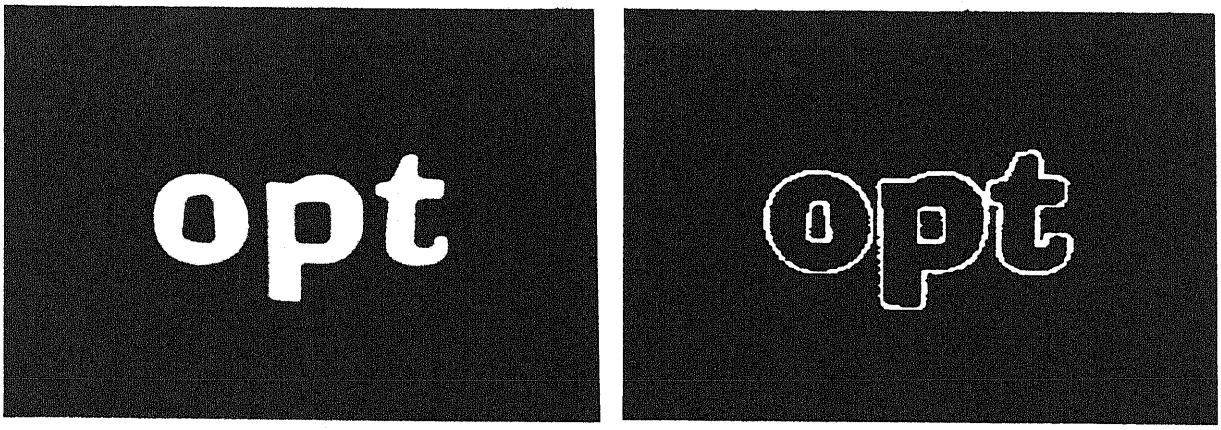

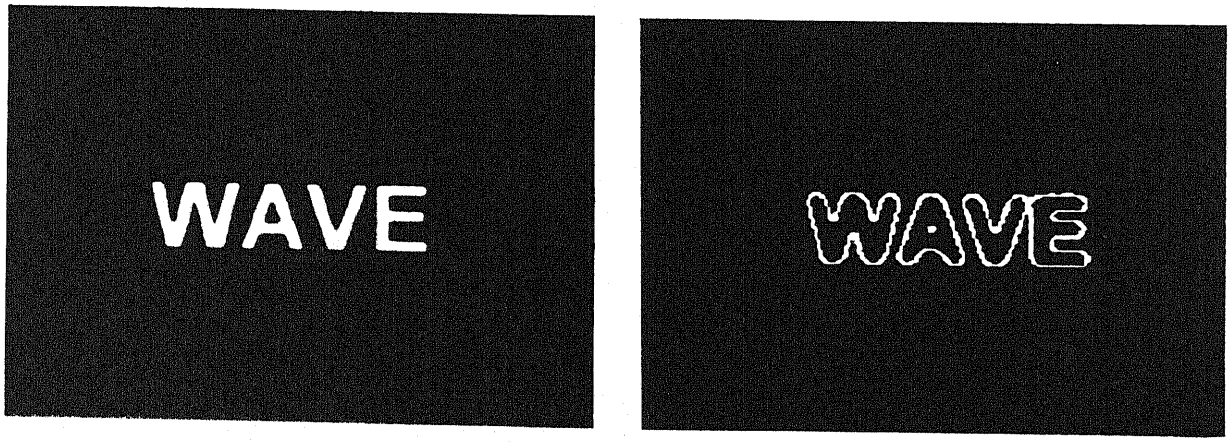

(a) (b)

Fig. 4.10 Results of image edge enhancements. (a) input images and (b) results of the edge enhancements.

satisfactory and the speckle-grain effect is scarcely observed in the edge enhanced images.

4.4 SUMMARY

We have described real-time optical image subtraction and edge enhancement by using FLC devices based on speckle modulation technique and have successfully realized the real-time high-speed image subtraction and edge enhancement. The spatial shifts for a speckle pattern have been easily given through optical components consisted of the combination of FLC polarization switches and birefringent plates, and multiple-exposure images through a focused or defocused imaging system have been written onto the FLC-SLM. The subtracted and edge enhanced images have been successfully obtained from these multiple-exposure patterns by the Fourier filtering. There are several method for real-time image subtraction and edge enhancement, however, the proposed method has some advantages over the previous methods as discussed in Sections 4.2 and 4.3.

FLC devices have attractive features of high-speed switching, memory effect and multiple exposures, and polarization and intensity switching capabilities, and they surely become promising devices for real-time optical information processing and optical computing. One of the drawbacks of currently available FLC-SLMs may be the sensitivity for a write-in intensity. This point should be improved to realize a faster, compact, and small power laser system in these fields.

REFERENCES

4.1 S. Debrus, M. Françon, and P. Koulev, *Nouv. Rev. d'Opt.* **5,** 153 (1974).

4.2 M. Françon, *Laser Speckle and Applications in Optics* (Academic Press, New York, 1979).

4.3 E. Marom, and I. Kasher, *J.Opt.* **8,** 5 (1977).

4.4 J. P. Sharpe, and K. M. Johnson, *Appl. Opt.* **31**, 7399 (1992).

4.5 D. Cunningham, J. Sharpe, and K. M. Johnson, *Opt. Commun.* **101**, 311 (1993).

4.6 X. Lin, J. Ohtsubo, and T. Takemori, *Rep. Grad. School Electron. Sci. Technol. Shizuoka Univ.* **16,** 133 (1995).

4.7 C. C. Mao, K. M. Johnson, and G. Moddel, *Ferroelectrics* **114**, 45 (1991).

4.8 S. Fukushima, T. Kurokawa, and M. Ohno, *Appl. Phys. Lett.* **58,** 787 (1991).

4.9 D. C. O'Brien, R. J. Mears, T. D. Wilkinson, and W. A. Crossland, *Appl. Opt.* **33**, 2795 (1994).

4.10 C. M. Gomes, H. Sekine, T. yamazaki, and S. Kobayashi, *Neural Networks,* **5,** 169 (1992).

4.11 H. Sakai and J. Ohtsubo, *Appl. Opt.* **31**, 6852 (1992).

4.12 T. S. Chao, *OSA Technical Digest Series* **14**, 28 (1990).

4.13 W. Richards, H. K. Nishihara, and B. Dawson, *MIT Applied Intelligence Laboratory Memo* p.688 (Massachusetts Institute of Technology, Cambridge, Mass., 1982).

4.14 D. Marr and E. Hildreth, *Proc. R. Soc. London Ser.* B **207,** 187 (1980).

4.15 C. C. Mao, K. M. Johnson, R. Turner, D. Jared, and D. Doroski, *Appl. Opt.* **31**, 3908 (1992).

4.16 T. H. Chao, *Appl. Opt.* **28**, 4727 (1989).

4.17 D. Armitage and J. I. Thackara, *Appl. Opt.* **28**, 219 (1989).

4.18 J. Feinberg, *Opt. Lett.* **5**, 330 (1980).

4.19 J. P. Huignard, and J. P. Herriau, *Appl. Opt.* **17**, 2671 (1978).

4.20 R. C. Gonzales, and P. Winz, *Digital Image Processing* p.115 (Addison-Wesley Pub., Massachusetts, 1977).

Optical associative memory for pattern recognition using the Hopfield model has the advantage of the simplicity of its structure of the memory. But the further investigations reveal that the storage capacity of the Hopfield model is quite limited because of the number of spurious states and oscillations. In order to alleviate the spurious state in the Hopfield neural network, the concept of the terminal attractor (TA) has been introduced. In this chapter, we apply the TA model to associative memory neural network for pattern recognition and compare it with the conventional Hopfield model. The computer simulations for pattern recognition have been performed by using 6×6 neurons and 3 stored patterns in the network. For the feasibility of optical implementation of the TA model, a neural network with 4×4 neurons and 3 stored patterns is tested by using LCTV-SLMs in the experiment. These results indicate that the TA model can reduce spurious states in the Hopfield neural network and the recalling capability can be much improved.

CHAPTER 5

OPTICAL ASSOCIATIVE MEMORY FOR PATTERN RECOGNITION

Neural network modeling has given an impetus to work in the fields of electronic and optical information processing since early 1960s.[5.1-3] It is well known that neural networks in the human eye-brain system process information in parallel with the aid of large numbers of simple interconnected processing elements, i.e., the neurons. It is also known that the system is very adept at recognition and recall from partial information and has remarkable error correction capabilities.

Two broad approaches to implement optical analogues of neural networks have been developed. The first approach utilizes vector-matrix-oriented optical processors based on spatial light modulators and/or arrays of emitters and detectors.[5.3-4] The second approach uses a holographically oriented processor based either on nonlinear media with saturable gain or on holograms used in resonator cavities.[5.5-8]

In this chapter, we present a new optical associative memory neural network for pattern recognition based on the TA model and compare it with the conventional Hopfield model associative memory. LCTV-SLMs are used for the optical realization of such a system. Since most of optical devices used for a SLM have a binary nature, we modified the TA model to agree with optical system.

5.1 CONVENTIONAL ASSOCIATIVE MEMORY

Pattern recognition in neural networks is based upon a selection of memories (from N given categories) into which a certain set of pattern are stored. Hopfield described a simple neural network model for the operation of pattern recognition and associative memory.[5.7] The action of individual neurons is modeled through a thresholding operation and the information is stored in a stable equilibrium points in the interconnections among the neurons. The computation is performed by setting the state (on or off) of some of the neurons according to external stimulus and, with the interconnections according to the recipe that Hopfield prescribed, the state of all neurons that are interconnected to those that are externally stimulated

spontaneously converge to the stored pattern that is the most similar to the external input. The basic operation performed is a nearest-neighbor search, a fundamental operation for pattern recognition, associative memory, and error correction.

5.1.1 Basic Model

Let us consider a discrete type of the Hopfield neural network consisting of N neurons with outputs ± 1 as shown in Fig. 5.1. We represent the connection weight from the jth neuron to the ith one by W_{ij} and the output of the ith neuron at time t by $x_i(t)$. This network has 2^N possible states, and the current state is described by an N-dimensional vector $X = (x_1,\ldots,x_n)^T$, where the superscript T denotes the transpose. We will denote the network state at time t by X_t.

Let $X^{(1)}, X^{(2)},\ldots, X^{(M)}$ be binary patterns (represented by column vectors) to be stored in the network and $x_i^{(m)}$ ($=\pm 1$) be the ith component of $X^{(m)}$. We assume that N and M are sufficiently large and that $X^{(m)}$ is randomly chosen out of the 2^N possible patterns. Then, these patterns are almost orthogonal to each other, i.e.,

$$\frac{1}{N}\sum_{i=1}^{N} x_i^{(m)} x_i^{(n)} \approx 0 \quad (m \neq n). \tag{5.1}$$

In the Hopfield neural network associative memory, the $X^{(m)}(m = 1,\ldots,M)$ is stored in the network using the weight matrix $W = \left[W_{ij}\right]$ given by

$$W_{ij} = \sum_{m=1}^{M} x_i^{(m)} x_j^{(m)} \qquad i, j = 1,2,3,\ldots,N, \tag{5.2}$$

$$W_{ii} = 0. \tag{5.3}$$

The neural network dynamics for the recalling of the stored patterns is give by

$$x_i(t+1) = \text{sgn}\left(\sum_{j=1}^{N} W_{ij} x_j(t)\right), \tag{5.4}$$

where sgn(u)=1 when $u > 0$ and -1 when $u < 0$ is a threshold operation function. The network changes its state at discrete times $t = 0,1,2,\ldots$ according to

$$X_{t+1} = \text{sgn}(WX_t), \tag{5.5}$$

where the function sgn operates componentwise on vectors.

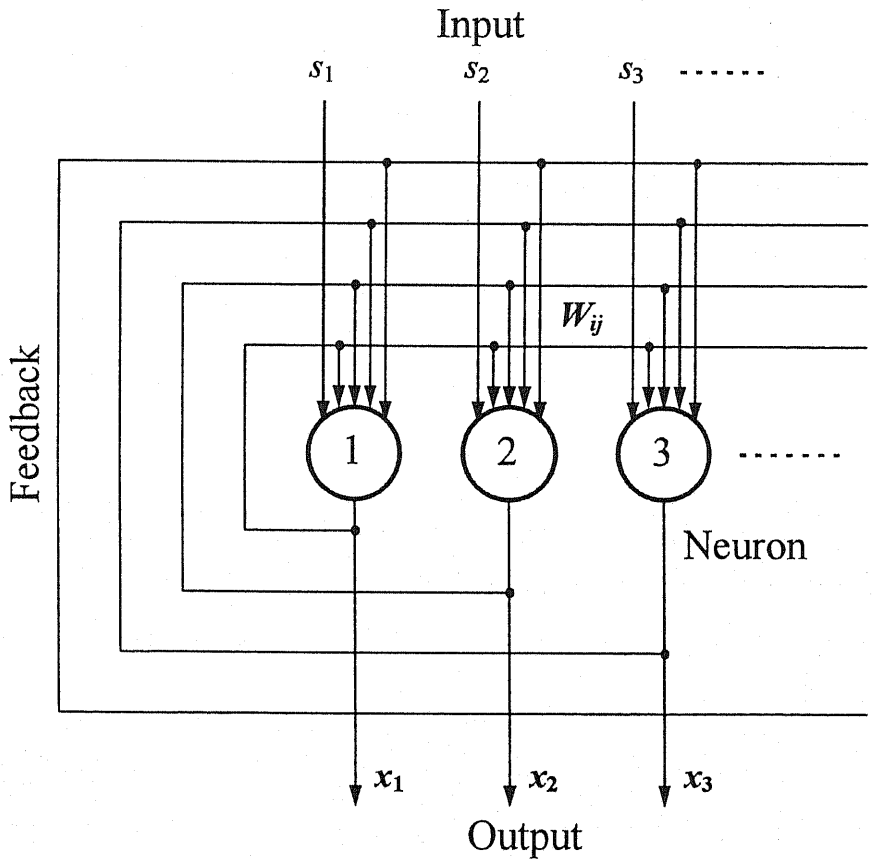

Fig. 5.1 The basic operation of the Hopfield model neural network

When the memory is addressed with a bipolar valued pattern that is not one of the stored patterns, the weight matrix multiplication and thresholding operation yield an output bipolar valued pattern which, in general, is an approximation of the stored pattern that is at the shortest Hamming distance from the input pattern. If this output pattern is fed back and used as the input to the memory, the new output is generally a more accurate version of the stored pattern and continued iteration converges to the correct pattern. During this process, the energy of the network

$$E = -\frac{1}{2}\sum_{i=1}^{N}\sum_{j=1}^{N} W_{ij}x_i x_j , \tag{5.6}$$

decreases with time so that the network state finally settles in an equilibrium corresponding to a minimum of the energy. Since E can be rewritten as

$$\begin{aligned} E &= -\frac{1}{2}\sum_{i=1}^{N}\sum_{j=1}^{N}\left(\sum_{m=1}^{M} x_i^{(m)}x_j^{(m)}\right)x_i x_j \\ &= -\frac{1}{2}\sum_{m=1}^{M}\left(\sum_{i=1}^{N} x_i^{(m)}x_i\right)^2 , \end{aligned} \tag{5.7}$$

it is considered that E has a minimum at $X^{(m)}$. Consequently, when an initial state sufficiently close to a stored pattern is given, the network state X is expected to reach an equilibrium which is identical or very close to the stored pattern.

5.1.2 Memory Capacity

The capacity estimation[5.9] of the Hopfield associative memory was based on the assumption that M of the randomly chosen N bipolar vectors are used for the storage. When the network is probed by one of the possible N vectors that are less than a Hamming distance $N/2$ away from

the fundamental memory, the maximum asymptotic value of M can be no more than $N/(4\log N)$ as N approaches infinity. This is called the absolute capacity, i.e., it is the maximum number of randomly generated patterns which are memorized as the equilibrium of the network with the correlation-type connection weights. On the other hand, Hopfield showed by a computer simulation that the memory capacity of the associative memory is approximately $M = 0.15N$, where N is the number of neurons. Namely, the Hopfield model associative memory can recall randomly generated patterns up to $0.15N$ with a small error. This is called the relative capacity.

These investigation reveal that the storage capacity of the Hopfield model is quite limited. Its absolute capacity of $N/(4\log N)$ is smaller than N in order and its relative capacity of $0.15N$ is also not large. When the ratio of the number of stored patterns to that of neurons (i.e. memory ratio) $r = M/N$ is greater than about 0.15, the network state will converge to an equilibrium state which is very different from the stored patterns, i.e., a spurious memory is recalled, no matter how large the initial overlap may be.

5.1.3 Discussion

The limitation of the capacity of the Hopfield model is partially caused by the existence of spurious states. The spurious states arise in several forms. The most common spurious states are those stable states that are not originally stored. In terms of phase-space terminology, these are false attractors trapped in the local minima in the energy landscape. Further, Montgomery *et. al.* pointed out the existence of oscillating states that also affect the storage capacity.[5.10]

To increase the storage capacity of the neural network associative memory, we must reduce or eliminate the spurious states. There are a number of modifications of the prototype. For example, the sparsely encoded associative memory,[5.11] the chaos associative memory[5.12] and so on. For the purpose of reducing the trap with states in local energy minima of the phase space, i.e., the spurious states, statistical mechanical models such as simulated annealing[5.13]

have been proposed to permit uphill jumps in the phase space so that the state of the network can be pumped out of the local minima and eventually reaches the global minimum. Recently, Morita has shown that the performance of the conventional associative memory model is improved remarkably by a partial reverse method in recalling process.[5.14] One remarkable fact is that the absolute capacity is about $0.4N$,[5.15] which is much greater than the absolute capacity $N/(4\log N)$ of the conventional Hopfield model and is larger than even the relative capacity $0.15N$. The other point is the disappearance of the spurious memory. But it still remain some problems such as venerable mathematical analysis. On the other hand, a new type of attractor called a terminal attractor (TA),[5.16] which represents singular solutions of a neural dynamic system, was introduced for the elimination of the spurious states in the associative memory. These terminal attractors are characterized by having finite relaxation times, no spurious states, and infinite stability. The applications of terminal attractors for content-addressable and associative memories, pattern recognition, self-organization, and for dynamical training have been illustrated. An application of the TA model for pattern recognition in a neural network is described in the following section.

5.2 DYNAMICS OF TA MODEL

5.2.1 Basic TA Model

The idea of the TA is based on a violation of the Lipschitz condition* at a fixed point. As a result, the fixed point becomes a singular solution which envelopes the family of regular solutions, while each regular solution approaches such an attractor in finite time, no spurious state, and infinite stability.

---

* For a dynamics system $\dot{x} = f_i(x_1, x_2, \ldots, x_n)$, $i = 1,2,\ldots,n$, the Lipschitz condition is defined by $|\partial f_i / \partial x_i| < \infty$.

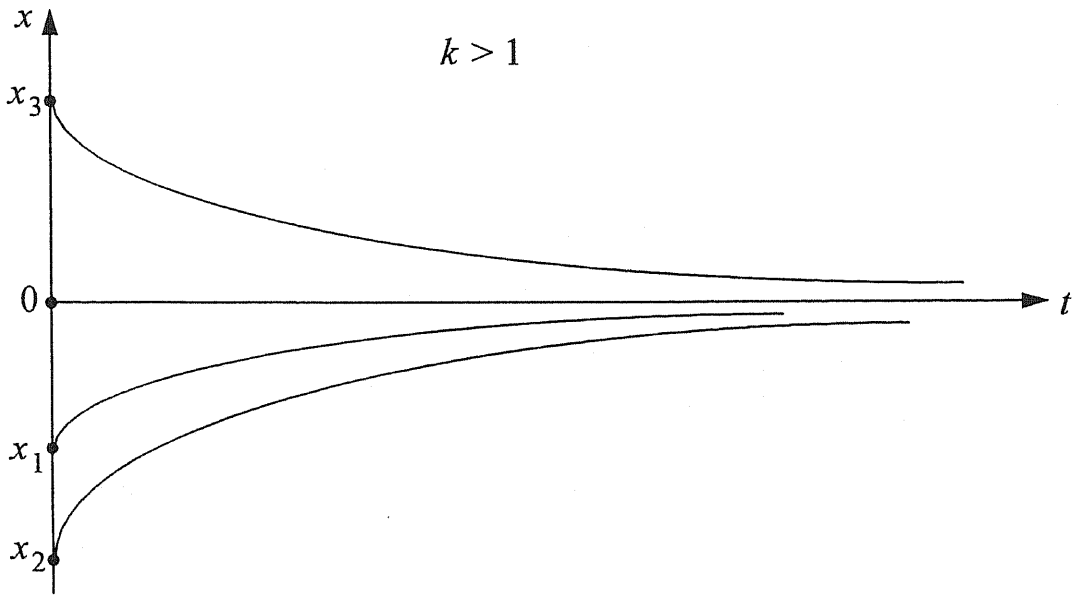

(a)

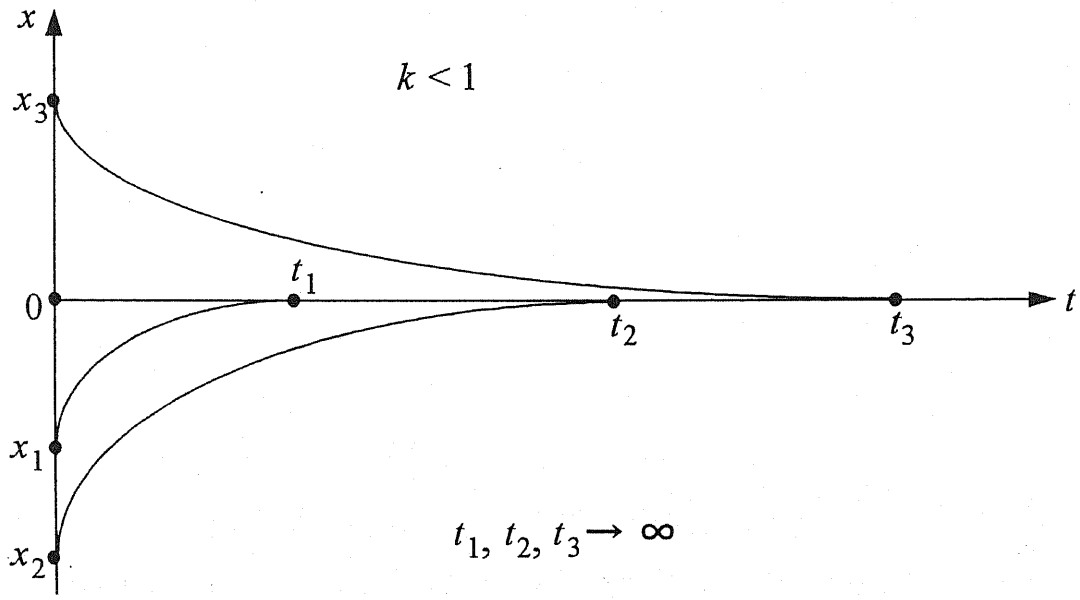

(b)

Fig. 5.2 Convergence to (a) regular attractor and (b) terminal attractor.

Let us consider a dynamics system, which is given by the following differential equation

$$\dot{x} = -x^k, \tag{5.8}$$

where k is a positive parameter. This equation has an equilibrium point at $x = 0$. Then, let us consider the Lipschitz condition in the neighborhood of the equilibrium point $x = 0$ as

$$\lim_{x \to 0} \frac{d\dot{x}}{dx} = -k \lim_{x \to 0} x^{k-1} = \begin{cases} 0 & k > 1 \\ -\infty & 0 < k < 1. \end{cases} \tag{5.9}$$

Namely, if $k > 1$, the dynamics system of Eq. (5.8) satisfy Lipschitz condition and has a regular attractor. In contrast, if $k < 1$ ($k = 1/3, 1/5, \ldots, 1/(2n+1)$), then, the Lipschitz condition is violated and the system has a terminal attractor.

The relaxation time t_i is plotted versus the initial values of $x = x_i$ and is shown in Fig. 5.2 for both the regular and the terminal attractors. It is clear that the relaxation time approaches infinity for the regular attractors, meaning that x never intersects the solution $x = 0$. In contrast, for the terminal attractors, $x(t = 0) = x_1$ decays to $x = 0$ at $t = t_1$, $x(t = 0) = x_2$ decays to $x = 0$ at $t = t_2$, and so on, all in finite times. Consequently, these attractors become terminal. It represents a singular solution which is intersected by all the attracted transients.

5.2.2 TA Model for Associative Memory

First, let us consider a discrete time type of neural networks consisting of N neurons with outputs bipolar values. At time t, the output of the ith neuron is $x_i(t)$. Then, we assume that a set of N linearly independent vectors $\{x_i^{(m)}\}$ $(m = 1, 2, \ldots, M)$ is stored as terminal attractors in the neural network. The neural dynamics of the TA model for associative memory are given by

$$\frac{dx_i(t)}{dt} + x_i(t) = \sum_{j=1}^{N} W_{ij} f\left[x_j(t)\right] - \sum_{m=1}^{M} \alpha^{(m)} \left\{ f\left[x_i(t)\right] - x_i^{(m)} \right\}^{\frac{1}{3}} \times \exp\left\{ -\beta^{(m)} \left\{ f\left[x_i(t)\right] - x_i^{(m)} \right\}^2 \right\}, \tag{5.10}$$

where N and M are the total numbers of neurons and stored patterns in the network, $\alpha^{(m)}$ and $\beta^{(m)}$ are positive control constants, and W_{ij} is a connection weight from the jth neuron to the ith one. The exponential multipliers are introduced into Eq. (5.10) in order to localize the effects of the terminal attractors and to provide a Gaussian distribution peaked at $f\left[x_i(t)\right] = x_i^{(m)}$. When $f\left[x_i(t)\right]$ moves away from $x_i^{(m)}$, the exponential function decays to zero. This term maximizes the influence of the terminal attractor for $f\left[x_i(t)\right]$ that approaches $x_i^{(m)}$. $f[\cdot]$ is a output threshold function

$$f\left[x_i(t)\right] = \tanh\left[x_i(t)\right]. \tag{5.11}$$

That is, the network changes its state at discrete times $t = 0,1,2,\ldots$ according to Eqs. (5.10) and (5.11). Here, the threshold function tanh operates componentwise on vectors.

5.2.3 Linearly Stability of TA Model

Before the stability of the equilibrium point $x_i^{(m)}$ of Eq. (5.10) is discussed, the stability of equilibrium points of a dynamics system should be reviewed briefly. Let us consider a dynamics system with equilibrium points x^*

$$\frac{dx_i}{dt} = f_i(x_1,\ldots,x_n) \quad (i = 1,2,\ldots,n). \tag{5.12}$$

We have the theorem of the stability of a dynamics system, i.e., if the real parts of the eigenvalues of the Jacobi matrix which the linearized version of the dynamical system (5.12) in

the neighborhoods of the corresponding equilibrium point

$$J(x^*) = \begin{pmatrix} \frac{\partial f_1}{\partial x_1}(x^*) & \cdots & \frac{\partial f_1}{\partial x_n}(x^*) \\ \vdots & \ddots & \vdots \\ \frac{\partial f_n}{\partial x_1}(x^*) & \cdots & \frac{\partial f_n}{\partial x_n}(x^*) \end{pmatrix}, \tag{5.13}$$

are all negative, that is,

$$\mathrm{Re}\,\lambda_i < 0, \tag{5.14}$$

then these point are asymptotically stable.[5.17] Such points are called static attractors, since each solution that gets close enough to x^* approaches the corresponding constant value as a limit as $t \to \infty$, i.e., it enters a basin of attraction that the size is an index of the recollection ability of the neural network dynamics system.

Based upon the above theorem, let us linearize the Eq. (5.10) in the neighborhoods of the equilibrium point $x_i^{(m)}$, and with respect to point $f[x_i(t)]$ which are sufficiently close to the equilibrium points $x_i^{(m)}$, so that

$$\left| f[x_i(t)] - x_i^{(m)} \right| = \varepsilon \to 0. \tag{5.15}$$

Fro a simple description, we will assume $M = N$ in Eq. (5.10). It is reasonable because of the stability of the dynamics is not affected. Then, the linearized version of the Eq. (5.10) in the neighborhoods of the corresponding equilibrium point is written by

$$\frac{dx_i(t)}{dt} = \sum_{j=1}^{N} J\left(x_j^{(m)}\right)\left\{ f[x_j(t)] - x_j^{(m)} \right\}, \tag{5.16}$$

where $J(x_i^{(m)})$ is the Jacobi matrix of Eq. (5.10) in the equilibrium points $x_i^{(m)}$. It can be obtained by a first order approximation of a Taylor-series expansion. The stability of the equilibrium points $x_i^{(m)}$ depends on the eigenvalues λ_m of the matrix $J(x_i^{(m)})$. Here, all the eigenvalues of the matrix $J(x_i^{(m)})$ are negative and unbounded at the equilibrium points $x_i^{(m)}$, which means that all these equilibrium points satisfy the condition Eq. (5.14) and they are terminal attractors of infinity stability. For proof, see Appendix C.

Thus, by incorporating with terminal attractors in a neural network consisting of N neurons, one can store N desired vectors as stable equilibrium points with no spurious static attractors. Hence, Eqs.(5.10) and (5.11) can be used as an associative memory for pattern recognition.

5.3 COMPUTER SIMULATIONS OF TA MODEL

5.3.1 Simulation Method

In order to demonstrate the effectiveness of the TA model associative memory for pattern recognition, we use the computer simulations. The assumptions will be required for the TA dynamics system of Eq. (5.10) before the simulations. These assumptions are related to the selection of the values of $\dot{x}_i(t)$, W_{ij}, $\alpha^{(m)}$, and $\beta^{(m)}$. At first, it is assumed that the neural network which was given by dynamics system of Eq. (5.10) is a discrete in time, then, $\dot{x}_i(t) = 0$, namely, it reaches a steady state from a initial state. Next, we discuss the connection weight W_{ij}. The simplest assumption is that W_{ij} may be determined by the Hebb's law in the same way as the Hopfield model (see Eqs. (5.2) and (5.3)). When this term was used in the Hopfield model, spurious states were found. There are several possible ways to make the interconnection weight W_{ij} in the TA model. The choice of another interconnection weight may cause unequal comparison between the two models. For the sake of the comparison of the effects of the reduction for spurious states in the TA model on the same basis and to see

whether the TA term can improve the storage and retrieval capabilities of the neural network system, the same connection weight is used for the both networks. Finally, we discuss the parameters $\alpha^{(m)}$ and $\beta^{(m)}$. The parameter $\alpha^{(m)}$ is the measure of the correction by the TA model. If this value is too small, then the effect of the correction for the Hopfield model becomes small and the solution by the recalling may be trapped by spurious states originally involved in the Hopfield dynamics. For a large value of $\alpha^{(m)}$, the correction by the second term of the right hand side of Eq. (5.10) becomes large and the memory stored in the Hopfield may not be recovered. Then we choose this value as unity for all m from the empirical basis of the simulations. As already mentioned, the purpose of $\beta^{(m)}$ in the terminal attractor is to provide a Gaussian distribution peaked at $f(x_i) = x_i^{(m)}$. In practice, the values of $\beta^{(m)}$ controls the influence that a stored pattern has on its neighbor (in terms of Hamming distance). A small $\beta^{(m)}$ (for instance, $\beta^{(m)} < 0.5$) causes stronger cross talk among stored patterns, and the spurious states caused by cross talks are generated near the boundary of a basin of a stored pattern. Whereas, a large $\beta^{(m)}$ reduces the cross talks. In other words, the value of $\beta^{(m)}$ decides the behavior of neighbors of a terminal attractor. However, the optimal value of $\beta^{(m)}$ is not theoretically obtained. According to the experience, the good results are obtained when $\beta^{(m)}$ is about 1~3. For simplicity, we select $\beta^{(m)} = \alpha^{(m)} = 1$ in our simulations and the later optical experiment. With these selections of parameter values, Eq. (5.10) may be written as

$$x_i(t) = \sum_{j=1}^{N} W_{ij} f\left[x_j(t)\right] - \sum_{m=1}^{M} \left\{ f\left[x_i(t)\right] - x_i^{(m)} \right\}^{\frac{1}{3}} \times \exp\left\{ -\left\{ f\left[x_i(t)\right] - x_i^{(m)} \right\}^2 \right\}. \qquad (5.17)$$

The computer simulations have been performed by using a 6×6 neuron network based on the Eqs. (5.17) and (5.11). The network is trained to recognize the patterns "A", "O", "E", as shown in Fig. 5.3. These patterns are stored as terminal attractors in the network. Their Hamming distances from each pattern are tabulated in Table 5.1. The mean Hamming distance among the three patterns is 14.67.

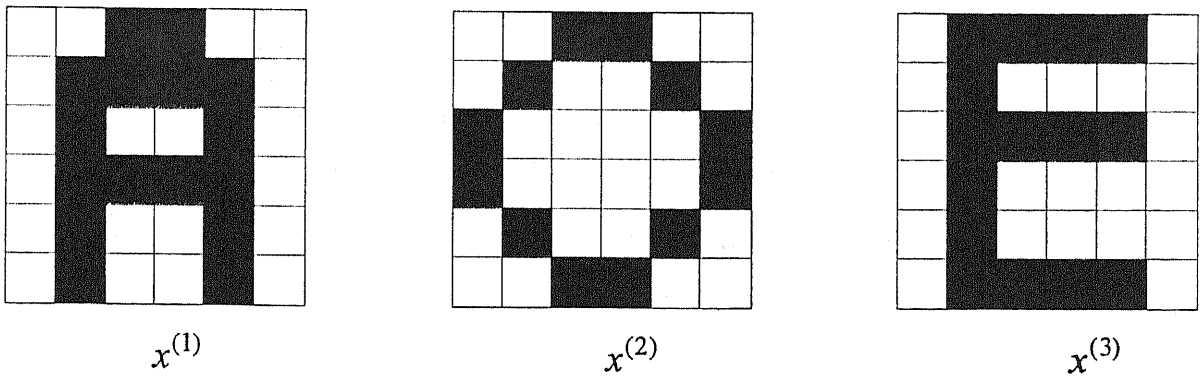

Fig. 5.3 Stored patterns in the computer simulations.

Table 5.1 Hamming distances among stored patterns.

PATTERN	$x^{(1)}$	$x^{(2)}$	$x^{(3)}$
$x^{(1)}$	0	16	13
$x^{(2)}$	16	0	15
$x^{(3)}$	13	15	0

5.3.2 Results and Discussion

The computer simulation results of the recognition ability for the Hopfield and the TA ($\beta^{(m)}$ = 0.2 and 1) neural network associative memories are shown in Figs. 5.4, 5.5, and 5.6, respectively. The Hamming distances of six initial imperfect inputs from stored pattern "A"

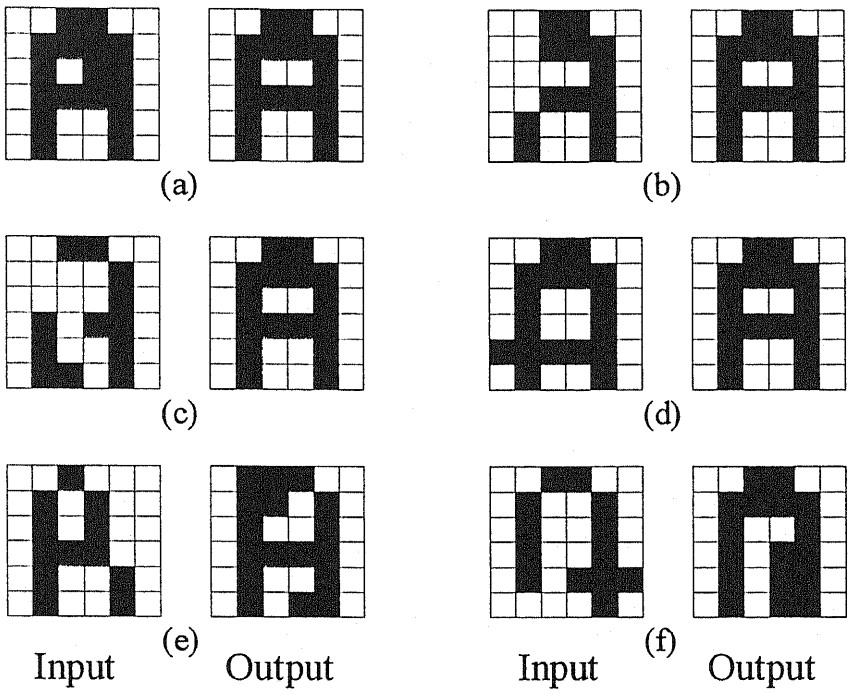

Fig. 5.4 Computer simulations for the recalling property of the Hopfield model.

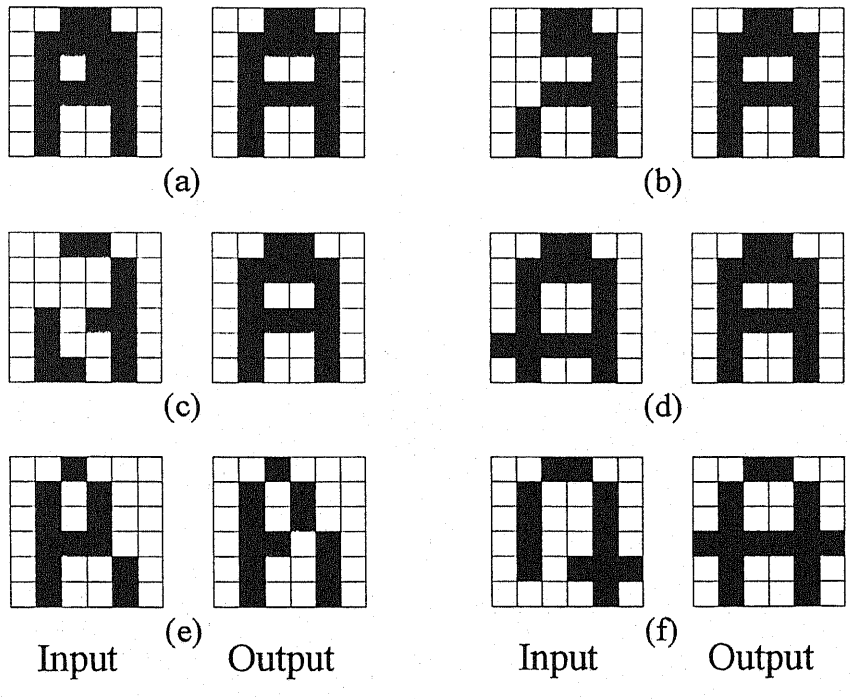

Fig. 5.5 Computer simulations for the recalling property of the TA model ($\beta^{(m)} = 0.2$).

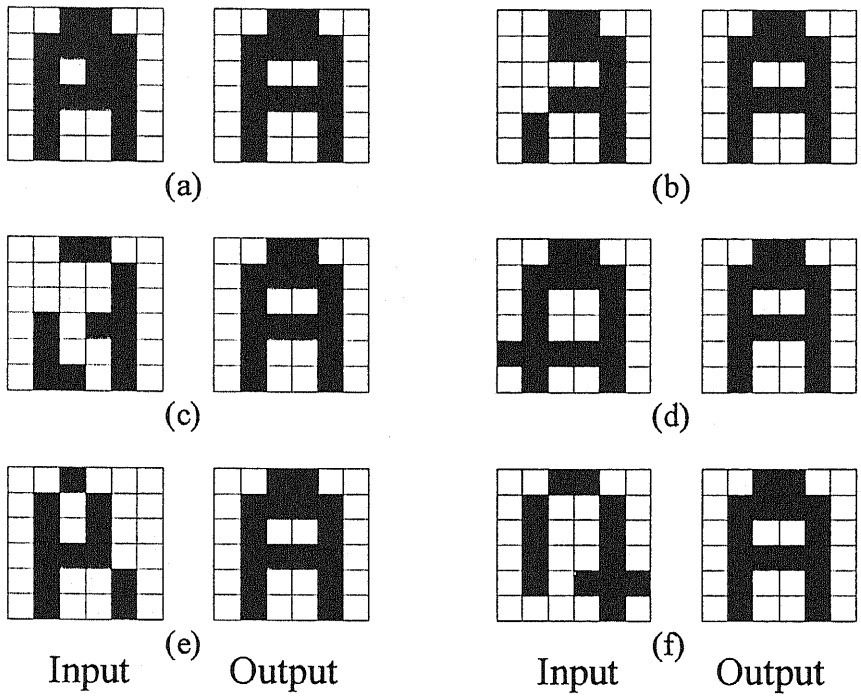

Fig. 5.6 Computer simulations for the recalling property of the TA model ($\beta^{(m)} = 1$).

are 1, 3, 4, 5, 6, and 7, respectively, and those for the other stored patterns are equal to 11 or more. From Figs. 5.4, 5.5 and 5.6, we can see the following facts:

1. The neural networks both in the TA and Hopfield models are correctly converged to pattern "A" without trapping in local minima when starting from the imperfect patterns for a smaller Hamming distance (see Figs. 5.4, 5.5 and 5.6 (a)-(d)). This means that the pattern recognition ability of the two model is almost the same for this case.

2. When the Hamming distance between the initial input and the stored pattern becomes large (see Figs. 5.4, 5.5 and 5.6 (e)-(f)), the Hopfield model converges to the error patterns, i.e., the local minima. In the TA model, when $\beta^{(m)} = 0.2(<0.5)$, the spurious states caused by cross talks are generated. The associations are also failed. On the contrary, when $\beta^{(m)} = 1$ for the TA model, the spurious state does not exist and the system always converges to a global minimum which corresponded to the right stored pattern. Namely, the TA neural network associative memory can reduce spurious states in the Hopfield model and improve its recollection ability.

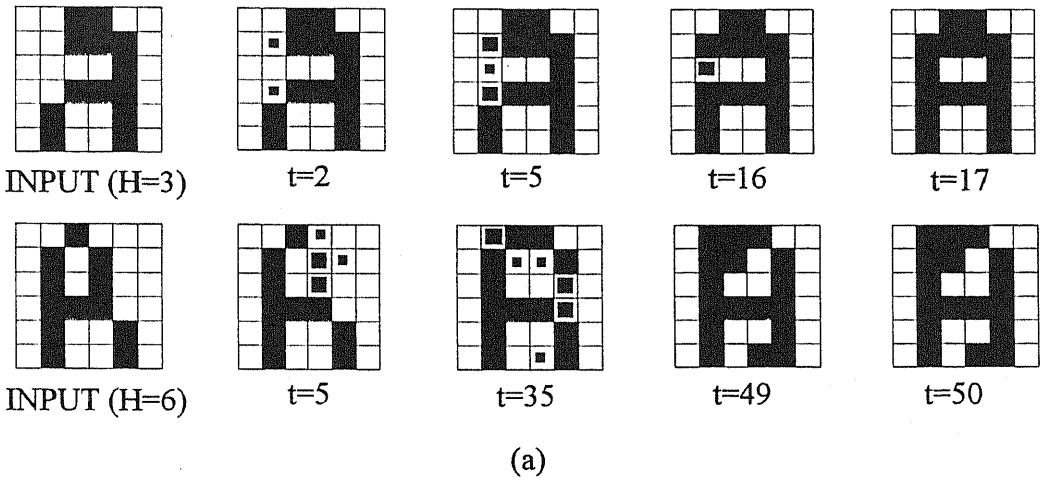

(a)

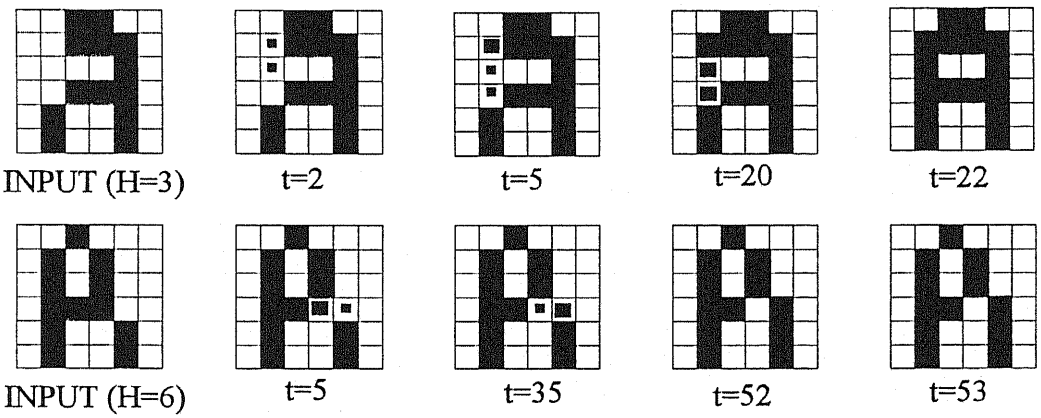

(b)

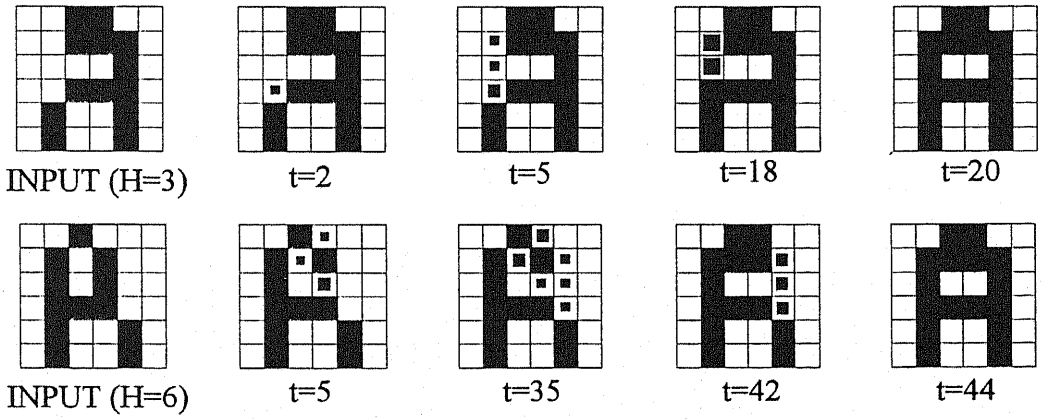

(c)

Fig. 5.7 Examples of the recognition process in (a) the Hopfield model, (b) the TA model ($\beta^{(m)} = 0.2$), and (c) the TA model ($\beta^{(m)} = 1$). Hamming distances of the inputs from the pattern "A" are H=3 and H=6. t is the iteration time.

Figure 5.7 shows some instant states in the evolutions of the neural networks. The networks correctly converged to "A" starting from an imperfect version up to a Hamming distance of 3 in the both models. Besides the convergence is better in the Hopfield model. But, when starting from a Hamming distance of 6, the neural network state of the Hopfield model converges to an equilibrium state which is very different from the stored patterns, i.e., a spurious memory is recalled as shown in Fig. 5.7 (a). The recognition is also unsuccessful in the TA model of $\beta^{(m)} = 0.2$ as shown in Fig. 5.7 (b), while the TA model with $\beta^{(m)} = 1$ in Fig. 5.7 (c) succeeds the correct recalling.

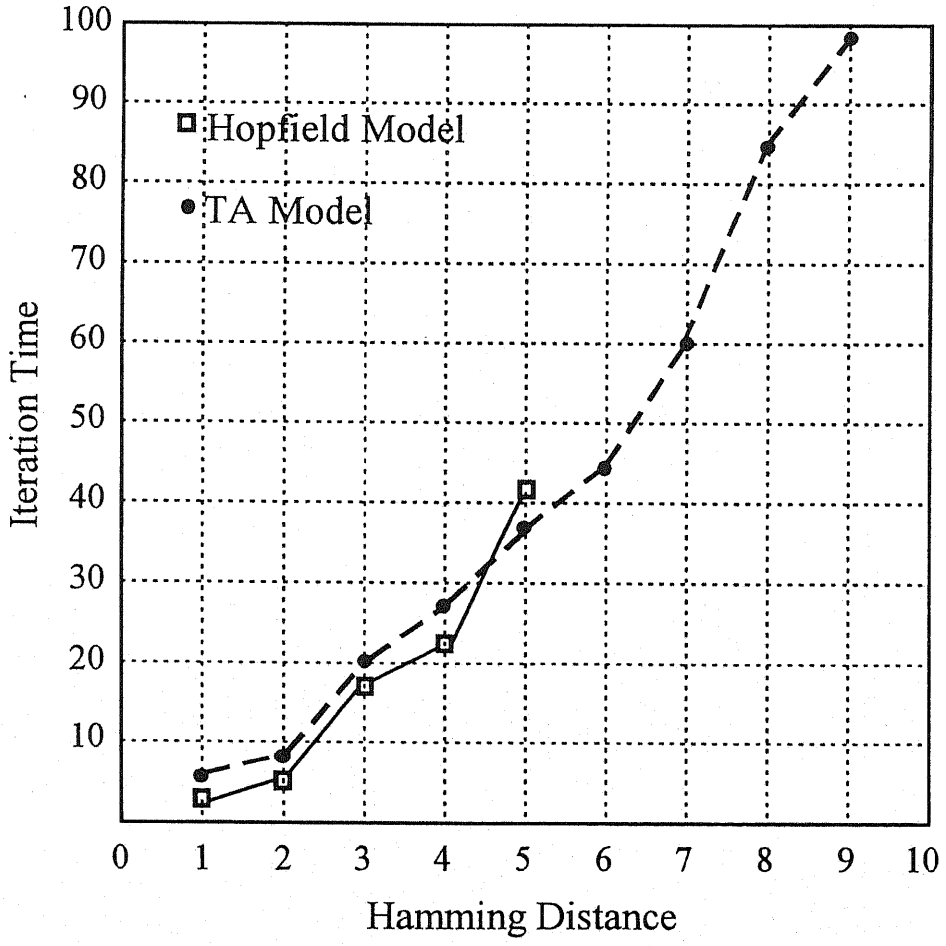

Fig. 5.8 Dependence of the iteration time for the correct recalling on the Hamming distance.

In the neural network for pattern recognition, the speed of correct recalling and the recognition rate are the measures which show the ability of the network system. Therefore, the recognition speed and recognition rate for the used Hopfield and TA ($\beta^{(m)} = 1$) neural networks are considered.

At first, we discuss the speed of the correct recalling. To express the dependence of the iteration time for the correct recalling on the Hamming distance clearly, the iteration time versus the Hamming distance is plotted in Fig. 5.8. Figure 5.8 shows how the iteration time changes with the Hamming distance for the recalling process. We can see that the Hopfield model has faster speed of the convergence up to the Hamming distance of 4 because of the simplicity of its structure. But, for the Hamming distance equal to 5 or more, the correct pattern can not be recalled any more in the Hopfield model. On the contrary, a stable association characteristic is shown for a larger Hamming distance in the TA model, though the iteration time increases.

Next, we discuss the recognition rate. Figure 5.9 shows the plot of the recognition rate against the Hamming distance from the memory pattern. The ordinate of the graph is the recognition rate and the abscissa is the Hamming distance, where recognition rate is defined by

$$\text{recognition rate} = \frac{\text{total number of patterns of successful recollection}}{\text{total number of input patterns}} \times 100\%.$$

The recognition rate may depend on what kinds of patterns are stored as memory patterns and also on a set of input test patterns. Although the absolute value of the recognition rate plotted here does not have absolute meaning, the trend of the recalling for the system can be evaluated by such a plot.

In this computer simulation, the total number of test patterns is 15 corresponding to each Hamming distance. From the results that shown in Fig. 5.9, the TA model maintains the recognition rate of more than 70% up to the Hamming distance of 7. It is possible to say that the TA model has a good pattern recognition ability.

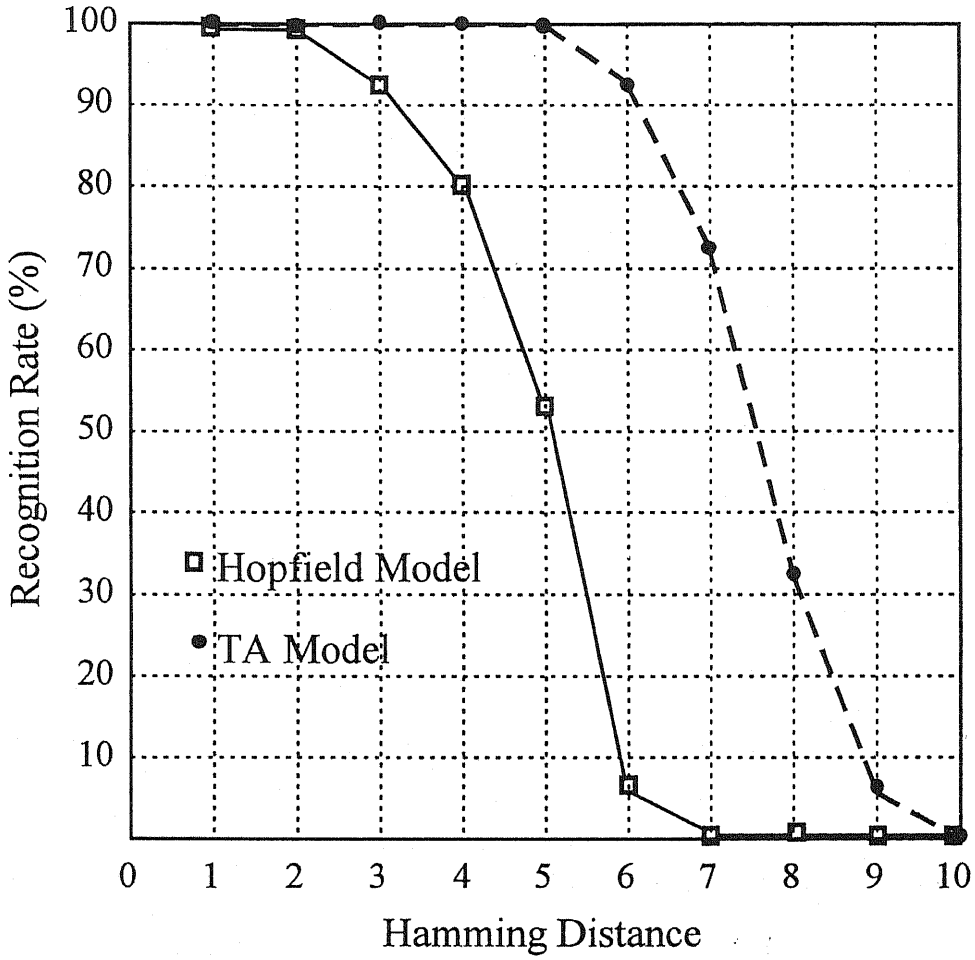

Fig. 5.9 Recognition rate against the Hamming distance from the memory pattern. Total number of test patterns for each Hamming distance is 15.

5.4 OPTICAL IMPLEMENTATION OF TA MODEL

Optical technologies offer parallel processing and two-dimensional interconnections. Therefore, optical neural network have received considerable attentions for their applications to information storage and processing.[5.18-21] The principal challenge of optics has always been overcome by the lack of devices to implement the reprogrammable operations required in

information processing. Recent advances in SLMs offer new alternatives for optical neural architectures. In this section, we present an optical implementation of the TA model associative memory for pattern recognition.

5.4.1 Experimental Method

Optical implementation of dynamics system described by Eq. (5.17) is very difficult because it contains a 1/3 power function. For the feasibility of the optical implementation, we make further approximations to Eq. (5.17), since most of optical devices used as a SLM are binary nature. If we assume that the unipolar binary number (1,0) is used for the neuron-state vectors, the factor of 1/3 in the power function of Eq. (5.17) may be dropped and, instead of the square operation in the exponential function, the absolute value function can be used without changing the value of the equation. By using this assumption, Eqs. (5.17) and (5.11) are rewritten as follows:

$$x_i(t) = \sum_{j=1}^{N} W_{ij} f\left[x_j(t)\right] - \sum_{m=1}^{M} \left\{ f\left[x_i(t)\right] - x_i^{(m)} \right\} \times \exp\left\{ -\left| f\left[x_i(t)\right] - x_i^{(m)} \right| \right\}, \tag{5.18}$$

$$f\left[x_j(t)\right] = 1\left[x_i(t)\right], \tag{5.19}$$

where $1[u] = 1$ when $u > 0$ and -1 when $u < 0$.

The optical neural network architecture for pattern recognition based on the TA model described by Eqs. (5.18) and (5.19) is shown in Fig. 5.10. It consists of two subsystems. One is the optical system for the Hopfield model and the other is the optical system which realizes the TA model. In the Hopfield model subsystem, two liquid-crystal televisions LCTV1 and LCTV2 which consist of 220×320 pixels, each size of $80\mu m \times 90\mu m$, are used as the SLMs to represent the state vector $f(x_i)$ ($i = 0,1,2,\ldots,N$) and the connection matrix W_{ij}

($i, j = 1,2,\ldots,N$), respectively. Here, N is the number of neurons in the network. The results of the Hopfield model outputs are detected by the CCD camera 1.

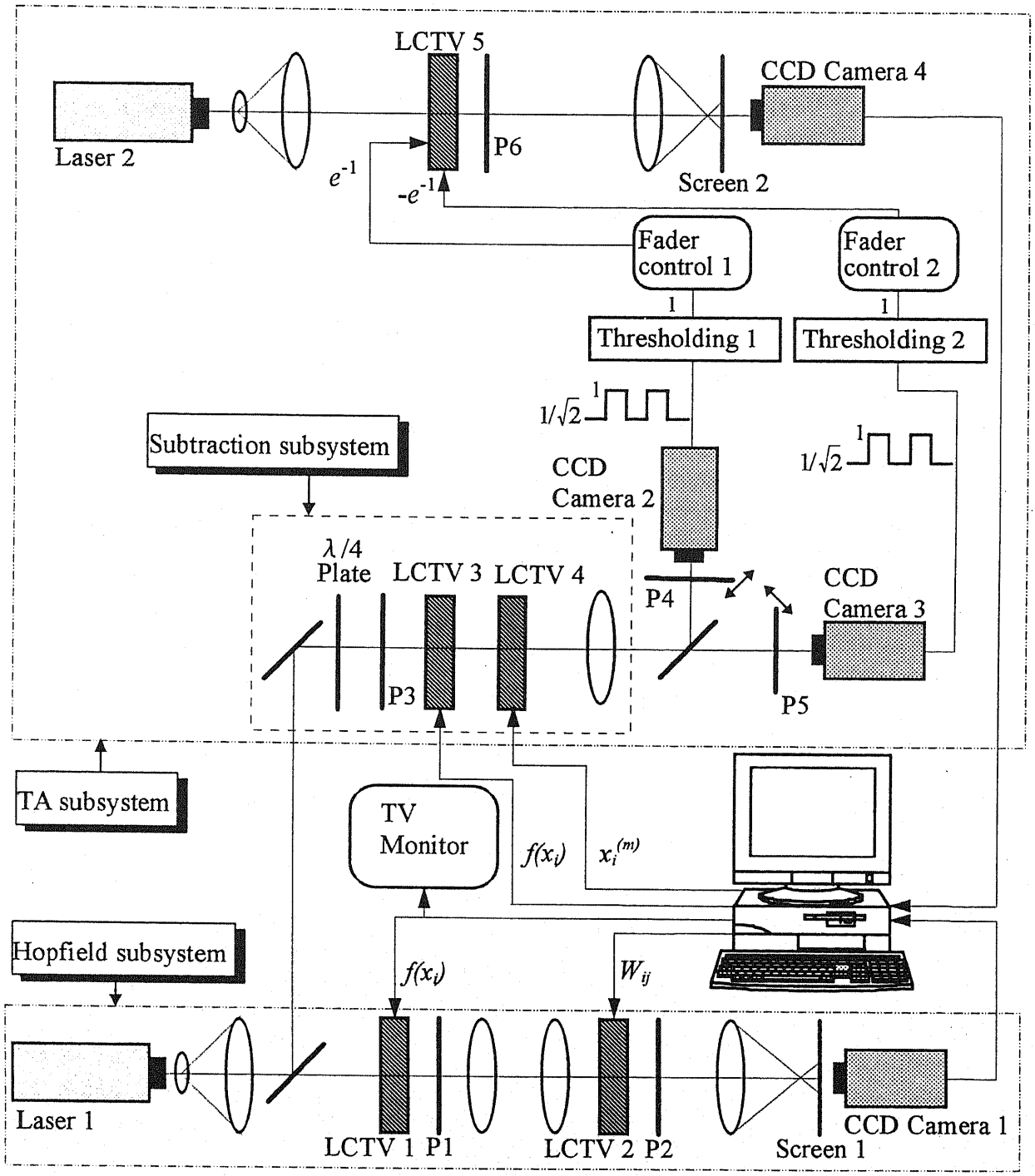

Fig. 5.10 Experimental setup for the TA model optical associative memory. P1-P6: polarizers.

The TA subsystem has two challenging problems. The first is the optical implementation of the subtraction. The second is the realization of the exponential weight. From an optics point of view, the exponential operation and the subtraction shown in the Eq. (5.18) are not easy to implement. In the optoelectronics approach, these two operations can best be handled by electronics. But the operation is much faster if it can be done optically in parallel and real-time.

Here, for the implementation of the subtraction $f(x_i) - x_i^{(m)}$, we used a real-time image subtraction system by using polarization modulation of LCTV.[5.22] The LCTV-SLM not only has the intensity modulation property, but also has the attractive features of polarization and phase modulations of light. The principle of the image subtraction that is based on polarization modulation is as follows. It is assumed that only the direction of the linear polarization through the LCTV is changed by applying the voltage to the LCTV and that the state of the linear polarization remains approximately unchanged, so that the real-time image subtraction is accomplished by the approximate rotations of the linear polarization of successive light transmissions through LCTV3 and 4, where the twist direction of the liquid crystal molecules of the LCTV3 is reversed to that of the LCTV4. The intensity difference of two images that corresponds to the polarization angle difference is detected. The sign of the subtraction is obtained by the polarization direction of light. In the experiment, the polarization modulation angles that corresponds to the binary input signals 0 and 1 are 0° and 45°, respectively. The results of four possible output subtractions are tabulated in Table 5.2. Using two polarizers P4 and P5 that have the polarization directions ±45°, we obtain the results ±1 for the output polarizations of ±45° and $\pm 1/\sqrt{2}$ of the unwanted signals for the output polarization of 0°. They are detected by the CCD camera 2 and 3. After thresholding, we obtain only the correct results that correspond to ±1 signals.

The exponential operation can simply let the digital computer handle the job. However, the optical method was used in this experiment. It is realized by the optical subsystem that has the light transmission property equal to the value of exponential function,

Table 5.2 Subtraction results in the experiment

Subtraction	Result	Output Polarization
1 - 1 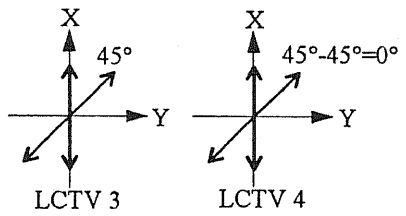	0	 (0°)
0 - 0 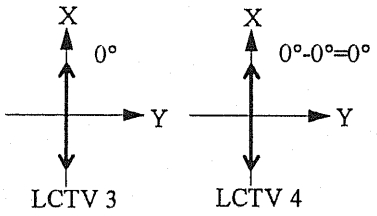	0	 (0°)
1 - 0 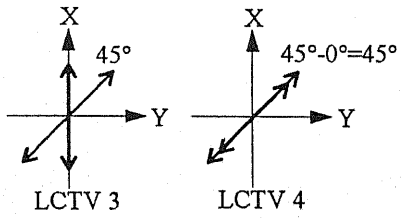	1	 (+45°)
0 - 1 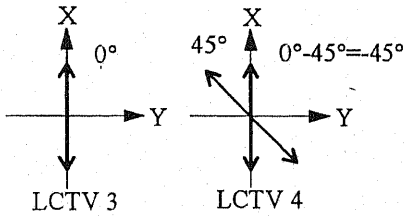	-1	 (-45°)

i.e., a fader control is used. Finally, the summation with respect to M is calculated and casted in the Screen 2, and is detected by the CCD camera 4 as the output of the TA model subsystem.

The signals of the TA model subsystem which is the output from the CCD camera 4 and the Hopfield model subsystem which is the output from the CCD camera 1 are sent to a computer to the subtraction of the two terms with an analogue quantity. After thresholding, we obtain the next state $x_i(t+1)$. The update state vector $x_i(t+1)$ is the input as a new state to LCTV-SLMs for the dynamical system. The above process is iterated until the state vector converges to a stable state without trapping in local minima. The converged stable state is displayed on a TV monitor. The subtraction of the analogue quantity here was calculated by the digital computer due to the accuracy problems of the optical subtraction, but it can be calculated optically, such as for example by the same principle of the polarization modulation by LCTV-SLMs used in the TA subsystem.

5.4.2 Results and Discussion

In the experiments, we used a network with N=4×4 neurons. The network was trained to recognize the patterns "A", "O", "H". Figure 5.11 shows examples of the experimental results of the recovery from imperfect inputs by the optical setup in Fig. 5.10. Three stored patterns are shown in Fig. 5.11 (a). The mean Hamming distance from other patterns is 8. Figure 5.11 (b) shows four initial imperfect patterns. The Hamming distances of the inputs from the stored pattern "A" are 1, 2, 3, and 4 from top to bottom, respectively, and those with the other stored patterns are equal to 5 or more. The Hamming distances of the input patterns from the memory patterns are tabulated in Table 5.3. The results for the pattern recognition in the Hopfield and TA models are shown in Figs. 5.11 (c) and (d), respectively. These results indicate that the recognition is unsuccessful due to the trap in a local minimum in the Hopfield model neural network when the Hamming distance between the initial input and the stored pattern is 3 or more. On the contrary, the TA model network correctly converges to "A", thus the association

is successful for all input data.

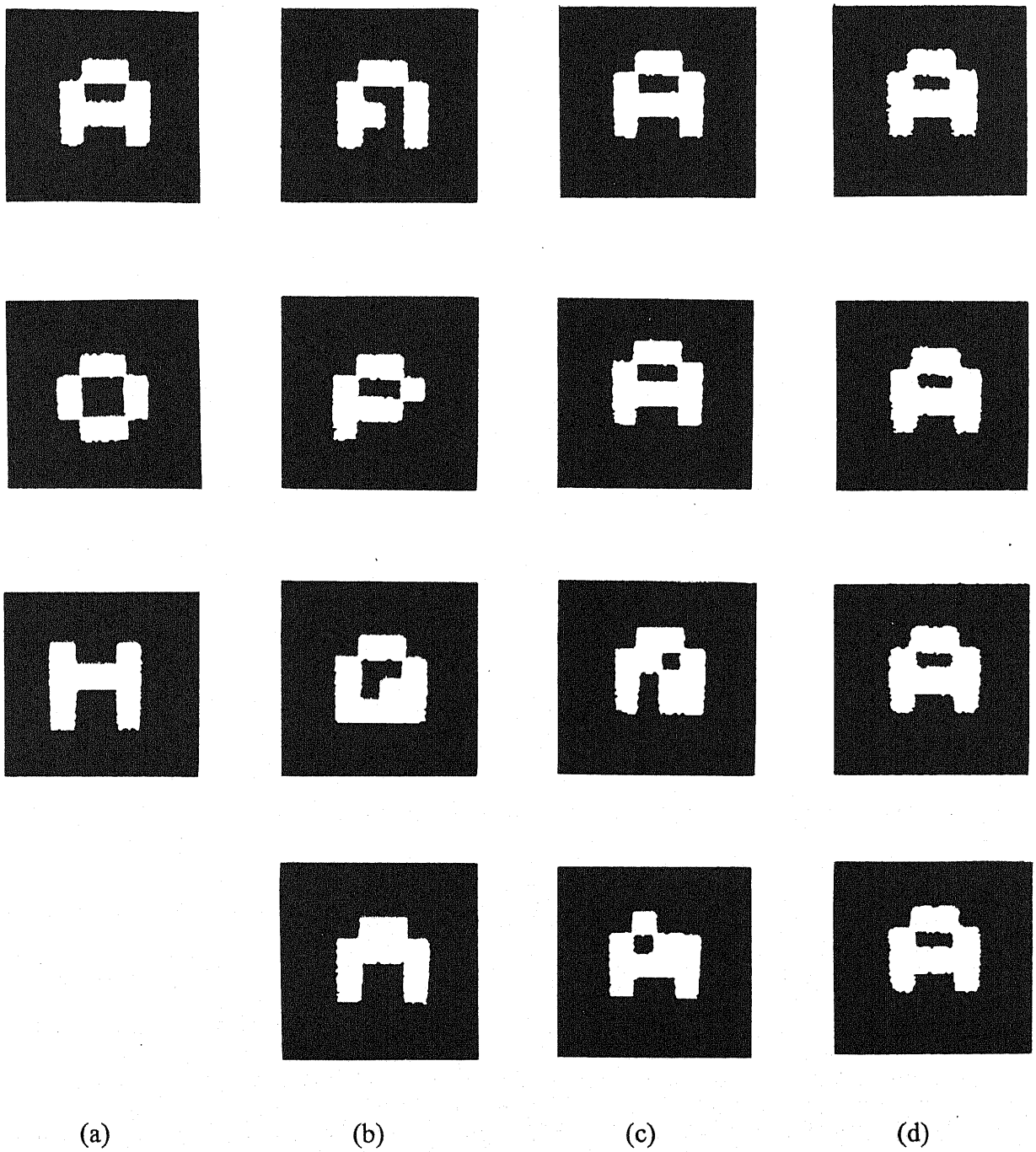

Fig. 5.11 Experiment results. (a) Stored patterns, (b) inputs, (c) outputs of the Hopfield model, and (d) outputs of the TA model.

Table 5.3 Hamming distance of input patterns from the memory patterns.

INPUT PATTERN	MEMORY PATTERN		
	$x^{(1)}$	$x^{(2)}$	$x^{(3)}$
X_1	1	5	7
X_2	2	6	10
X_3	3	7	11
X_4	4	6	12

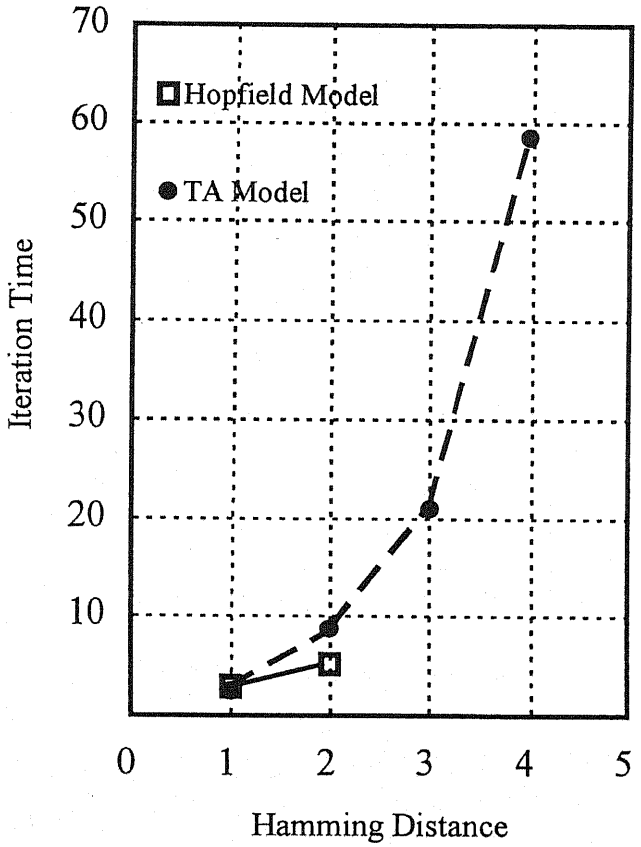

Fig. 5.12 Dependence of the iteration time for the correct recalling on the Hamming distance.

From the experiment results, we plot a graph to express the dependence of the iteration time for the correct recalling on the Hamming distance. Figure 5.12 indicates that the stable association state is realized up to the Hamming distance of 4 in the used TA model network system. One the other hand, the Hopfield model network has faster recollection speed when the Hamming distance is 2 or less. But, when the Hamming distance is greater than 2, the recalling ability of the Hopfield model deteriorates suddenly. These results are same with the computer simulation.

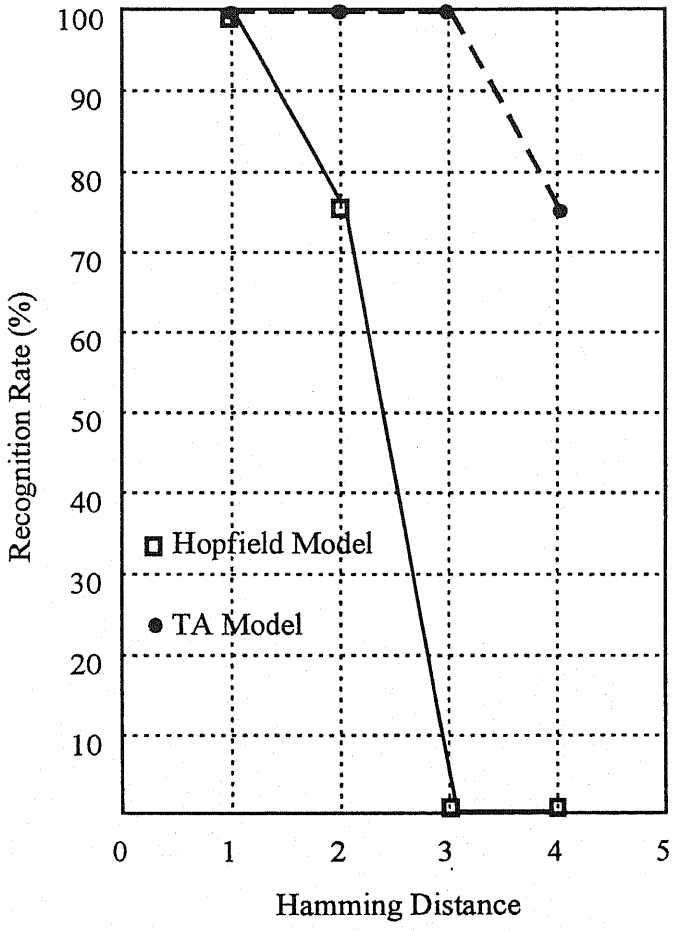

Fig. 5.13 Recognition rate against the Hamming distance from the memory pattern. Total number of test patterns for each Hamming distance is 4.

The results of the recognition rate for the optical system in Fig. 5.10 are shown in Fig. 5.13. In the experiment, the total number of test patterns for each Hamming distance is 4. The TA model has the pattern recognition rate of more than 75% up to Hamming distance of 4. The achievement and correct pattern recognition in the TA model neural network is demonstrated by the optical experiment.

5.5 INVESTIGATION OF CAPACITY FOR TA MODEL

As already mentioned in Section 5.1.3, the storage capacity of the Hopfield model is quite limited because of the number of spurious states and oscillations. The investigation reveals that its absolute memory capacity of $N/(4\log N)$ is much smaller than N in order and its estimated relative memory capacity of $0.15N$ is not large. On the other hand, the TA model neural network is expected to have no spurious states, infinite stability, and the improvement of the memory capacity. However, the memory capacity of the TA model can not be given because it is influenced by the various conditions, so that both the mathematical analysis and the experimental demonstration are difficult. We will give a rather intuitive explanation by a numerical simulation instead.

The numerical simulation have been performed by using a 100 neuron network model. The Hamming distance between inputs and the stored pattern is greater than 5. The memory rate is defined by

$$r_t = \frac{M}{N} . \tag{5.20}$$

Figure 5.14 shows the relation between the memory rate and the consistency of the recalling by the numerical simulation. These results indicate that, by the TA model associative memory, the conventional Hopfield model is greatly improved by the introduction of the terminal attractor in the memory capacity.

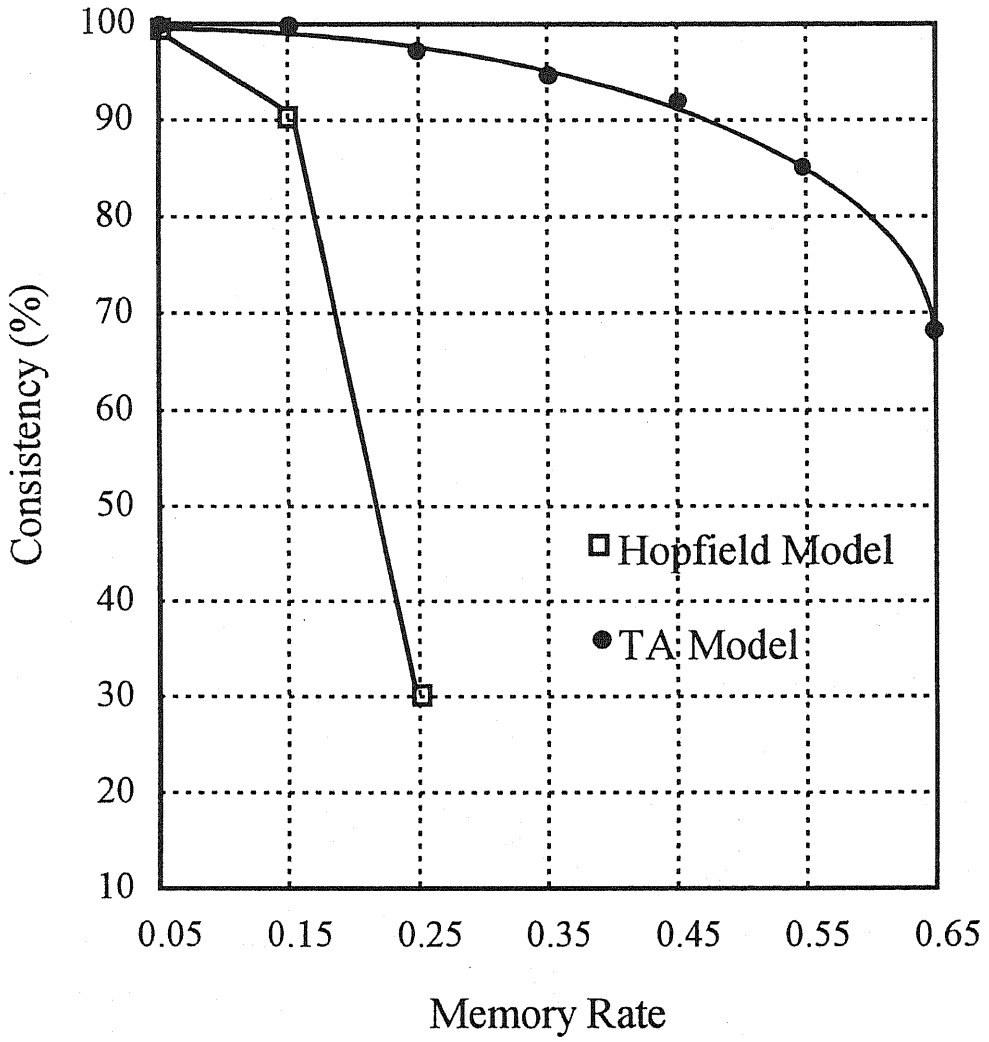

Fig. 5.14 The relation between the memory rate and the consistency of the recalling.

5.6 SUMMARY

In this chapter, we have applied the TA model neural network for pattern recognition and compared it with the conventional Hopfield model. The computer simulations for the pattern recognition ability have been performed by using a 6×6 neuron network model. Patterns "A", "O", and "E" were embedded in the network as the recognition target patterns and we have

shown the usefulness of the TA neural network. Furthermore, for discussing the feasibility of the optical implementation of the TA model associative memory, we have used a network with 4×4 neuron and 3 stored patterns "A", "O", and "H". The TA model optical neural network for pattern recognition was carried out by using LCTV-SLMs and CCD cameras. We have successfully realized the exponential and subtraction computations for the TA model dynamics by the optical method. From the experimental results, it is possible to construct all-optic TA neural network by using currently available optical devices and a large scale neural network can be realized. The experimental results indicate that the TA model can reduce spurious states in the Hopfield model neural network without trapping in local minima. We have also shown that, by TA model dynamics, the Hopfield model is greatly improved in terms of recollection ability and memory capacity.

We have used LCTV-SLMs in the optical experiments which are operated by TV frame rate, so that the state-update time of this neural network is primarily limited by the speed of the TV frame rate. The main drawback of LCTV-SLM is its limited dynamic range and contrast ratio. As another optical device, FLC-SLMs present some characteristics that make them attractive for the optical implementation of neural networks[5.23]: high response speed and bistability, intrinsic memory capability, and more important than that, the real-time updating of connections, as stated here, open the possibility of simulating the behavior of biological networks in a practical way. The FLC-SLM is a very attractive and promising device for optical neural network, therefore, further functional optical neural networks may be implemented by the combination of electronically addressed LCTV-SLMs and optical addressed FLC-SLMs.

REFERENCES

5.1 P. J. van Heerden, *Appl. Opt.* **2,** 387 (1963).

5.2 H. C. Longuet-Higgins, *Nature* **217,** 104 (1968).

5.3 D. Gabbor, *IBM J. Res. Dev.* **13,** 156 (1969).

5.4 G. J. Dunning , E. Marom, Y. Owechko, and B. H. Soffer, *J. Opt. Soc. Am.* A **2**(13), 48 (1985).

5.5 H. J. Caulfield, *Opt. Commun.* **55,** 80 (1985).

5.6 R. J. Collier, and K. S. Pennington, *Appl. Phys. Lett.* **8,** 44 (1966).

5.7 J. J. Hopfield, *Proc. Natl. Acad. Sci. USA,* **79**, 2254 (1982).

5.8 J. Feinberg, *Opt. Lett.* **5,** 330 (1980).

5.9 R. J. McEliece, E. C. Posner, E. R. Rodemich, and S. S. Venkatesh, *IEEE Trans. Inf. Theory,* **IT-33**, 461 (1987).

5.10 B. L. Montgomery and B.V. K. Vijaya Kumar, *Appl. Opt.* **25,** 3759 (1986).

5.11 S. Amari, *Neural Net.* **2**, 451 (1989).

5.12 K. Aihara, T. Takabe, and M. Toyoda, *Phys. Lett.* A **144**, 333 (1990).

5.13 S. Kirkpatrick, C. D. Gelatt, Jr., and M. P. Vecchi, *Science* **220,** 671 (1983).

5.14 M. Morita, *Neural Net.* **6**, 115 (1993).

5.15 S. Yoshizawa, M. Morita, and S. Amari, *Neural Net.* **6**, 167 (1993).

5.16 M. Zak, *Neural Net.* **2**, 259 (1989).

5.17 上坂吉則著: ニューロコンピューティングの数学的基礎 p. 191-197 (近代科学社1993).

5.18 N. Farhat, D. Psaltis, A. Prata, and E. Paek, *Appl. Opt.* **24**, 1469 (1985).

5.19 J. S. Jang, S. Y. Shin, and S. Y. Lee, *Opt. Lett.* **13**, 693 (1988).

5.20 I. Shariv, and A. A. Friesem, *Opt. Lett.* **14**, 485 (1989).

5.21 S. H. Song, S. C. Park, and S. S. Lee, Opt. Lett. **15**, 1389 (1990).

5.22 H. Sakai, and J. Ohtsubo, *Appl. Opt.* **31**, 6852 (1992).

5.23 Cleber M. Gomes, H. Sekine, T. Yamazaki, and S. Kobayashi, *Neural Net.* **5**, 169 (1992).

"Is SLM useful for a real-time optical information processing?"

"It is a very attractive and promising device for real time optical information processing and computing."

CHAPTER 6

CONCLUSION

In the present thesis, we have discussed the real-time optical information processing and computing by using liquid crystal spatial light modulators (LC-SLMs), involving the real-time optical speckle metrology, real-time optical image processing, and optical neural networks for pattern recognition.

In Chapter 2, we have described the operation characteristics of LCTV- and FLC-SLMs. The advantages of these liquid crystal SLMs are their fast response time, high sensitivity, low-power operation, high spatial resolution, and so on. Moreover, LCTV has been recently used in the field of optical information processing because of the low cost of the device and the ease of the commercial availability. On the other hand, FLC-SLM has the excellent features of multiple exposure capability of images, much larger data throughput, and the great potential for further real-time optical processing. These excellent operation capabilities of LCTV- and FLC-SLMs have been demonstrated by our experiments for optical information processing and computing.

The method of the JTC is frequently used as a powerful tool for such as an object identification or a displacement measurement for speckle applications. In Chapter 3, the joint transform correlation for real-time optical speckle metrology have been investigated. A method for the generation of a joint pattern to calculate a real-time joint transform correlation function for speckle applications has been proposed in Section 3.2. To give a spatial shift to the pattern, the combination of a 90° TN-LC cell and a birefringent calcite plate has been used based on the polarization switching by the TN-LC cell and the optical path separation between the o- and e-rays through the birefringent plate. The successive two speckle patterns before and after the displacement have been detected. Then, the joint transform correlation function has been calculated. A good linear relation between the peak position of the correlation function and the object displacement has been obtained, which enables the application of this method to displacement and velocity measurements in speckle techniques.

In Section 3.3, we have successfully realized a real-time high-speed joint transform correlator for speckle applications by using FLC devices which can operate faster than a cycle

of several ms. A FLC polarization switch and a birefringent plate have been used to make a spatial shift of a speckle pattern. The joint pattern before and after the displacement of speckle patterns has been written onto a FLC-SLM which is operating synchronized with the FLC polarization switch. The joint pattern has been optically processed and the joint transform correlation pattern has been finally obtained. An object speed as fast as 100 mm/s can be measured by the current proposed system at its modest operation. We have used a CCD camera and a LCTV-SLM, so that the sampling rate of data for the displacement or the velocity measurement was slow in the present system. But, if an another FLC-SLM is available, a faster sampling rate of the data can be achieved by synchronizing the second FLC-SLM with the FLC polarization switch and the first FLC-SLM. FLC device has the capability of a time response as faster as about 100μs or more. Therefore, the device will be a promising one for real-time optical processing.

Optical images processing based on speckle phenomena have been used for extracting the difference between two images, image coding and decoding, image multiplexing, and so on. In Chapter 4, based on speckle modulation technique, real-time optical image subtraction and edge enhancement by using FLC devices have been conducted and the real-time high-speed image subtraction and edge enhancement have been successfully realized. The spatial shifts for a speckle pattern have been easily given through optical components consisted of the combination of FLC polarization switches and birefringent plates. Multiple-exposure images through a focused or defocused imaging system have been written onto the FLC-SLM. The subtracted and edge enhanced images have been successfully obtained from these multiple-exposure patterns by the Fourier filtering. The whole operation of the system was controlled by the microcomputer, and the operation speed is faster than 10 ms. As the used FLC-SLM has a high resolution more than 100 *l*p/mm and can store fine speckle patterns, the image qualities for the obtained results are quite satisfactory.

Neural network computation should prove useful in fields such as image analysis, artificial vision, pattern recognition, and automatic target recognition. Different technologies

have been used to implement such neural networks. Among these, software and electronic implementation have been much used. However, optical technology seems to provide inherent capabilities for neural network applications that require the processing of a large amount of data. This is especially true for image-related processing, in which optical technologies offer parallel processing and two-dimensional interconnections. Specifically, the recent advances in SLMs offer new alternatives for optical neural architectures. Many optical implementations of various neural network architectures have been proposed. However, there are two main flaws in the conventional associative memory model. The first one is that its capacity is not large. The second one is the existence of a large number of spurious memories.

Based on the concept of terminal attractor (TA), we have been presented a TA model optical neural network associative memory for reducing the spurious states and compared it with the conventional Hopfield model in Chapter 5. The computer simulations for pattern recognition have been performed by using a 6×6 neuron network model. Three patterns "A", "O", and "E" are embedded in the network as recognition target patterns. Furthermore, for discussing the feasibility of the optical implementation of the TA model associative memory, we used a network with 4×4 neuron and 3 stored patterns "A", "O", and "H". The TA model optical neural network for pattern recognition has been implemented by using LCTV-SLMs and CCD cameras. We have successfully realized the exponential and subtraction computations in the TA model dynamics by optical method. It has been proved from the experiment that all optical neural network based on the TA model can be realized by using currently available electrical and optical addressed SLMs. The experiment results has also indicated that the TA model can reduce spurious states in the Hopfield neural network and the recalling capability can be much improved. However, there still remain some important problems such as mathematical analysis and experimental demonstration of memory capacity and biological relevance in the TA model. We should further study the dynamics of the neural networks.

Now we can give some answers for the question that "Are SLMs useful for real-time optical information procession?" at the beginning of this thesis: "SLMs are very attractive and

promising device and they have much larger data throughput and the great potential for further real-time optical information processing and computing."

In the finale of the thesis, I like to say: "Optics is an old and venerable subject and it also is a novel and captivating subject..."

Appendix A

FLC-SLM CHARACTERISTICS[A.1]

Table A.1 FLC-SLM characteristics

Characteristic	Parameter
Active area	20 mm × 20 mm
Resolution(1)	72 *l*p/mm
Sensitivity(2)	100 μW/cm^2
Visibility	0.86
Response time for writing in the positive mode	t_p=42 μs
Response time for writing in the positive mode	t_n=43 μs
Reflectivity	99%
Readout wavelength	633 nm
Memory	Binary
Image polarity	Bipolar

(1) Grating first-order diffraction efficiency has fallen to half the maximum value.

(2) The write wavelength is 633 nm.

Appendix B

EFFECT OF A FOCUSING ERROR ON THE OTF[B.1]

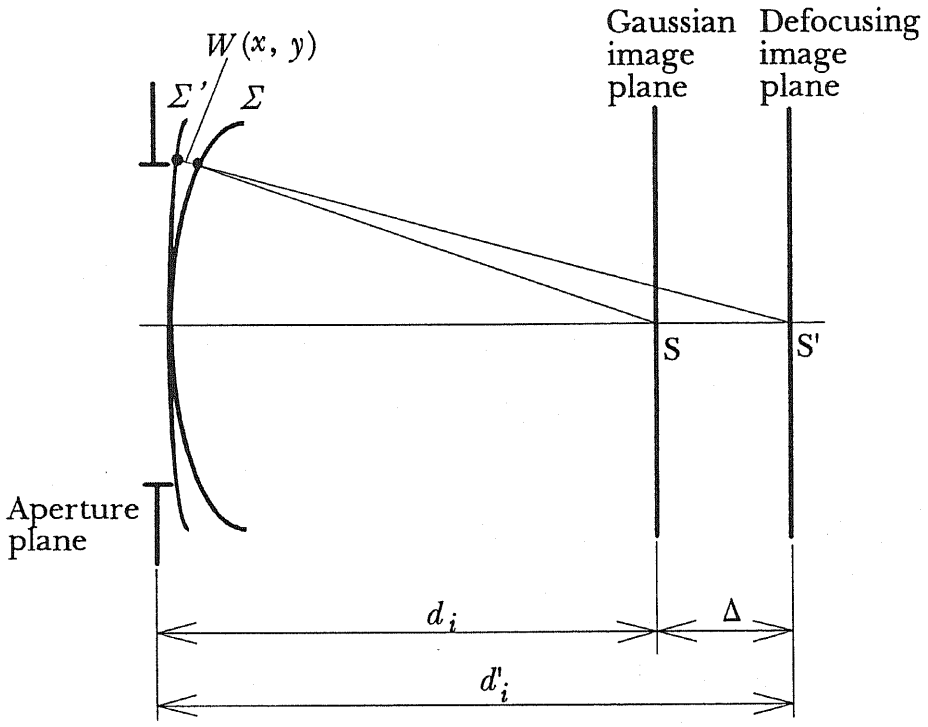

Fig. B.1 The wavefront aberrations of a defocusing system. $\Delta \approx \varepsilon d_i^2$.

From elementary geometrical optics, the condition of focus of a optical imaging system is determined by the lens law (or Gaussian law)

$$\frac{1}{d_i}+\frac{1}{d_o}-\frac{1}{f}=0, \tag{B.1}$$

where d_i and d_o are image and object distances of the imaging system, respectively, and f is the focal length.

As shown in Fig. A.1, when the image plane is out of focus, the more general relation

$$\frac{1}{d_i}+\frac{1}{d_o}-\frac{1}{f}=\varepsilon, \tag{B.2}$$

will hold. The aberration function $W(x,y)$ is given by

$$W(x,y)=\frac{\varepsilon}{2}(x^2+y^2). \tag{B.3}$$

For a square aperture of width $l=2\lambda d_i f_0$ (f_0 is the coherent cutoff frequency), the maximum phase error at the edge of the aperture (along the x or y axis) is $\varepsilon k l^2/8$. Thus the maximum path-length error, which we represent by w, is given by

$$w=\frac{\varepsilon l^2}{8}=\frac{\varepsilon}{2}(\lambda d_i f_0)^2. \tag{B.4}$$

The number w is a convenient indication of the severity of the focusing error. If the aberration function $W(x,y)$ given by Eq. (A.3) is substituted in the OTF of an aberration system, then

$$\begin{aligned} H(u,v)=\frac{1}{l^2}\iint_{-\infty}^{\infty} & P(x+\lambda d_i u, y+\lambda d_i v)P(x,y) \\ & \times\exp\left\{j\frac{kw}{(\lambda d_i f_0)^2}\left[(x+\lambda d_i u)^2+(y+\lambda d_i v)^2-(x^2+y^2)\right]\right\}dx\,dy, \end{aligned} \tag{B.5}$$

where $P(\cdot)$ is a pupil function. Equation (A.5) may be expressed in the symmetrical form

$$\begin{aligned} H(u,v)=\frac{1}{l^2}\iint_{-\infty}^{\infty} & P\left(x+\frac{\lambda d_i u}{2}, y+\frac{\lambda d_i v}{2}\right)P\left(x-\frac{\lambda d_i u}{2}, y-\frac{\lambda d_i v}{2}\right) \\ & \times\exp\left\{j\frac{kw}{(\lambda d_i f_0)^2}\left[\left(x+\frac{\lambda d_i u}{2}\right)^2+\left(y+\frac{\lambda d_i v}{2}\right)^2-\left(x-\frac{\lambda d_i u}{2}\right)^2-\left(y-\frac{\lambda d_i v}{2}\right)^2\right]\right\}dx\,dy. \end{aligned} \tag{B.6}$$

The area of overlap of two displaced pupil functions is a rectangle of $(l-\lambda d_i|u|)(l-\lambda d_i|v|)$. Consequently,

$$H(u,v)=\frac{1}{l^2}\iint_{-\infty}^{\infty}\Pi\left(\frac{x}{l-\lambda d_i|u|}\right)\cdot\Pi\left(\frac{y}{l-\lambda d_i|v|}\right)\exp\left\{j2\pi\left[\left(\frac{-2uw}{\lambda^2 d_i f_0^2}\right)x+\left(\frac{-2vw}{\lambda^2 d_i f_0^2}\right)y\right]\right\}dx\,dy$$
$$=\frac{1}{l^2}(l-\lambda d_i|u|)(l-\lambda d_i|v|)\,\mathrm{sinc}\left[(l-\lambda d_i|u|)\left(\frac{-2uw}{\lambda^2 d_i f_0^2}\right)\right]\mathrm{sinc}\left[(l-\lambda d_i|v|)\left(\frac{-2vw}{\lambda^2 d_i f_0^2}\right)\right], \tag{B.7}$$

where $\Pi(\cdot)$ and $\mathrm{sinc}(\cdot)$ are rectangle and sinc functions, respectively. The sinc function is an even function, and so the Eq. (A.7) may be written in the form

$$H(u,v)=\Lambda\left(\frac{u}{2f_0}\right)\cdot\Lambda\left(\frac{v}{2f_0}\right)\cdot\mathrm{sinc}\left[\frac{8w}{\lambda}\left(\frac{u}{2f_0}\right)\left(1-\frac{|u|}{2f_0}\right)\right]$$
$$\times\,\mathrm{sinc}\left[\frac{8w}{\lambda}\left(\frac{v}{2f_0}\right)\left(1-\frac{|v|}{2f_0}\right)\right]. \tag{B.8}$$

Here, $\Lambda(\cdot)$ is a triangle function.

Appendix C

PROOF OF LINEARLY STABILITY FOR TA DYNAMICAL SYSTEM[C.1]

At first, let us linearize the system described in Eq. (5.10) with respect to points $f[x_i(t)]$ which are sufficiently close to the equilibrium points $x_i^{(m)}$, so that

$$\left|f[x_i(t)] - x_i^{(m)}\right| = \varepsilon \to 0. \tag{C.1}$$

The linearized versions of the system in Eq. (5.10) in the neighborhoods of the corresponding equilibrium point is given by

$$\frac{dx_i(t)}{dt} = \sum_{j=1}^{N} J_{ij}\left(x_j^{(m)}\right)\left\{f[x_j(t)] - x_j^{(m)}\right\}, \tag{C.2}$$

where the Jacobi matrix $J_{ij}\left(x_j^{(m)}\right)$ is accomplished by a first-order approximation of a Taylor-series expansion of systems in Eqs. (5.10) and (5.11):

$$J_{ij}\left(x_j^{(m)}\right) = \frac{W_{ij}}{\cosh^2 x_i(t)} \qquad (i \neq j), \tag{C.3}$$

$$J_{ii}\left(x_j^{(m)}\right) = -1 + \frac{W_{ii}}{\cosh^2 x_i(t)} - \alpha^{(m)}\left(\frac{1}{3}\varepsilon^{-2/3} - 2\beta^{(m)}\varepsilon^{4/3}\right)\cdot\exp(-\beta^{(m)}\varepsilon^2). \tag{C.4}$$

Now the stability of the equilibrium points $x_i^{(m)}$ depends on the eigenvalues λ_m of the matrices $J_{ij}(x_j^{(m)})$, respectively.[C.2] In order to find these eigenvalues, let us multiply the matrices $J_{ij}(x_j^{(m)})$ by $\varepsilon^{2/3}(\varepsilon \to 0)$

$$J_{ij}^{*}\left(x_j^{(m)}\right) = \varepsilon^{2/3} J_{ij}\left(x_j^{(m)}\right). \tag{C.5}$$

Then, as follows from Eqs. (B.3) and (B.4), at $\varepsilon \to 0$, respectively,

$$J_{ij}^{*}\left(x_j^{(m)}\right)(i \neq j) \to 0, \tag{C.6}$$

$$J_{ii}^{*}\left(x_j^{(m)}\right) \to -\frac{1}{3}\alpha^{(m)}, \tag{C.7}$$

that is, the matrix $J_{ii}(x_j^{(m)})$ is a diagonal at $\varepsilon \to 0$, and its eigenvalues are

$$\lambda_m^{*} = -\frac{1}{3}\alpha^{(m)} \quad m = 1,2,\ldots,N(=M). \tag{C.8}$$

Hence, at $\varepsilon \to 0$

$$\lambda_m = \varepsilon^{-2/3}\lambda_m^{*} = -\frac{1}{3}\alpha^{(m)}\varepsilon^{-2/3} \to -\infty. \tag{C.9}$$

Thus, all the eigenvalues of the matrices $J_{ij}(x_j^{(m)})$ are negative and unbounded at the equilibrium points $x_i^{(m)}$, which means that all these desired equilibrium points are stable.

REFERENCES

A.1 Y. Kobayashi, T. Takemori, N. Mukohzaka, N. Yoshida, and S. Fukushima, *Appl. Opt.* **33**, 2785 (1994).

B.1 J.W.Goodman, *Introduction to Fourier Optics* Cha.6 (McGraw-Hill, San Francisco,1968).

C.1 M. Zak, *Neural Net.* **2**, 259 (1989).

C.2 上坂吉則著: ニューロコンピューティングの数学的基礎 p. 191-197 (近代科学社1993).

ACKNOWLEDGMENTS

I would like to express my appreciation to my supervisor Prof. J. Ohtsubo for his guidance, encouragement and valuable discussion throughout the course of this research, without which this thesis would not have been possible. I would like to acknowledge to Prof. T. Kubo, Prof. Y. Hatanaka, Prof. A. Sasaki, and Mr. T. Takemori for their valuable discussion and advice. I am also grateful to my colleagues in my laboratory for their various cooperations during the past four year. I would also like to thank Prof. Dr. Y. Suzuki and Dr. T. Hara of Hamamatsu Photonics, and Dr. T. Kurokawa of NTT for the use of the FLC-SLMs.

I wish to express my thanks to the Japanese Monbusho, for providing the Monbusho Scholarship in the academic 1992.1-1996.3, during the period I was able to pursue my research.

I am unable to express adequate thanks to my husband, Erlin Ye, not only for his love and encouragement, but also for helping me to complete some calculation.

Last but not least, my thanks go to my mother, father, and sisters who have always stood by me with love.

Xin Lin

LIST OF PAPERS AND PRESENTATIONS

Papers

1. Xin Lin and Junji Ohtsubo, and Tamiki Takemori, "Generation of a Joint Pattern for Optical Speckle JTC by Using a Liquid Crystal Cell and a Birefringent Plate", Optics Commun. **98**, 41 (1993).
2. Xin Lin, Junji Ohtsubo, Yasuhisa Tsujita, Takahiro Kubo, and Tamiki Takemori, "Real-Time Optical Joint Transform Correlator and its Application to Speckle Measurements", SPIE Proc.**1983**, 374 (1993).
3. Xin Lin, Junji Ohtsubo, and Tamiki Takemori, "Real-Time Optical Speckle JTC Using FLC-SLM", Rep. Grad. School Electron. Sci. Technol. Shizuoka Univ. **16**,113 (1995).
4. Xin Lin, Junji Ohtsubo, and Tamiki Takemori, "Real-Time Optical Images Subtraction and Enhancement Using FLC Devices Based on Speckle Modulation", Appl. Opt. to be published.
5. Xin Lin, and Junji Ohtsubo, "Terminal Attractor Optical Associative Memory for Pattern Recognition", Proceedings of 16th meeting on lightwave sensing technology **LST 16**, 45 (1995).
6. Xin Lin, and Junji Ohtsubo, "Optical Neural Networks with Terminal Attractors for Pattern Recognition", Opt. Eng. contributing.
7. X. Lin, and J. Shi, "Application of Infranics for 10.6μm Laser Facula Tracing System", Optical Society of China Proc.**3,** 355 (1989).
8. X. Lin, and J. Shi, "A Study of a 10.6μm Laser Facula Tracing System", Optics and Fine Mechanics **122**, 20 (1991).
9. X. Lin, and J. Shi, "A Method of Improvement Performance for Opto-electronic Precision Tracing System", Weapon Industry Society of China Proc.**10,** 123 (1991).

Presentations

1. 林新、大坪順次、竹森民樹 ” ＴＮ液晶セルと複屈折板の組み合わせを用いたスペックル光結合相関計”、光学連合シンポジウム京都 ’92 (1992.9).
2. 林新、大坪順次、竹森民樹 ” FLC偏光スイッチと複屈折板を用いたスペックル光結合相関計”、第40回応用物理学関係連合講演会 (1993.3).
3. Junji Ohtsubo, Xin Lin, Yasuhisa Tsujita, Takahiro Kubo, and Tamiki Takemori, "Real-Time Optical Joint Transform Correlator and its Application to Speckle Measurements", ICO-16 Budapest (1993.8).
4. 林新、大坪順次、竹森民樹 ” FLC-SLMを用いたスペックル変調画像の実時間減算 ”、第41回応用物理学関係連合講演会 (1994.3).
5. 林新、大坪順次、竹森民樹 ” FLC-SLMを用いたスペックル変調実時間画像のエッジエンハンス ”、第42回応用物理学関係連合講演会 (1995.3).
6. 林新、大坪順次 ” ターミナルアトラクタを使ったニューラルネットワーク連想メモリ”、第56回応用物理学会学術講演会 (1995.8).
7. 林新、大坪順次 ” ターミナルアトラクタ 連想メモリの光学的実現”、光学連合シンポジウム東京 ’95 (1995.9).
8. 林新、大坪順次 ” ターミナルアトラクタ光連想メモリを使ったパターン認識”、第16回光波センシング技術研究会講演会 (1995.12).

Xin LIN

M.S. 1990, Changchun Institute of Fine Mechanics, Academia Sinica. Ph.D. 1993 to the present, Shizuoka University, Japan.

Research interests include optical information processing and optical neural networks.

I like reading and art. I believe that wisdom and beauty are eternal endeavor of human kind.